



UNIVERSITY OF GENEVA  
DEPARTMENT OF ASTRONOMY  
FACULTY OF SCIENCE

## Master Thesis

---

# Reflected Light from Hot Jupiters as Seen by TESS

---

In partial fulfilment of the requirements for the Master in Astrophysics  
degree

**Supervisors:**

Prof. Monika Lendl  
Dr. Adrien Deline

**Submitted by:**

Shivom Gupta

**Examiners:**

Prof. Monika Lendl  
Dr. Adrien Deline  
Prof. Xavier Dumusque

Academic year 2021/2022



# Summary

With more than 5000 exoplanets discovered since the first detection in the late 20<sup>th</sup> century, research in this field has seen a rapid evolution from detection to characterization of planets using photometry and spectroscopy. The most studied class of planets are hot Jupiters, gas giants orbiting very close to their host star which are relatively easy targets for detecting reflected light. This light as phase variation and secondary eclipse in the light curve has helped in constraining the properties of the upper atmosphere with day side temperature, albedos, clouds and winds. The geometric albedo of hot Jupiters has a wide range which indicates different types of clouds, and heat redistribution efficiency between the day and night side. The study of this light in visible and infrared has the potential to explain day side brightness temperature and geometric albedo very well. This thesis mostly deals with the very first steps in learning all of this; Analysing TESS data from 28 hot Jupiters to detect secondary eclipses and further tries to address observational and physical aspects with the obtained results of hot Jupiters mainly concerning those where an eclipse detection is achieved.

Keywords: hot Jupiters, secondary eclipse, light curve modeling, gaussian processes, albedo.

# Contents

<b>Summary</b>	i
<b>List of Tables</b>	v
<b>List of Figures</b>	vii
<b>Acknowledgements</b>	xi
<b>1 Introduction to Exoplanets</b>	1
1.1 Transit . . . . .	2
1.1.1 Orbital Parameters . . . . .	5
1.1.2 Light Curve . . . . .	6
1.1.3 Stellar Limb Darkening . . . . .	9
1.2 Secondary Eclipse & Phase Curve . . . . .	9
1.3 Transiting Exoplanet Survey Satellite (TESS) . . . . .	13
<b>2 Analysis of WASP-33b</b>	15
2.1 Data . . . . .	15
2.1.1 Lomb-Scargle Periodogram & BLS model . . . . .	16
2.1.2 BATMAN model . . . . .	18
2.2 Model fitting with MCMC . . . . .	19
2.3 Gaussian Processes . . . . .	23
2.3.1 GP Kernel . . . . .	23
2.4 GP & BATMAN joint modeling and fitting . . . . .	24
2.4.1 Data binning and Error treatment . . . . .	25
2.4.2 GP model . . . . .	25
2.4.3 GP Prediction . . . . .	28
<b>3 Secondary Eclipses from Hot Jupiters</b>	31
3.1 Target selection . . . . .	32
3.2 Data Acquisition and Analysis . . . . .	32
3.2.1 TIC 69679391 (KELT-20 b/MASCARA-2 b/HD 185603) . . . . .	33
3.2.2 TIC 290131778 (TOI-123 A b/HD 202772 A b) . . . . .	35
3.2.3 TIC 367366318 (KELT-7 b) . . . . .	37
3.2.4 TIC 293435336 (WASP-76 b) . . . . .	39

3.2.5	TIC 399870368 (TOI-624 b/HAT-P-70 b ) . . . . .	40
3.2.6	TIC 1129033/WASP-77 A b . . . . .	41
3.2.7	TIC 25375553/WASP-111 b . . . . .	43
3.2.8	TIC 16740101/KELT-9 b/HD 195689 A b . . . . .	44
3.2.9	TIC 100100827/WASP-18 b/TOI-185 b . . . . .	46
3.2.10	Marginal Detections . . . . .	47
3.2.11	Non Detections . . . . .	47
3.3	Results . . . . .	51
3.3.1	Observational and Physical Aspects of Hot Jupiters . . . . .	51
3.3.2	$T_{eq}$ Vs the ratio of $T_{eq}/T_b$ . . . . .	53
3.3.3	Bond Albedo ( $A_B$ ) Vs Equilibrium Temperature ( $T_{eq}$ ) . . . . .	54
<b>4</b>	<b>Conclusion &amp; Next Work</b>	<b>57</b>
<b>Appendix</b>		<b>59</b>
<b>Bibliography</b>		<b>67</b>

# List of Tables

3.1	Results from KELT-20 b based on secondary eclipse analysis . . . . .	35
3.2	Results from HD 202772 A b analysis with BATMAN model. . . . .	37
3.3	Results from KELT-7 b analysis with BATMAN model. . . . .	38
3.4	Results from WASP-76 b analysis with BATMAN model. . . . .	40
3.5	Results from HAT-P-70 b analysis with BATMAN model. . . . .	41
3.6	Results from WASP-77 A b analysis with BATMAN model. . . . .	43
3.7	Results from WASP-111 b analysis with BATMAN model. . . . .	44
3.8	Results from KELT-9 b analysis with BATMAN model. . . . .	45
3.9	Results from WASP-18 b analysis with BATMAN model. . . . .	46
4.3	Marginal detections. . . . .	59
4.1	Results from WASP-33 b analysis with BATMAN only and (GP+BATMAN) model. . . . .	59
4.2	Results from hot Jupiters analysis with significant eclipse detection. . . . .	60

# List of Figures

1.1	All exoplanet detection methods developed so far. . . . .	3
1.2	Mass-Orbital Period diagram for confirmed exoplanets. . . . .	4
1.3	Schematic for a full and grazing transit. . . . .	4
1.4	Illustration of a planet orbiting in an eccentric orbit. . . . .	5
1.5	Illustration of a transiting planet: Two cases with different impact parameters. . . . .	7
1.6	Impact on light curve shape at different wavelengths. . . . .	10
1.7	Schematic of a full light curve with both transit and secondary eclipse. .	11
1.8	Phase curve of LHS3844b centered at the secondary eclipse. . . . .	12
1.9	Schematic of TESS field of view and four CCD cameras. . . . .	14
2.1	WASP-33 b data from sector 18. . . . .	16
2.2	Periodogram and window function for WASP-33 b. . . . .	17
2.3	Full model of light curve along with different components, transit, secondary eclipse and phase curve model. . . . .	19
2.4	A general plot of posterior probability with prior and likelihood and illustration of MCMC walkers exploring the parameter space. . . . .	21
2.5	Best fit BATMAN model and corresponding residuals for WASP-33 b .	22
2.6	Best fit GP model plotted over residuals from BATMAN model and WASP-33 b data. . . . .	26
2.7	100 BATMAN models plotted over detrended data of WASP-33 b, zoom-in over eclipse and residuals from best fit GP+BATMAN model. . . .	27
2.8	Joint GP+BATMAN model plotted over raw data of WASP-33 b . . .	28
2.9	BATMAN model plotted over detrended data of WASP-33b and zoom-in view over a single transit & eclipse. . . . .	28
2.10	GP model prediction for WASP-33 b data along with prediction for the gap.	29
3.1	Band pass of TESS, CHEOPS and Kepler (left). Position of 42 targets of interest(Right). . . . .	33
3.2	GP model for detrending KELT-20 b data from sector 14. . . . .	34
3.3	100 BATMAN models plotted over detrended data (sector 14, 40) of KELT-20 b, zoom-in over eclipse and residuals from best fit GP+BATMAN model.	35
3.4	100 BATMAN models plotted over detrended data (sector 1, 28) of HD 202772A b, zoom-in over eclipse and residuals from best fit GP+BATMAN model. . . . .	36

3.5	100 BATMAN models plotted over detrended data (sector 43, 45) of KELT-7 b, zoom-in over eclipse and residuals from best fit GP+BATMAN model.	38
3.6	100 BATMAN models plotted over detrended data (sector 30, 42) of WASP-76 b, zoom-in over eclipse and residuals from best fit GP+BATMAN model.	39
3.7	100 BATMAN models plotted over detrended data (sector 32) of HAT-P-70 b, zoom-in over eclipse and residuals from best fit GP+BATMAN model.	41
3.8	100 BATMAN models plotted over detrended data (sector 31) of WASP-77 A b, zoom-in over eclipse and residuals from best fit GP+BATMAN model.	42
3.9	100 BATMAN models plotted over detrended data (sector 28) of WASP-111 b, zoom-in over eclipse and residuals from best fit GP+BATMAN model.	43
3.10	100 BATMAN models plotted over detrended data (sector 14, 15) of KELT-9 b, zoom-in over eclipse and residuals from best fit GP+BATMAN model.	45
3.11	100 BATMAN models plotted over detrended data (sector 2) of WASP-18 b, zoom-in over eclipse and residuals from best fit GP+BATMAN model.	47
3.12	100 BATMAN models plotted over detrended data (sector 1,27) of WASP-94 A b, zoom-in over marginally detected eclipse.	48
3.13	100 BATMAN models plotted over detrended data (sector 7, 34) of HAT-P-30 b, zoom-in over marginally detected eclipse.	48
3.14	100 BATMAN models plotted over detrended data (sector 1) of WASP-95 b, zoom-in over marginally detected eclipse.	49
3.15	100 BATMAN models plotted over detrended data (sector 38) of KELT-26 b, zoom-in over marginally detected eclipse.	49
3.16	100 BATMAN models plotted over detrended data (sector 39) of TIC-362709886, zoom-in over marginally detected eclipse.	50
3.17	100 BATMAN models plotted over detrended data (sector 46) of KELT-17 b, zoom-in over marginally detected eclipse.	50
3.18	100 BATMAN models plotted over detrended data (sector 41) of HAT-P-49 b, zoom-in over marginally detected eclipse.	51
3.19	Equilibrium temperature Vs relative planet size for all confirmed exoplanets.	52
3.20	Blackbody curve for all 9 exoplanets for which we get secondary eclipse detection.	53
3.21	Equilibrium temperature Vs the ratio of equilibrium temperature to brightness temperature for both efficient and inefficient heat redistribution factor.	54
3.22	Bond albedo Vs equilibrium temperature plots with different models of heat redistribution.	55
4.1	Corner plot from BATMAN model analysis of WASP-33 b	62
4.2	Loglikelihood progress with MCMC steps for WASP-33 b analysis.	62
4.3	MCMC chains after burn-in step from WASP-33 b analysis.	63
4.4	Corner plot from joint sector analysis of WASP-77 A b	64
4.5	Corner plot from the joint sector analysis of WASP-111 b	65

4.6 Corner plot from the joint sector analysis of WASP-18 b	66
---	----

# Acknowledgements

I would like to render my warmest thanks to my supervisors Monika Lendl and Adrian Delne for their guidance and encouragement for constant improvement. Monthly meetings helped keep a check on my progress in both thesis writing and data analysis part. Important discussions during those meetings helped me improve my theoretical understanding of the topic. Numerous individual meetings with Adrian helped me progress in the data analysis part. With this project, I got an opportunity to work with real data. I hope to turn this thesis work towards an actual contribution to exoplanet research through a publication after implementing needed improvements that meet the standard of a publication.

I would like to thank for the weekly photometry and atmosphere group meetings. I am thankful to people from these groups, especially Angeliki Psaridi, Solène Ulmer-Moll and Tunde Akinsanmi for useful discussions. I thank my friend William Ceva for the discussion in the initial days as I was trying to implement the BATMAN model. I am thankful to Maddalena Bugatti for always inspiring and motivating me, and to all my classmates for amazing two years together. I am thankful to all my teachers including Francesco Pepe, Georges Meynet, Emline Bolmont and David Ehrenreich for insightful lectures and interactions. People outside the department, Surhud More from IUCAA and my friend Akanksha Tiwary inspired me to make the tough decision of leaving the job to pursue a master in astrophysics. I am thankful to Sara Seager as one of her talk paved a path for my interest in extraterrestrial life. This thesis work would not have been possible without the support from Daniel Schaeerer as I was facing a tough financial situation since the first year of my master. I am highly indebted to the University and the department for providing me with an opportunity and support to pursue my master.

An indirect contribution from my mother Nisha Gupta, my sister Ankita Gupta and Soni Gupta can't be put into words as they motivated me in difficult times. Blessings and support from my grandmother Sneh Lata Gupta, grandfather Suresh Chandra Gupta, aunt Niti Gupta, uncle Chandra Prakash Gupta and aunt Nandini Prakash, and uncle Brijesh Gupta from my village, kept me going. I would also like to thank my brother Gaurav Gupta and Ishu Gupta for their support as I was preparing to come to Geneva.

I would like to dedicate this thesis work and my master in the memory of my father Santosh Kumar Gupta, paternal grandfather Babu Ram Gupta, grandmother Shanti Devi and uncle Vijay Kumar Gupta.

# Chapter 1

## Introduction to Exoplanets

People have imagined and speculated about the presence of planets around other stars since time immemorial. The first image of a planetary disk around the star Beta Pictoris in 1984 [47] was a demonstration and a test bed for later known to be direct imaging method. However, this technique has contributed to only about 1% of total exoplanets discoveries to date, as it becomes challenging to deal with high contrast between the planet and its host starlight.

A typical Earth-size planet around a Sun-like star is a billion times fainter which makes it extremely difficult to detect even a Jupiter sized planet. With direct imaging from ground-based telescopes available at that time, astronomers realized the feasibility of such detection, so they changed their strategy and began developing indirect methods to infer the presence of exoplanets.

Radial velocity observations of binary stars back in the 1980s gave some hope for detecting exoplanets indirectly. Two such high precision observations by astronomers[7][29] indicated to have signals from planetary-mass objects but could not be confirmed. Continuous efforts turned into a breakthrough until the late 20<sup>th</sup> century when the very first exoplanets were discovered. In 1992, two astronomers (Wolszczan & Frail)[58] used the Pulsar Timing method and came up with strong evidence of a planet orbiting a neutron star. However, this method has contributed to less than 1% of total exoplanets discovered to date.

Three years later in 1995, two astronomers (Mayor & Queloz)[37] from Geneva Observatory discovered the first exoplanet around a Sun-like star using radial velocity methods. This technique revolutionised exoplanet detection and characterization since 1995. Their significant contribution led the professor-student duo to share a Nobel Prize in Physics along with James Peebles in 2019. In the last two decades, the radial velocity method has emerged as the second most powerful technique after the transit method. Together, they help in constraining the mass and the radius of the planet respectively, which gives a global view of the planetary composition.

Apart from transit, radial velocity and pulsar timing, the contribution from astrometry, gravitational microlensing, Transit Timing Variation (TTV) and numerous other methods have been crucial in the discovery of exoplanets in a wide range of systems. Figure 1.1 shows all the exoplanet detection methods developed so far. The recent announcement of a potential planetary candidate orbiting an X-ray binary in another galaxy M51[13] points towards remarkable capabilities of microlensing technique which has contributed to farthermost planet discoveries in our galaxy. Exoplanet characterization with the aforementioned methods has provided us with a spectrum of planets and this characterization is no more limited to just individual planets. Exoplanets in multi-planetary systems inferred using TTV have opened up a new possibility to characterize other stellar systems as a single entity[38].

With more than 5000 planets discovered by June 3, 2022, as shown in Figure 1.2, the exploration has just begun. Though these numbers keep changing frequently, we have seen a paradigm shift from just detecting to characterizing exoplanets in the last decade. In tandem with detecting more planets, atmosphere detection and characterization of hot Jupiters using transmission spectroscopy have revealed the chemistry of their atmosphere [14][52]. Astronomers have also learned about their atmosphere circulation and global energy budget with reflection spectra [20]. Hot Jupiters are a key set of planets which require extensive observations, both photometric and spectroscopic until the advent of a new generation of telescopes capable of detecting and probing smaller rocky planets in the super-Earth regime in the next two decades.

In this thesis, I will be dealing with hot Jupiters as secondary eclipse observations are currently feasible for planets in this class. This is mostly due to their size and proximity to the host star which maximizes the signal to noise ratio (SNR) achieved in the data collected from current space and ground-based telescopes. Specifically, I will be using data from Transiting Exoplanet Survey Satellite (TESS)[42] to identify good targets for high precision secondary eclipse follow-up observation from CHaracterising ExOPlanets Satellite (CHEOPS)[3]

## 1.1 Transit

The transit method, the most successful and widely used technique, has solely contributed to the discovery of more than 3000 exoplanets out of a total of about 5000 at the time of writing. During transit, a planet passing in front of a star blocks a small fraction of its light thus causing a dip in the stellar flux. This dip is about 1% of the stellar light for a Jupiter-like planet orbiting a Sun-like star.

Since the discovery of the first exoplanet using this technique (Charbonneau et al. 2000)[9] & Henry et al. 2000 [24], significant improvement in instrumentation and data analysis has made possible the finding of smaller planets. Besides, new space-based ob-

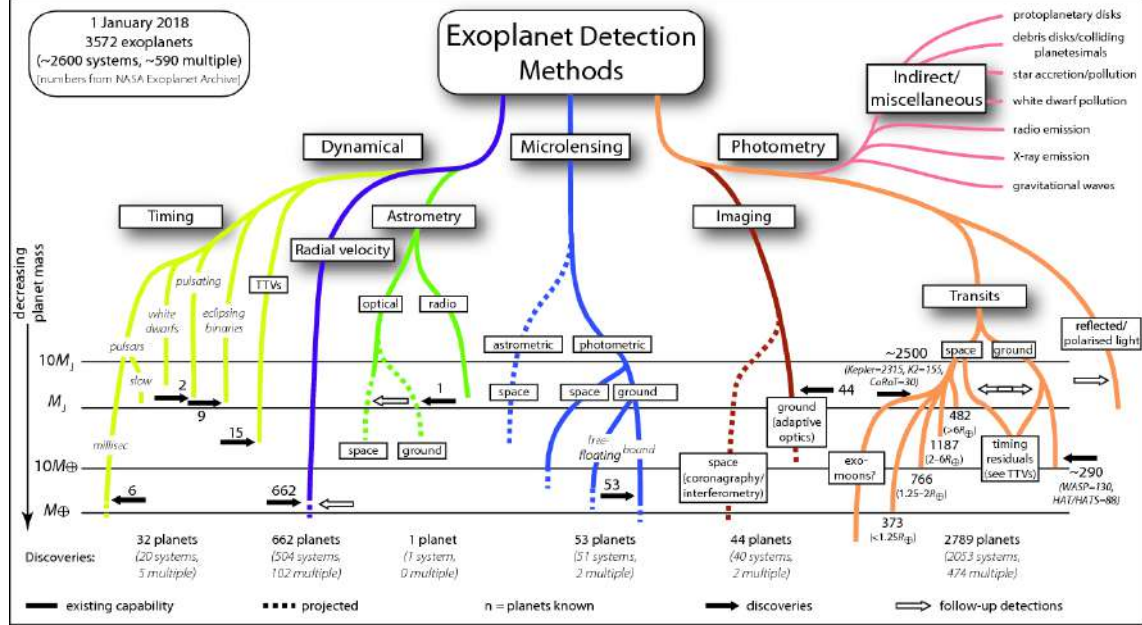


**Figure 1.1:** All the exoplanet detection methods developed so far. Figure showing both direct and indirect methods along with sensitivities of each for detecting different mas range of planets. Figure taken from (M. Perryman), 2018.

servatories[42][3][6] has been advantageous as Earth's atmosphere is no more a hurdle and we can achieve high-quality data even with a small telescope.

Based on observations, astronomers estimate that each star in our Milky Way galaxy has at least one planet on average [8]. Not all the stars probed through the transit method have shown the presence of a planet. This is attributed to the fact that planets need to be orbiting nearly edge-on to be detected, which is not the case with every planetary system. A planet sweeps a band of shadow as it transits the star. An observer needs to be within the antumbra region of this shadow to observe a full transit (see Fig. 1.3). Considering an observer on Earth is at an infinite distance relative to star-planet distance, the probability of the planet's shadow falling on Earth would largely depend on the star-planet distance and their relative size. Thus, we can define the probability of occurrence of a transit event. Assuming a planet has a circular orbit, the transit probability is given by:

$$P_{\text{transit}} = \sin \Theta = \frac{R_* + R_p}{a} \quad (1.1)$$

Where,  $\Theta$ ,  $R_*$ ,  $R_p$  and  $a$  are opening half-angle of the cone (see Fig. 1.3), stellar radius, planetary radius and semi-major axis distance respectively.

For an eccentric orbit, this probability is given by:

$$P_{\text{transit(ecc)}} = \left( \frac{R_* + R_p}{a} \right) \left( \frac{1}{1 - e^2} \right) \quad (1.2)$$

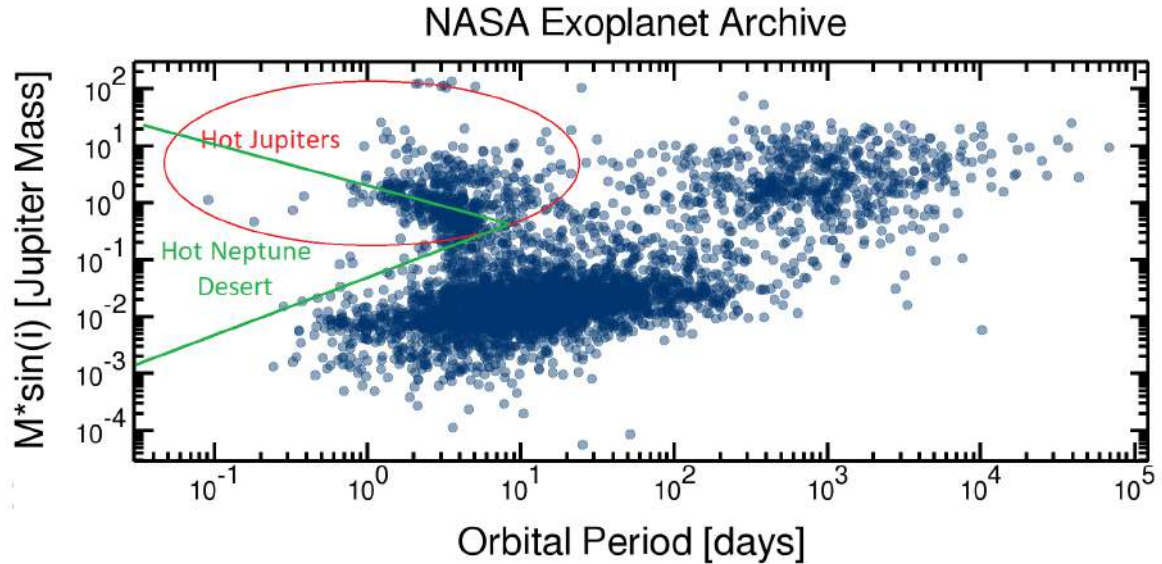


**Figure 1.2:** Mass-Orbital Period diagram for confirmed exoplanets till December 14, 2021. Hot Jupiter population is encircled in red.

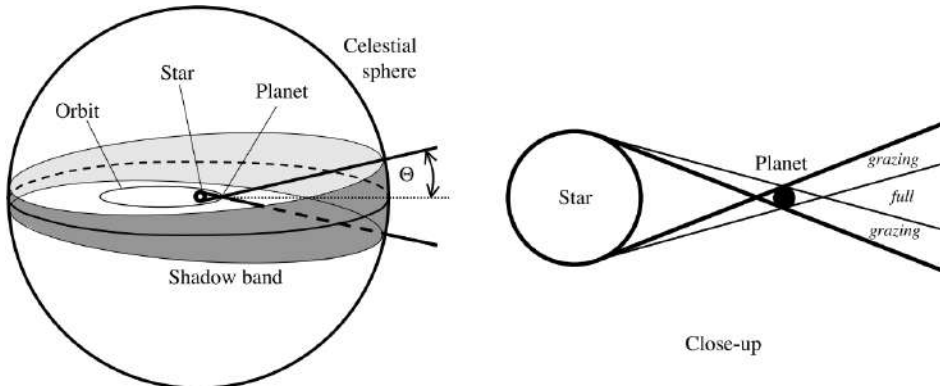


**Figure 1.3:** Figure showing shadow band (left) swept by a planet as it transits the star. A full transit will be visible in the antumbra region marked by thin lines (right) compared to a grazing transit in the penumbra region marked by thick lines.

The probability of transit for an eccentric orbit will be higher than the one we get from equation 1.2, if the periastron of the planet's orbit points towards the observer. For all planet the probability of transit increase if the star is larger and this applies also when  $R_p \ll R_*$ . More close in and bigger planets have a high probability of being detected compared to those far out. This also creates a strong bias in the planet population statistics where we see more gas giants compared to smaller rocky planets. But, this bias was prominently visible until 2019 as astronomers since then have found more smaller planets which makes Figure 1.2 less biased but still biased as we can't yet detect very small rocky planets down to Mercury.

However, we see a non-uniformity in this planet population diagram, especially in the region below 10 days of the orbital period. Here, we see the scarcity of hot Neptunes as a big gap (see Fig. 1.2) is prominently visible between hot Jupiters and smaller rocky

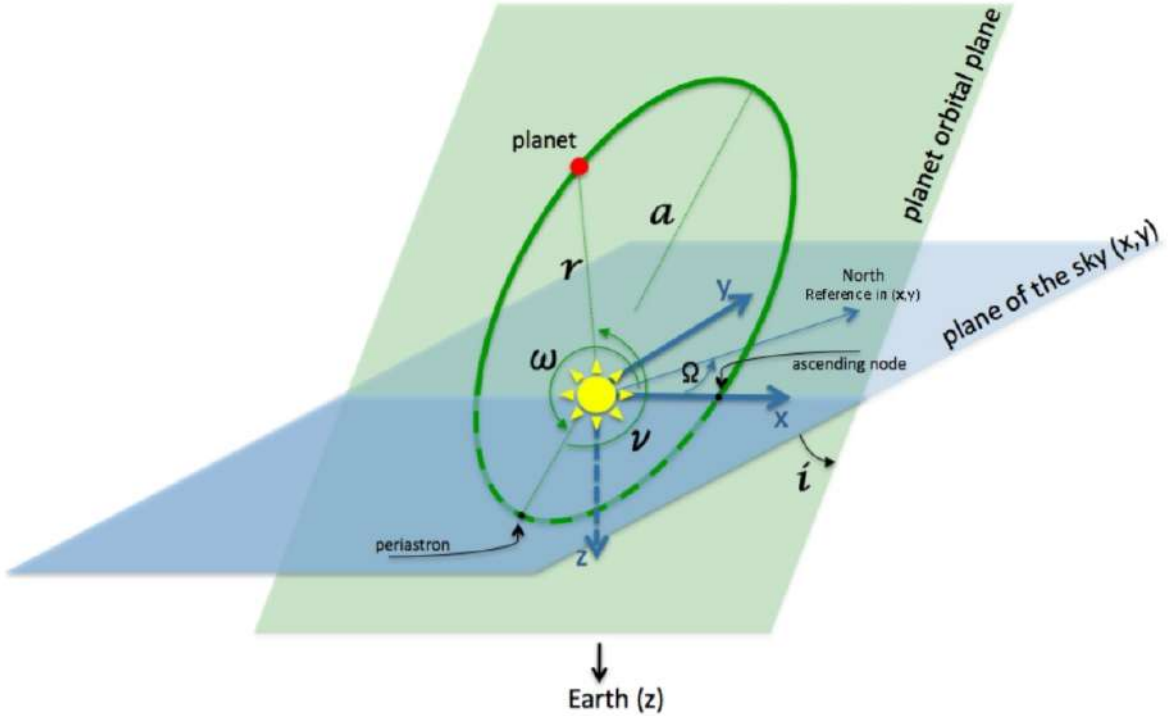


**Figure 1.4:** Schematic describing various elements that explains a planet in an eccentric orbit inclined at angle  $i$ . Figure taken from (Aude Alapini Odunlade, PhD Thesis, Chapter 1)

planets. Planets in this region receive strong radiation from the star due to which the atmosphere of the planet evaporates over time leaving behind a small rocky core. This gap is referred to as Hot Neptune Desert[49] which certainly is not an observational bias as inferred from the observations till now. Astronomers have not detected Neptune size planets below orbital periods of 10 days (see Fig. 1.2), instead they have detected some purely rocky super-Earths with no atmosphere and mini-Neptunes that are in the transition of atmospheric evaporation. These class of planets so close to their hot stars indicates that hot Neptunes once present or migrated in that region, are subjected to high irradiation from the star, which over some time makes them lose their atmospheres.

### 1.1.1 Orbital Parameters

Knowing the orbital architecture of a planetary system is one of the important steps in understanding the shape and characteristics of a light curve. From Figure 1.4, we can picture a planet in an eccentric orbit with eccentricity ( $e$ ) and orbit inclined at an angle ( $i$ ) with the plane of the sky as viewed from Earth. Among other parameters, ( $\omega$ ) is the argument of periastron; It is the angular position of the periastron from the ascending node, ( $r$ ) is the distance between the planet and the star, ( $a$ ) is the semi-major axis of the orbit, ( $\Omega$ ) is the angle between the North direction and the ascending node in the plane of the sky. This angle is also called the Longitude of the ascending node. ( $\nu$ ) is true anomaly; It is the angular separation between the planet's position and the periastron of the orbit.

A planet transiting in such (see Fig. 1.4) an orbital configuration would have a high probability of being detected if  $i \approx 90^\circ$  since the periastron of the planet is quite close in the direction of the observer, i.e Earth. In this configuration, transit duration would be shorter compared to a circular orbit with the same semi-major axis distance ( $a$ ) (see Fig. 1.4). Also, a transit event would not be highly sensitive to different orbital inclination angles compared to a circular case. There are more cases where a transit event is favoured in an eccentric orbit. For instance, orbital configurations with different argument of periastron ( $\omega = \pi/2, \pi, etc.$ ) i.e different orientation of the orbit. Since the projected distance between the star and the planet would be smaller compared to a circular case with the same period, a range of argument of periastron ( $\omega$ ) would favour a transit in such orbital configurations.

Using Kepler's first law, the star-planet distance ( $r$ ) at inferior conjunction can be written for an eccentric orbit as follows:

$$r = \frac{a(1 - e^2)}{1 + e \sin \omega} \quad (1.3)$$

A dimensionless parameter that defines projected star-planet distance and accounts for the effect of orbital inclination in modeling the transit light curve, is the Impact Parameter ( $b$ ). The impact parameter is the sky projected distance between the center of the planet and the host star when the planet is closest to the star. It is defined as follows:

$$b = \frac{a}{R_*} \left( \cos i \frac{(1 - e^2)}{1 + e \sin \omega} \right) \quad (1.4)$$

For occultation it would be  $(1 - e \sin \omega)$  in the denominator in both equation 1.3 & 1.4 and planet's position in the orbit would be superior conjunction.

Lower the impact parameter, planet transit along the longer chord of the stellar disc and when  $b = 0$ , the planet passes over the central chord of the star when the inclination is  $90^\circ$ . From Figure 1.5, we can see light curve in the dashed line. As the impact parameter is larger in this case,  $t_F$  and  $t_T$  decreases, ingress and egress duration increases and vice-versa for the light curve in solid line for which  $b = 0$ . When inclination gets closer to  $90^\circ$ , the impact parameter decreases and hence transit duration increases.

### 1.1.2 Light Curve

A transit light curve is a dip in the stellar flux as a planet passes over the stellar disc. Let's first discuss different parameters that characterize a light curve. From Figure 1.5,  $\Delta F$  is transit depth for two different light curves shown in dashed and solid lines.  $t_T$  is total transit duration i.e time taken by the planet to go from 1<sup>st</sup> to 4<sup>th</sup> contacts as depicted from gray circles representing planet,  $t_F$  is the duration between end of ingress and start of egress i.e from 2<sup>nd</sup> to 3<sup>rd</sup> contacts when the planet is completely superimposed

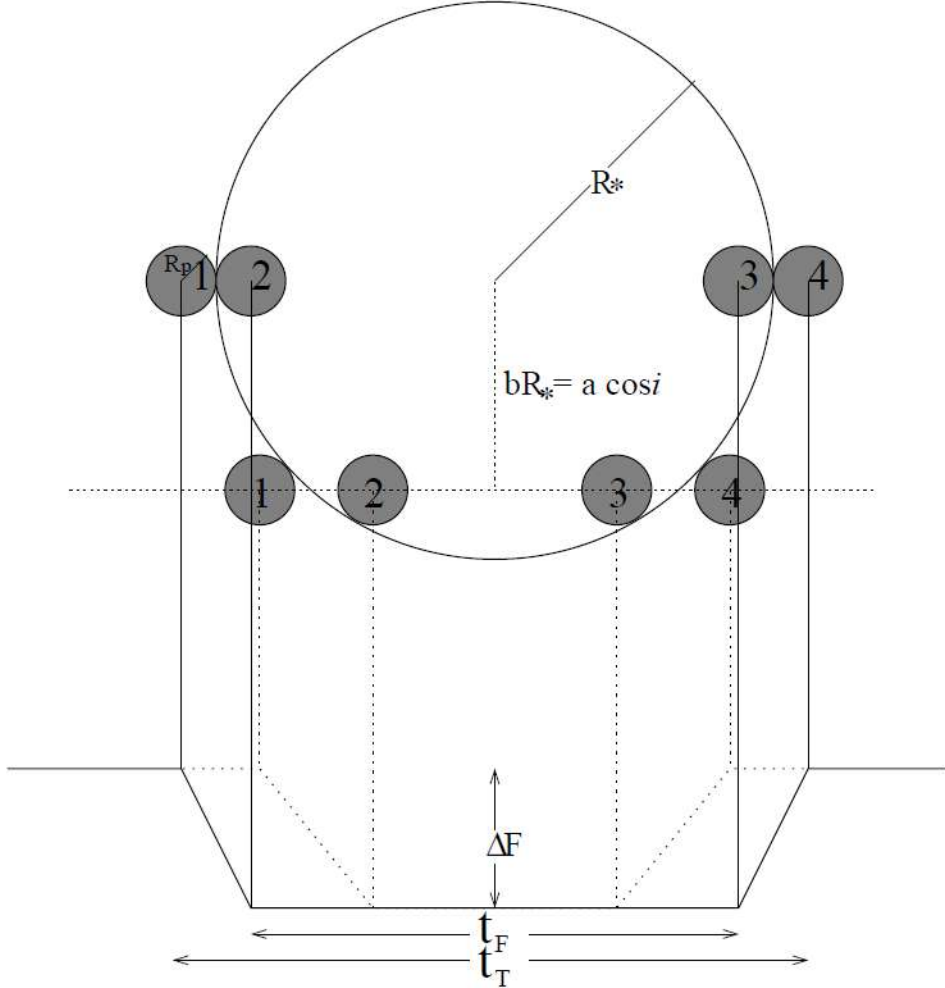


**Figure 1.5:** Schematic showing the effect of two different impact parameters ( $b$ ) on the shape of transit light curve (dashed and solid lines). In other words how it affects the total duration between ingress and egress ( $t_T$ ) and duration ( $t_F$ ) when the planet is completely superimposed on the stellar disc. Figure adapted from (Seager & Mallén-Ornelas), 2003.[43]

on the stellar disc.  $a$  is the semi-major axis and  $i$  is the inclination of the planet's orbital plane from the plane of the sky.

The depth of the transit dip is directly proportional to the projected area of the planet relative to that of the star which can be written as follows:

$$\frac{R_p^2}{R_*^2} \approx \Delta F \quad (1.5)$$

$\Delta F$  being an observable, we can first determine the relative size of the planet using equation 1.5. Constraining the absolute size of the planet is more complex as it requires stellar models to obtain an estimate of the stellar size. This in turn introduces additional uncertainty in the determined value. The transit light curve helps in constraining the planet's relative physical and orbital properties which include planet radius, semi-major

axis and inclination. Its shape and size are dependent on the stellar type, inclination, star-planet size and wavelength range of the observation.

Using geometry, we can also write  $t_T$  and  $t_F$  for a circular orbit case as follows:

$$t_T = \frac{P}{\pi} \arcsin \left( \frac{\sqrt{(R_* + R_p)^2 - (a \cos i)^2}}{a \sin i} \right) \quad (1.6)$$

$$t_F = \frac{P}{\pi} \arcsin \left( \frac{\sqrt{(R_* - R_p)^2 - (a \cos i)^2}}{a \sin i} \right) \quad (1.7)$$

Another observable parameter is Period ( $P$ ). To know the orbital period of a planet, at least two transits are required. The period can be determined by using a simple linear relation which is as follows:

$$P = \frac{t_n - t_1}{n} \quad (1.8)$$

where  $t_n$  and  $t_1$  are mid-transit time of  $n^{\text{th}}$  and first transit respectively and  $n$  is total number of planetary orbits that occurred between the  $n^{\text{th}}$  and the first transit.

After getting first relative parameter ( $\frac{R_p}{R_*}$ ), we can get ( $\frac{a}{R_*}$ ) by using equation 1.6 as follows:

$$\frac{a}{R_*} = \left[ \frac{(1 + \sqrt{\Delta F})^2 - b^2(1 - (\sin^2 \frac{t_T \pi}{P}))}{\sin^2 \frac{t_T \pi}{P}} \right]^{1/2} \quad (1.9)$$

In equation 1.9 all parameters are known except  $b$  i.e impact parameter which is sky projected distance between star and planet at mid-transit time can be derived by dividing equation 1.7 by equation 1.6 and using equation 1.5. It can be written as follows:

$$b = \left[ \frac{(1 - \sqrt{\Delta F})^2 - \frac{\sin^2 \frac{t_F \pi}{P}}{\sin^2 \frac{t_T \pi}{P}}((1 + \sqrt{\Delta F})^2)}{\frac{\sin^2 \frac{t_F \pi}{P}}{\sin^2 \frac{t_T \pi}{P}}} \right] \quad (1.10)$$

Lastly, orbital inclination ( $i$ ) can be calculated once we know ( $b$ ):

$$i = \arccos \left( \frac{b R_*}{a} \right) \quad (1.11)$$

Except equation 1.8, equation 1.5-1.11 are analytical solution based on transit geometry. These equations do not take into account the limb darkening effect. Finally, we see four observables  $\Delta F$ ,  $t_T$ ,  $t_F$  and  $P$  with which we can get all relative physical parameters as discussed above.

### 1.1.3 Stellar Limb Darkening

The light curve shape is also dependent on the limb darkening of the star, which is more prominently visible if we observe the star at different wavelengths for a better comparison. But firstly, let's discuss limb darkening.

Stellar limb darkening is a phenomenon in which a stellar disc appears less bright as we gradually move away from the center toward the edges. It is caused due to variations in temperature and opacity with different depths in the stellar atmosphere. When we look at the center, we are looking at an optical depth nearly equal to 1 and beyond that, we can't see as it becomes opaque. When we look at the limb, we are looking at some large slant angle and therefore at the same optical depth of 1, we are able to probe relatively cooler regions as the temperature there is lower compared to the center making the limb appear darker. This effect was first observed on the Sun by (Schwarzschild & Villiger) in 1906.

The effect of limb darkening changes the shape of the light curve. When a planet passes over the limb region, it causes a progressive drop in the stellar flux compared to a sharp drop in the inner regions of the stellar disk. From Figure 1.6, we can see this effect very prominently as the light curve is getting more “U” shaped as the wavelength of the observation decreases from 1030 nm (top) to 290 nm (bottom) because this effect gets more prominent at lower wavelengths.

To account for this effect in modeling light curve, there are some functions which could be used for different types of stars. One of the very basic function is as follows:

$$\frac{I(\theta)}{I(\theta = 0)} = 1 - B(1 - \cos \theta) \quad (1.12)$$

where  $I(\theta)$  is the intensity of light as seen by an observer at angle  $\theta$ . It is the angle between the normal to the stellar surface and the line of sight of the observer.  $I(\theta = 0)$  is the intensity of light at the center of the stellar disk,  $B$  is the wavelength-dependent limb darkening coefficient. There are numerous such functions and one of the most used is quadratic limb darkening law, as it gives good results with different types of stars. This function was given by (Manduca et al.), 1977.[32]

$$\frac{I(\mu)}{I(0)} = 1 - A(1 - \mu) - B(1 - \mu^2) \quad (1.13)$$

where  $\mu$  is  $\cos \theta$ ,  $A$  and  $B$  are limb darkening coefficients.

## 1.2 Secondary Eclipse & Phase Curve

A planet orbiting its host star undergoes gradual change of its phases just like we see different phases of the Moon. Its passage behind the star is called secondary eclipse or

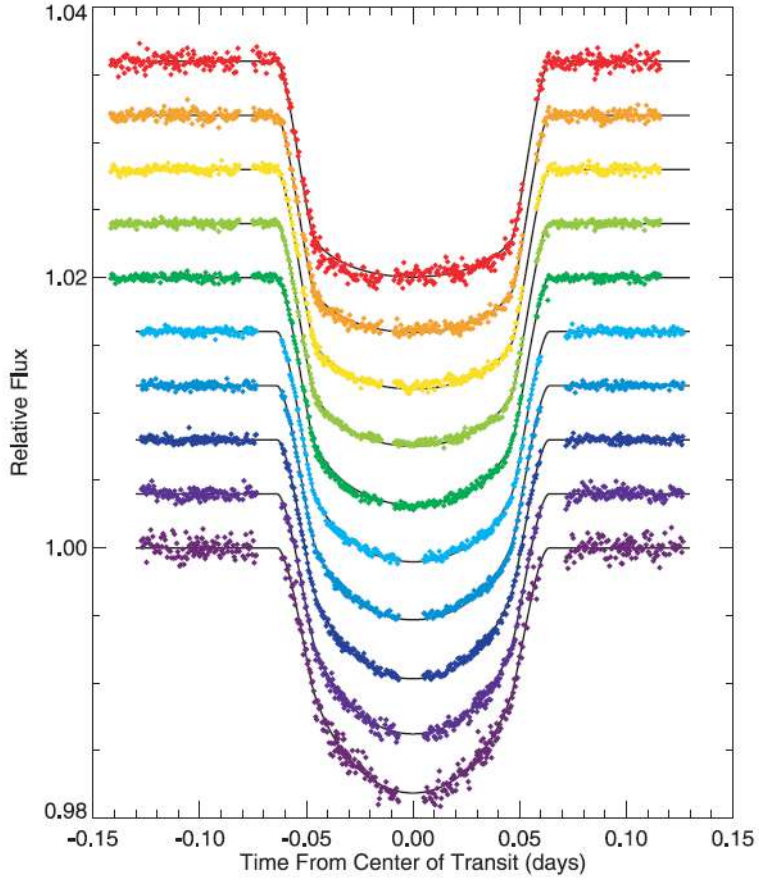


**Figure 1.6:** Light curves and their best fit model for HD 209458 b observed at 10 different wavelengths showing different shapes. This demonstrates how the limb darkening effect is wavelength dependent. As we go from higher to lower wavelength, the effect gets prominent and the light curve gets more ‘U’ shaped. Figure taken from (Knutson et al.), 2007.[25]

occultation. The probability of secondary eclipse for a circular orbit would be same as that of transit but for an eccentric orbit it is given as follows:

$$P_{\text{secondary}} = \frac{R_* + R_p}{a} \left( \frac{1 + e \cos(\frac{3\pi}{2} - \omega)}{1 - e^2} \right) \quad (1.14)$$

where  $e$  is the eccentricity of the orbit,  $\omega$  is the argument of the periastron and  $\theta = \frac{3\pi}{2}$ , is the angular position of the planet in the orbit measured from the reference sky plane. Transit probability for an eccentric orbit would be given by the above equation where  $\theta = \frac{\pi}{2}$ .

Planet at the time of mid-transit is just like a new moon and when it is almost behind the star, it is like a full moon reflecting its host starlight. This emitted flux is not just flux from reflected light, but it is a combination of fluxes from three different components as given by equation 1.15. Where thermal emission is the light which was absorbed by the planet and re-emitted at a different wavelength and internal heat usually comes from tidal activity or can be leftover from the system formation.

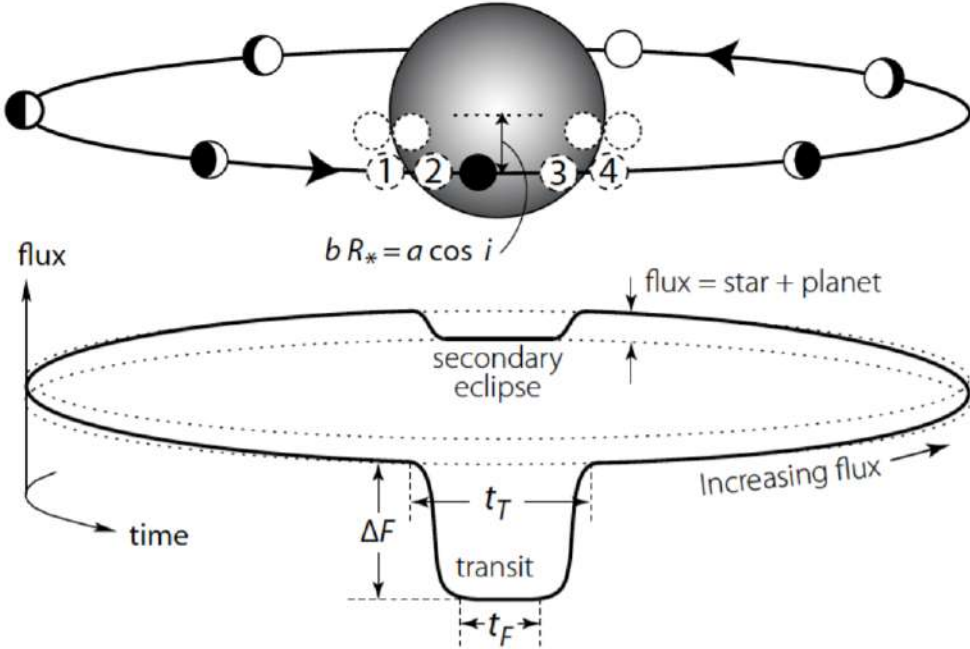


**Figure 1.7:** Schematic of a full light curve showing both transit and secondary eclipse along with the variation of total flux i.e. flux from the star and the planet as it orbits. Particularly, when the planet goes behind the star, light (both reflected and thermal) from the planet does not reach the observer, thus causing an eclipse. Figure taken from (Winn et al.), 2010.[57]

$$F_p = F_{\text{star, reflected by planet}} + F_{\text{p, thermal}} + F_{\text{p, internal}} \quad (1.15)$$

As the planet goes gradually from transit to occultation, it imprints the variation of this emitted flux which forms the planetary phase curve (see Fig. 1.8). From Figure 1.7, it can be seen as a gradual increase and decrease in total (star + planet) flux. When the planet is behind the star, the light from it is absent and thus we see only stellar light. This produces a flux drop at the time of the eclipse. The amplitude of this smaller dip tells how much light is emitted only by the planet because the combined star and planet flux is observed before the planet goes behind the star and thus we see only flux from the star. If the emitted light comes only from the reflected stellar light and planet's thermal flux, we can express the depth of secondary eclipse  $\Delta F_s$ , as follows:

$$\frac{F_p}{F_*} = A_g(\lambda) \left( \frac{R_p}{a_s} \right)^2 + \left( \frac{R_p}{R_*} \right)^2 \frac{\int_{\lambda=0}^{\lambda=\infty} B_\lambda(T_p) \tau(\lambda) d\lambda}{\int_{\lambda=0}^{\lambda=\infty} B_\lambda(T_*) \tau(\lambda) d\lambda} \quad (1.16)$$

where,  $F_p$  and  $F_*$  are total fluxes from the day side of the planet and the star respectively,  $A_g$  is wavelength-dependent geometric albedo,  $R_p$  is the planet radius and  $a_s$  is the star-planet distance at the time of secondary eclipse. The first term in the above equation gives the contribution from reflected light in the occultation depth. The second term accounts for emitted thermal flux.  $R_*$  is the stellar radius, the terms in the integral should be emission spectra of the planet and the star but for simplification, they are

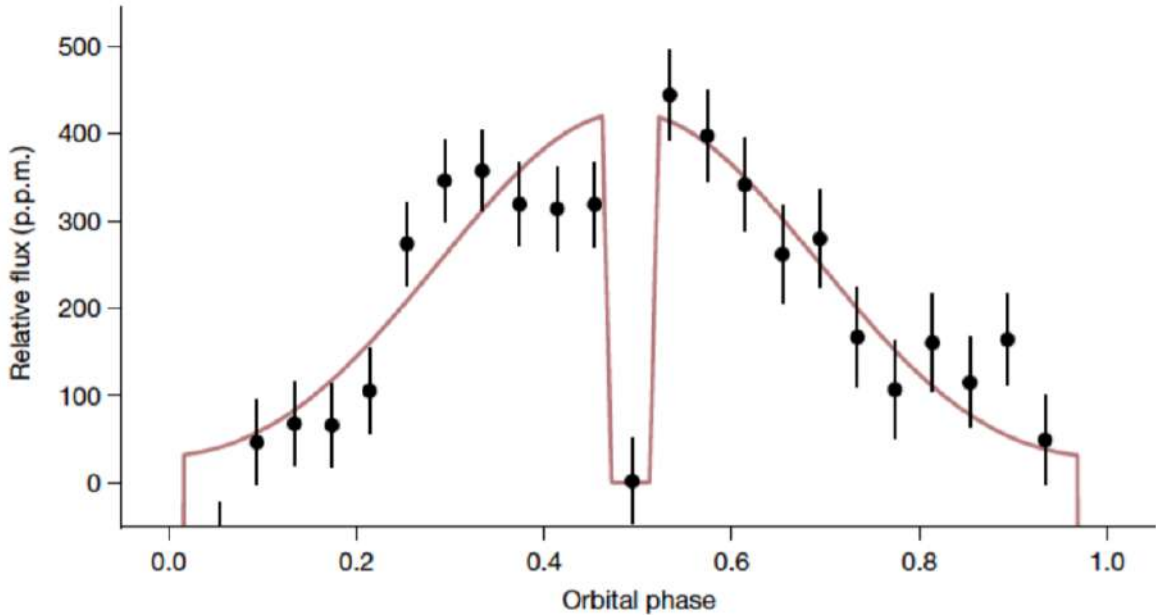


**Figure 1.8:** Phase curve of LHS3844b centered at secondary eclipse, data was taken from Spitzer space telescope. As more and more area of the planet facing us reflect light, we see an increase in planetary flux, it does not reach the observer when the planet is behind the star at 0.5 orbital phase. Figure adapted from (Kreidberg et al.), 2019.[28]

approximated as blackbodies  $B_\lambda(T_p)$  and  $B_\lambda(T_*)$ . Lastly,  $\tau(\lambda)$  is the transmission function of the TESS over which fluxes are integrated and thus the 2<sup>nd</sup> term in this equation gives the contribution of thermal flux in the occultation depth. For  $T_*$  and  $T_p$  we can use the effective temperature of the star and equilibrium temperature  $T_{eq}$  of the planet, respectively.

Equilibrium Temperature ( $T_{eq}$ ) is the temperature of a planet, assuming it to be a blackbody where it is heated only by the star.  $T_{eq}$  is more of a theoretical temperature for a planet assuming no atmosphere and thus no account for the greenhouse effect and cloud cover. These factors affect the temperature of the planet. We can calculate  $T_{eq}$  using  $T_*$  as follows:

$$T_{eq} = T_* \sqrt{\frac{R_*}{2a}} (f(1 - A_B))^{1/4} \quad (1.17)$$

where  $T_{eq}$  is the equilibrium temperature of the planet,  $a$  is the semi-major axis,  $A_B$  is bond albedo which defines the fraction of incident stellar flux scattered back into space by the planet and  $f$  is a proxy for atmosphere circulation as defined by Seager et al. 2005 [44].  $f = 1$  is adopted for efficient atmosphere circulation possibly due to strong winds where the planet re-emits radiation into  $4\pi$  sr. For no circulation case i.e  $f = 2$ , in this case only the irradiated day side re-emits into  $2\pi$  sr, in that case,  $T_{eq}$  is defined only for the day side.

Equation 1.16 gives expected occultation depth from thermal and reflective compo-

ment. We can use their sum and compare it with the values retrieved from data analysis, which help in constraining geometric albedo  $A_g$ , inference on clouds in the atmosphere and for estimating upper limits on several physical parameters. In chapter 3, we discuss it in more detail.

Further, we can calculate the brightness temperature  $T_b$  of the planet. It is the temperature at which a blackbody emit the flux equivalent at a given wavelength. Using occultation depth ( $f_p$ ), we can calculate this temperature by modifying the 2<sup>nd</sup> part of the equation 1.16 as follows:

$$T_b(\lambda) = \left( \frac{hc}{\lambda k_B} \right) \left( \ln \left( 1 + \frac{2hc^2k^2}{f_p \lambda^5 B_\lambda(T_*)} \right) \right)^{-1} \quad (1.18)$$

Where  $h$  is plank constant,  $c$  is the speed of light in vacuum,  $\lambda$  is specific wavelength,  $k_B$  is Steffan–Boltzmann constant,  $f_p$  is occultation depth and  $B_\lambda(T_*)$  is Plank function for star and  $k^2$  is radius ratio squared ( $R_p/R_*$ )<sup>2</sup>. Since we now can estimate  $T_{eq}$  and  $T_b$ , we can use their ratio i.e  $T_{eq}/T_b$  to constrain contribution from the reflected light along with inference on any other source that contributes in the reflected light.

Since the secondary eclipse depth thus depends on all three components as mentioned in equation 11, in case if planet's heating due to tidal forces or contraction also contributes, then the overall emitted flux would be more than what the planet received from the star. This will make the secondary eclipse dip deeper. We can identify such a case where the observed occultation depth is more than the expected one from equation 1.16. In chapter 2 and further, we will not deal with the full phase curve except for the secondary eclipse as it is beyond the scope of this thesis work. The shape and amplitude of the phase curve are affected by the presence of clouds, winds and composition in the upper atmosphere. Therefore, its proper characterization helps in constraining the physical properties of hot Jupiters.

### 1.3 Transiting Exoplanet Survey Satellite (TESS)

TESS is a space-based telescope which was launched on April 18, 2018, Ricker et al. 2015 [42]. It is an all-sky survey mission which aims to detect transiting exoplanets around bright stars. Planets smaller than Neptune are its main target and a subset of which will be observed by the currently running CHEOPS and upcoming missions like JWST. Follow-up for further spectroscopic observation could help in constraining planet mass and atmospheric composition. TESS is orbiting Earth in 2:1 resonance with the Moon in a highly elliptical orbit. It completes one orbit around Earth in 13.7 days. This orbital setup keeps the telescope away from interference from Earth for good observation and keeps the orbit stable for many years.

TESS is equipped with four wide-angle cameras. Each covers a  $24^\circ \times 24^\circ$  degree field of view. Each camera is equipped with four 2k x 2k CCDs. The two-year nominal mission

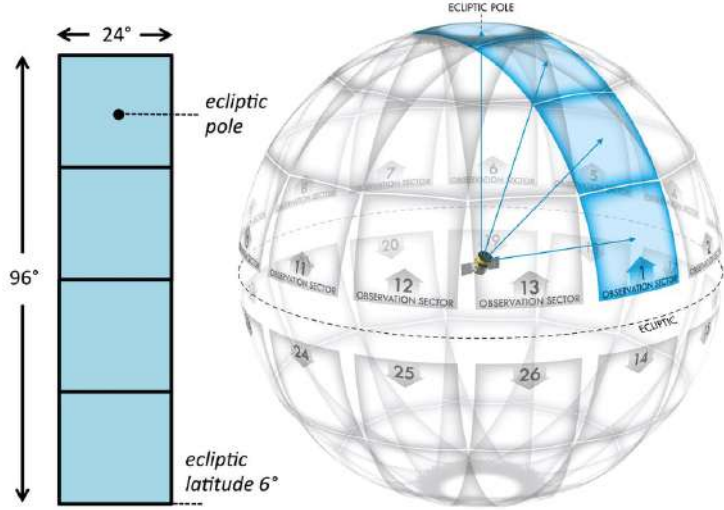


**Figure 1.9:** Figure (left) shows Field of View (FOV) coverage by all four CCD cameras onboard TESS and the figure on right shows different sectors on the sky map along with overlapping viewing zone of TESS.

was divided into 26 sectors as depicted in Figure 1.9. Each sector covers a total of  $24^\circ \times 96^\circ$  in the sky and one such sector is observed for two orbits or 27.4 days. The observation is done in 600 nm - 1000 nm of wavelength bands. The data are relayed back to Earth every 13.7 days, every time as it approaches the perigee of its orbit.[21]

More than 200 exoplanets have been confirmed since the first detection [22] of a planet  $\pi$  Men *c*, a super-Earth orbiting a G-type star. There are more than 5000 TESS Object of Interest (TOI) that will probably provide more such rocky planets for further investigation.

# Chapter 2

## Analysis of WASP-33b

In the chapter 1, we discussed the history of exoplanet research, statistics, transit light curve and how its shape and size are impacted by different physical parameters. In this chapter, we analyse the data of WASP-33b, a hot Jupiter orbiting a Delta Scuti variable star in about 1.22 days. This planet has been extensively studied with more than 70 research<sup>1</sup> publications to date. Being a highly irradiated and one of the hottest and well studied among hot Jupiters, its analysis is a test bed for the rest of the 28 hot Jupiters that we discuss in Chapter 3.

WASP-33b has a day side and night side temperature of about 3200 K and 1757 K respectively Zhang et al. 2018. It is subjected to mass loss from the upper atmosphere. D. Ehrenreich & J.-M. Desert 2011 [15] calculated this mass loss rate due to X-ray and UV radiation from the host star. Nikku Madhusudhan 2012[31], characterized the thermal structure and calculated the C/O ratio. Smith et al. 2011 [46] studied thermal emission and concluded inefficient heat redistribution from the day side to the night side. Many molecules have been detected in the atmosphere of WASP-33 b, with recent ones including Fe and Si and evidence for TiO Cont et al. 2021, 2022 [11][12]. Most of these studies were mainly based on spectroscopic observations. In this thesis, we only deal with the photometric observations of hot Jupiters with an aim to find targets that show robust secondary eclipse depth to be observed with higher photometric precision with CHEOPS. The methodology applied in analyzing this target is used for the rest of the 29 targets.

### 2.1 Data

WASP-33 b was discovered by Collier Cameron, A. et al. 2010 [10] with the ground-based facility SuperWASP. It was later observed by TESS in sector 18. For the analysis, we download the 2 min cadence data from MAST. MAST archive provides light curve data in two formats, namely SAP<sup>2</sup> and PDCSAP<sup>3</sup>. SAP is raw data, whereas PDCSAP is detrended from systematic noise using NASA's TESS data processing pipeline called

---

<sup>1</sup>(Publications)on WASP-33 b

<sup>2</sup>SAP: Simple Aperture Photometry flux

<sup>3</sup>PDCSAP: Pre-search Data Conditioning SAP flux

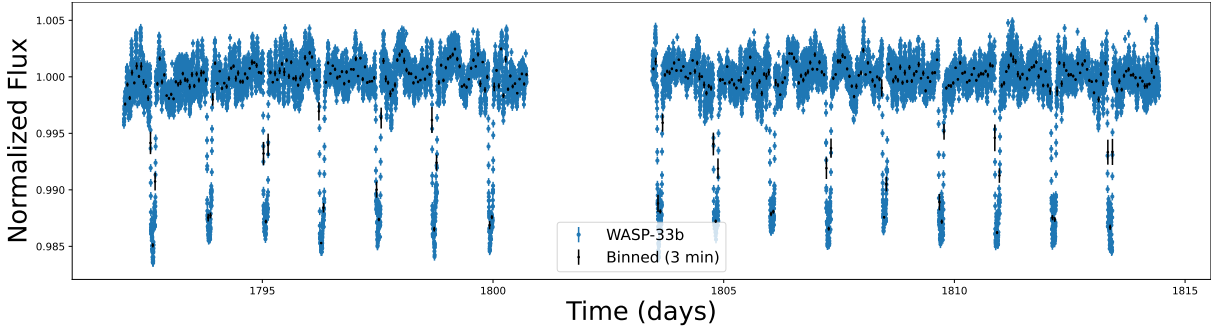


**Figure 2.1:** WASP-33b data from sector 18 of TESS showing 16 transits. The very first transit is removed as it's depth is not consistent after initial inspection. The data is normalized and overplotted in black points is binned data with 3 min bin size.

SPOC<sup>4</sup>. Although this seems an advantage, it may come at a cost for other targets where PDCSAP detrending might remove eclipse signal from the data itself. So for the rest of the targets, we use SAP flux as well. For modeling the correlated noise, we use Gaussian Processes. As of now, let's see the analysis of WASP-33 b.

### 2.1.1 Lomb-Scargle Periodogram & BLS model

The analysis of WASP-33 b begins with Lomb-Scargle (L-S) Periodogram Press W.H. and Rybicki 1989 [41]. It is an established algorithm that uses Discrete Fourier Transform to detect periodic signals in unevenly spaced data. Although TESS should ideally take data at an even interval of 2 minutes, in reality, this condition is not achieved due to limitations of electronics, when TESS instead of observing, transmits the data back to Earth in between two orbits and due to discarded data points (see Fig. 2.1). To deal with unevenly spaced data, we use an L-S periodogram which decomposes a time-series data into a linear combination of sinusoidal functions. This way the data is transformed from the time domain to the frequency domain. Apart from frequency pertaining to the planet's orbital period, a periodogram is used to explore frequencies that might be originating from stellar activity and pulsation which are correlated with the stellar rotation. Identifying such frequencies helps better detrend both PDCSAP and SAP data 3.2.1.

Another periodogram (see Fig. 2.2) or window function in black is used to see possible frequencies that might be resulting from the sampling of the data. To compute it, we create an evenly spaced 2 min resolution data by filling corresponding gaps with zeros and replacing flux values with ones. The highest peak (marked with magenta dashdot line) around 1.2193 days from the window function tells this period indeed belongs to WASP-33 b. This peak is a good example of the effect of sampling as a peak pertaining to the planet's period is not seen in the periodogram (green) of the actual data without in-transit data points. So the gaps created after removing in-transit data have a periodicity of the planet's actual period. In both the periodograms, we use Nyquist frequency i.e  $0.5 \times$  sampling frequency of the data to find frequencies of interest as mentioned above

---

<sup>4</sup>SPOC: Science Processing Operations Center

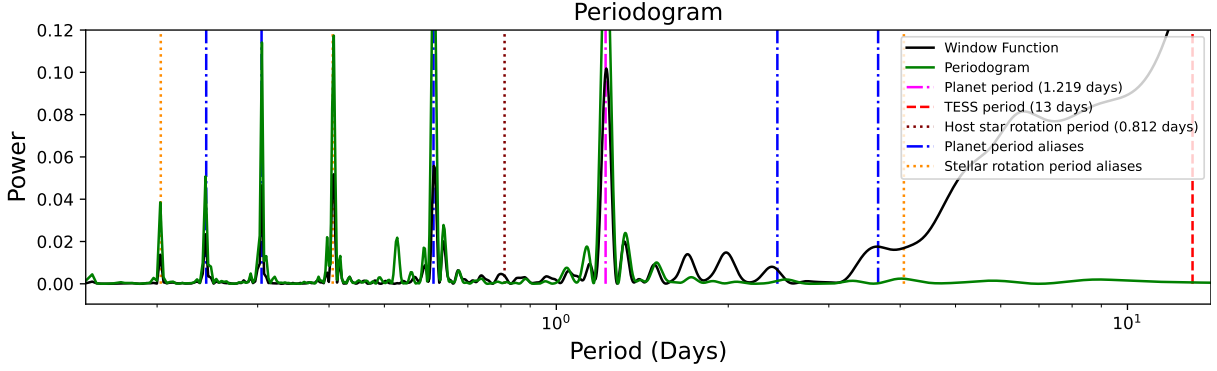


**Figure 2.2:** Lomb-Scargle periodogram (green) is used to explore different frequencies to identify period especially pertaining to WASP-33b. Another periodogram (black) also called window function is also explored to validate if the peak pertaining to the planet's period indeed belongs to the planet and is not an effect of sampling. Apart from this, peaks associated with aliases of the planet's orbital period, TESS orbital period and stellar rotation period are also identified.

while ensuring to capture the activity of frequencies as high as 1/4minutes.

Apart from peaks resulting from the planetary transits, TESS orbital period and stellar activity correlated with stellar rotation, there are numerous other peaks as can be seen from figure 2.2. Most of them are harmonics of a peak associated with the planet's orbital period, stellar rotation/pulsation and TESS orbital period. These aliases are calculated by dividing/multiplying the period of interest by non-zero positive numbers. After identifying the period pertaining to the planet, we estimate the values of the relative physical parameters 2.1.2 using the Box Least Square (BLS) model Kovács et al. 2002 [26] and use least square regression 2.2 for fitting the model which can be described mathematically as follows:

$$\hat{\theta} = \operatorname{argmin} \left[ \chi^2(\theta) \right] \quad (2.1)$$

$$\hat{\theta} = (A^T V^{-1} A)^{-1} A^T V^{-1} y \quad (2.2)$$

where  $\hat{\theta}$  are estimated parameters,  $\theta$  initial guess parameters of the model which are adjusted by minimizing  $\chi^2$ ,  $A$  is the basis matrix and  $V$  is covariance matrix whose diagonal terms are variances and non-diagonal terms are kept zero assuming no covariances between data points. As the name suggests, it is a statistical method to find a best fit model that could explain the data. Here data-model comparison is based on  $\chi^2$  and its minimization, minimizes the squared distance between the data and the model to obtain adjusted parameters of the model.

The BLS model propagates an upside-down hat-shaped signal through the data to find a dip potentially due to a transiting planet. This model indeed confirms the presence of WASP-33b but it does not take into account the effect of limb darkening 1.6, orbital

inclination, eccentricity and argument of periastron. Therefore, the estimated parameters from the fitting are not precise. So, a good model is required which could provide better constraints on the estimated parameters along with their uncertainties. Here, we choose BATMAN model 2.1.2 for further analysis.

### 2.1.2 BATMAN model

The BAsic Transit Model cAlculatioN (BATMAN) Laura Kreidberg 2015 [27] is a python package for modeling transit light curve. We have numerous similar packages on the market(PyTransit, Hannu Parviainen [39]). BATMAN compared to the BLS model, takes into account the impact of all the parameters on the shape and size of the model light curve. Parameters of the full model light curve that are fitted: The epoch time or the mid-transit time ( $T_0$ ), the orbital period of the planet ( $P$ ), the relative radii ratio of the planet to star ( $r_p$ ), the semi-major axis in units of stellar radius ( $a$ ), the orbital inclination of the planet ( $i$ ), the flux ratio of the planet to star ( $f_p$ ) or occultation depth, an offset parameter  $f$  for model and an adjusting parameter ( $s$ ) which accounts for any linear slope in the data. Besides, three parameters, orbital eccentricity ( $e$ ) argument of periastron ( $\omega$ ) and limb darkening coefficients ( $[u_1, u_2]$ ) are fixed and are taken from previous literature. In some of the cases, where we don't find any references, we take ( $[u_1, u_2]$ ) from other TESS targets where the host star closely matches the properties of our target star.

When using a Bayesian approach 2.5, parameters of a model are sampled from a desired probability distribution. To explore the parameter space, a Markov chain Monte Carlo (MCMC) algorithm used is implemented with the EMCEE package Foreman-Mackey et al. 2013 [19]. We then retrieve the most likely parameters along with their uncertainties. Before we further move on to how all of this is implemented, let's discuss a bit about our light curve model.

Recall from section 2.1.2, a full light curve model is composed of three components: Transit, secondary eclipse and planetary phase curve model. With the BATMAN package, we compute the transit model by specifying numerous parameters as discussed above. The eclipse model is computed with the help of the transit model by specifying  $f_p$  i.e depth of secondary eclipse or flux ratio of the planet to star at the mid-eclipse time. The mid-eclipse time is predicted with the ephemeris of the transit model. For the phase curve, we approximate it with a sinusoidal function whose main goal is to bridge the other two models in the full light curve. A major assumption here is that the planet's light is uniformly reflected by the surface. Finally, all the three models are combined as follows:

$$Model = TM + (SEM - 1) \times PPV \quad (2.3)$$

Where TM is Transit Model, SEM is the Secondary Eclipse Model and PPV is Planetary Phase Variation or phase curve model. Where PPV is approximated as follows:

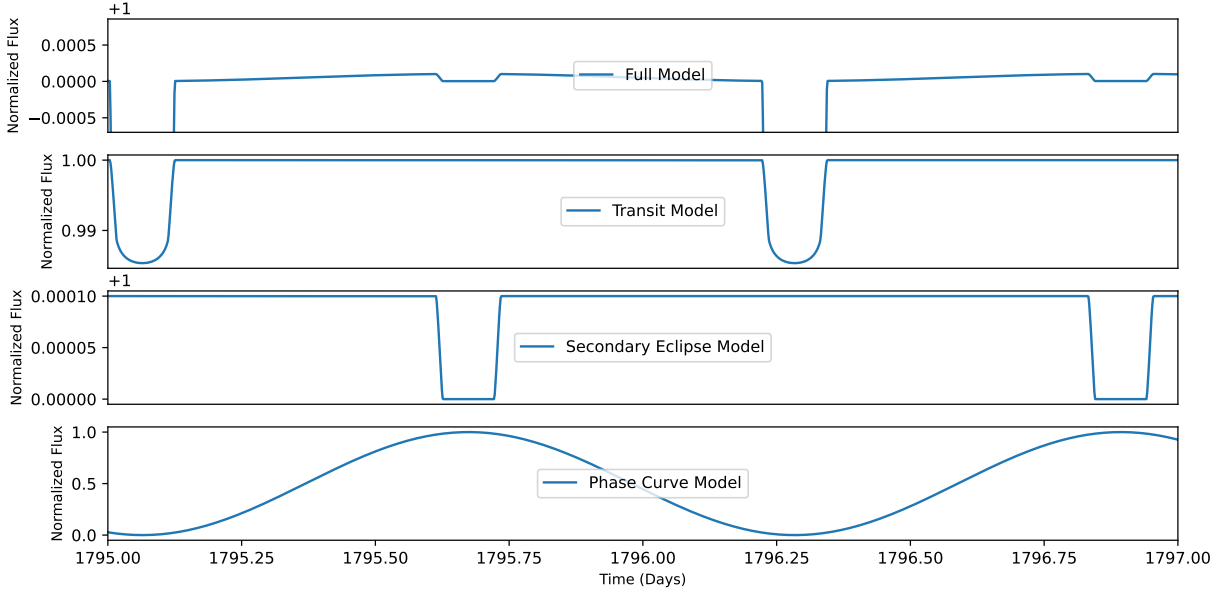


**Figure 2.3:** Full model (top) of light curve along with model components i.e transit, secondary eclipse and phase curve model.

$$PPV = \frac{(1 - \cos(\frac{2\pi(t-t_0)}{P}))}{2} \quad (2.4)$$

here ( $t$ ) is time and ( $P$ ) is orbital period of the planet, ( $t_0$ ) epoch time of any transit. We also include two normalizing parameters as discussed above. So, our final model using equation 2.3 & 2.4 along with adjusting parameters could be written as follows:

$$Full \text{ Model} = (s \times (t - t_0)) + (Model \times f)$$

where ( $f$ ) is an offset parameter as mentioned above and ( $s$ ) is an intrinsic linear slope in the data.

## 2.2 Model fitting with MCMC

Monte Carlo Markov Chain(MCMC) is a method used in sampling from a probability distribution. It can be used in Bayesian inference to obtain posterior probability distribution for a set of parameters of the model given data. MCMC implements random sampling such that the estimated value of the parameters converges toward the true value if sampling is done for a long time and with a large number of walkers. While sampling, a Markov chain draws samples in a correlated sequence of steps. The acceptance or rejection of a drawn sample depends on the state of the chain at the previous step and is done by calculating the ratio of posterior probability at both steps. If this ratio is greater than 1, then the chain accepts the sample and moves to the next step. If not, then a random number is generated between 0 and 1 and the ratio is compared to this random number. If the ratio is greater, the step is accepted and hence the new sample and if the

ratio is less than the random number, then the sample is rejected. Again chain draws new samples with the help of jump parameters and the whole process is repeated as described above. For the chains to not remain stuck at some local maxima, we run MCMC for a long time.

There are mainly four things required to do an MCMC analysis; Data, model, initial values of the parameters and jump parameters and as a result, we get a posterior distribution of the adjusted parameters. We can get best-fit values from the set of parameters that gives the highest posterior probability. While the parameter value and uncertainty are given by its median value along with 68% confidence interval which is  $1\sigma$  uncertainty. In MCMC, chains take some time to enter a region of high probability which is representative of the desired probability distribution that we are sampling from. Thus, we implement a burn-in step 4.3 to discard all those initial samples corresponding to low probability region and where the chains have not settled yet. To achieve convergence of Markov chains faster, we thus need a good starting point around a high probability region in parameter space 2.4.

Initial parameters are mainly used to initiate the MCMC chains nearby high probability region and thus we use BLS model parameters as a first guess and optimize them further using the BATMAN model using linear least square regression before running an MCMC. We implement this needed step using the minimize function from the `scipy.optimize` Virtanen et al. 2020 [51] package and adopted ‘L-BFGS-B’ algorithm along with simple bounds on the parameters. With successive iterations, this algorithm tries to refine the parameters of our full model.

Now let us understand how all of this work in a proper sequential manner, beginning with Bayes’ theorem. If we recall, we can write it as follows:

$$P(\theta|D) = \frac{P(D|\theta)P(\theta)}{P(D)} \quad (2.5)$$

Where  $P(\theta|D)$  is posterior probability of parameters given data,  $P(D|\theta)$  is probability of data as a function of model parameters,  $P(\theta)$  is prior probability of parameters and  $P(D)$  is probability of data or evidence itself.

The likelihood of  $\theta$  is the probability of obtaining data  $D$  assuming parameters  $\theta$  of the model i.e  $P(D|\theta)$ . In another way, we can also say the likelihood is the probability that the random noise variable  $\epsilon$  which is contamination in the data, takes the value of residuals. Assuming this noise has a gaussian distribution with independent errorbars, ( $\mathcal{L}$ ) can be written as follows:

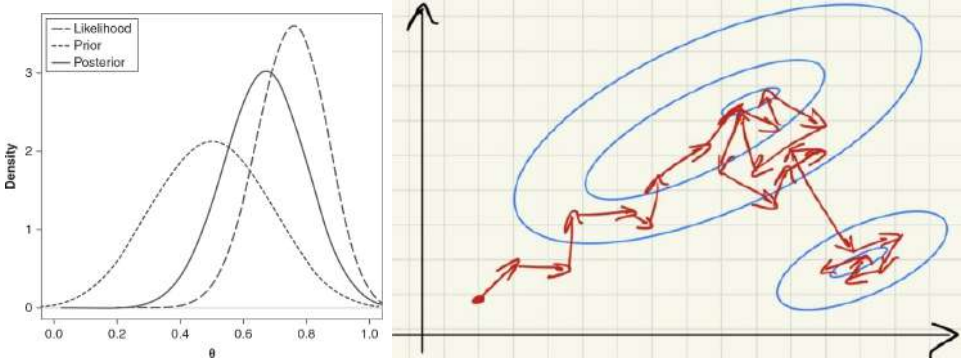


**Figure 2.4:** Figure(left) shows how our prior belief on parameters as prior probability combined with likelihood help better our belief on parameters ( $\theta$ ) as seen from posteriors. Also, instead of exploring a very broad region covering both prior and likelihood, a common and much smaller region in parameters space is explored by MCMC. Figure(right) shows the propagation of a chain in the parameter space along with local(bottom right) and global maxima (upper left). If chains start nearby a high probability region, MCMC converges faster.

$$\ln(\mathcal{L}(\theta)) = \ln P(\epsilon = y - m(\theta) | \theta) = -\frac{N}{2} \ln(2\pi) - \frac{1}{2} \sum_{i=1}^N \ln(\sigma_i^2) - \underbrace{\frac{1}{2} \sum_{i=1}^N \frac{(y - m(\theta))^2}{\sigma_i^2}}_{\chi^2} \quad (2.6)$$

Where  $\sigma_i^2$  are variances of  $N$  data points,  $m(\theta)$  is the full model and  $\chi^2$  is a merit function that compares data and the model. Minimizing  $(\chi^2)$  (see section 2.1) would minimize the squared distance between them and yield the parameters that best explain the data with the model based on those adjusted parameters. Minimizing  $\chi^2$  is akin to maximising the loglikelihood ( $\mathcal{L}$ ) or minimizing the negative of loglikelihood. In practice, we implement the latter form for ease of computation. We solve for the log of likelihood because the product of a large set of small probabilities may underflow the numerical precision of the computer. After adding the log of prior probability with loglikelihood, we get the log probability i.e  $\ln P(\theta|D)$ .

When executing the MCMC, we also need to define the number of walkers/chains which explore the parameter space and the number of steps. Each chain starts with adjusted parameters retrieved from least square regression as discussed above. For the chains to better explore the parameter space, each parameter is slightly changed randomly using jump parameters. Prior probabilities assumed for the parameters restrict the chains from exploring undesirable areas in the parameter space and thus save time. Defining priors could play a crucial role especially when the data is sparse. We use the EMCEE package to run an MCMC where all chains start at the same time and each explores all the parameters of the model. Thus the whole exploration of the parameter space becomes multi-dimensional.

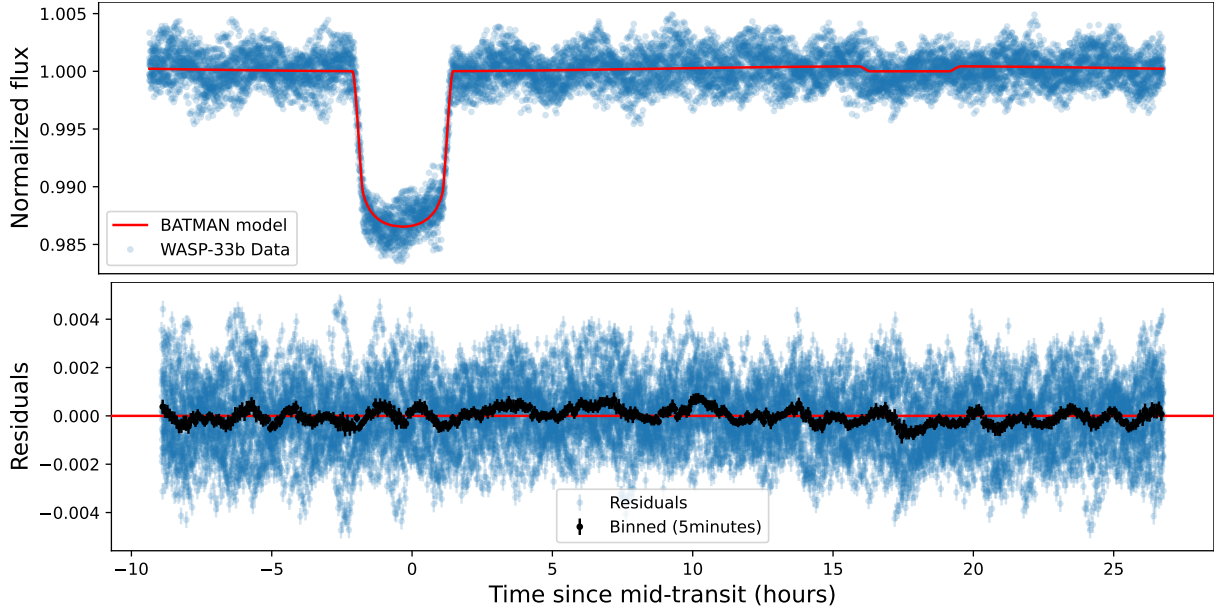


**Figure 2.5:** Figure showing best fit full model (BATMAN) plotted over phase folded data (top) and corresponding residuals (bottom) which shows correlated noise present in the data.

For analyzing WASP-33 b data, we use a total of 8 parameters in which 3 parameters namely  $\omega$ ,  $e$  and  $[u_1, u_2]$  (limb darkening coefficients) are kept fixed. A Quadratic limb darkening law is implemented and values of  $(u_1, u_2)$  are taken from Essen et al. 2021 who also used TESS data. Assuming a circular orbit,  $\omega$  can be fixed to any value as it is not defined for a circular orbit and  $e$  is fixed to 0. Two parameters  $f$  and  $s$  were mainly adjusting parameters where  $f$  keeps the baseline model (Normalized stellar flux only) to values of 1 and  $s$  fit for any intrinsic linear slope in the data. Initial values of most of the parameters for the BATMAN model are taken from the results of the BLS fitting and uniform priors are applied to all the free parameters. A total of 3000 steps and 48 walkers are used in MCMC analysis. Results (see table 4.1) from BATMAN fit (see section 2.5) is certainly far better than those from BLS. The fitted model seems to work well at first, however, we see correlated noise as revealed from the binned (black) data points.

In the beginning, we mention that the WASP-33 is a pulsating star and now it is quite evident from residuals based on BATMAN model analysis. This correlated noise mostly coming from different pulsation modes is captured by the residuals and can be seen as wiggles around the zero-line in the phase folded plot (see Fig. 2.5). This tells us that the best fit value of  $f_p = 446 \pm 9$  ppm (flux ratio) may be precise but with small uncertainty of about 9 ppm, it could be highly biased. It is necessary to account for this correlated noise in the analysis to obtain unbiased results.

From the above modeling and fitting experience, we can say, astronomical data is composed of three components: True planetary signal, correlated noise and uncorrelated/white noise. The latter two components make it hard to have a perfect model for the underlying true signal. The last component is not something that one can model.

There is only correlated noise that we can model to obtain better constraints on the parameters and accurate uncertainties on them after the fitting process. Modeling correlated noise could be well accomplished by Gaussian Processes (see section 2.3).

## 2.3 Gaussian Processes

Gaussian Processes is an infinite collection of random variables, such that the joint distribution of every finite subset of random variables is a multivariate gaussian distribution. It is a non-parametric method of modeling the data. Therefore, GP is applied over residuals i.e after removing all data that is modeled by a parametric model such as transit model (see section 2.1.2). It is conditioned by specifying training data to retrieve proper models. In the case of WASP-33b, data pertaining to the parametric model is removed by subtracting full model (see Fig. 2.9) from the original data before computing a GP.

The parameters of a Gaussian model are its mean function ( $\mu$ ) parameterized by  $\theta$ . This mean function is BATMAN model (see Fig. 2.9) described in equation 2.3 and the covariance or kernel function ( $K$ ) is parameterized by hyperparameters ( $\alpha$ ). A kernel is specified by its hyperparameters which describe the covariances between data points. For a time-series data, two data points are correlated in time, so the kernel finds covariances between two data points at the time, let's say  $t_1$  and  $t_2$ . The covariance function is used to populate the non-diagonal terms of the covariance matrix (see equation 2.2) of our noise model (see equation 2.6). In the previous analysis with BATMAN-only model, we assume noise has a gaussian distribution with independent errorbars. Following this assumption, we keep the non-diagonal terms to zero and specify only the diagonal terms i.e variances. In the case of GP, we don't apply the same assumption. Instead, we fill these non-diagonal terms. The hyperparameters of the kernel function determine the way non-diagonal terms are populated to generate a covariance matrix. The likelihood function for a GP model can be written similarly with the main difference of using the covariance function instead of the covariance matrix as described in the likelihood (see equation 2.6) of the BATMAN model.

$$\ln \mathcal{L}(\theta, \alpha) = \ln p(y|\theta, \alpha) = -\frac{N}{2} \ln (2\pi) - \frac{1}{2} \ln (\det K_\alpha) - \frac{1}{2} (r_\theta^T K_\alpha^{-1} r_\theta) \quad (2.7)$$

Here  $K_\alpha$  is the covariance matrix,  $r_\theta$  is residuals obtained from data and the mean model.

### 2.3.1 GP Kernel

There are standard kernel functions on the market and depending upon the nature (long-term, short-term, periodic etc.) of correlations in the data, we use them accordingly. For example in the case of WASP-33b, since it's a strongly pulsating star, we use the SHO(Simple Harmonic Oscillator), a quasi-periodic kernel which captures correlated noise mostly induced by the stellar pulsations from WASP-33. Von Essen et al. 2021 report

more than 20 pulsation frequencies each modeled using sine and cosine functions. In our case, we employ a GP with an SHO kernel described using equation 2.9 to capture correlations induced due to these pulsations with the rotation of the star. We also use Matérn-3/2, a generalized kernel and results (see table 4.1) from both are consistent. These kernels have additive and multiplicative properties which could help in capturing more complex trends in the data. A Matérn-3/2 kernel function can be written as follows:

$$k(t_1, t_2) = \sigma^2 \left( 1 + \frac{\sqrt{3}(t_1 - t_2)}{\rho} \right) \exp \left( -\frac{\sqrt{3}(t_1 - t_2)}{\rho} \right) \quad (2.8)$$

where  $\sigma$  is the amplitude and  $\rho$  is the correlation length of the kernel. They are also called hyperparameters of the kernel and  $t_1, t_2$  for example are the times of two points whose position is predicted by the kernel by calculating covariance between them. The Matérn-3/2 kernel is usually employed for treating long-term trends in the data. There is another kernel, a stochastically-driven damped harmonic oscillator or SHO kernel whose PSD (Power Spectral Density) is written as:

$$S(w) = \sqrt{\frac{2}{\pi}} \frac{S_0 w_0^4}{(w^2 - w_0^2)^2 + w_0^2 w^2 / Q^2} \quad (2.9)$$

where  $\omega_0$  is the frequency of the undamped oscillator,  $Q$  is the quality factor of the oscillator and  $S_0$  is proportional to the power at  $\omega = \omega_0$ . Using different relations between these terms, mainly three hyperparameters are defined which parameterize the SHO kernel. They are amplitude  $\sigma$ , undamped period  $P$  and  $\tau$  which is the decay time constant, of the quasi-periodic kernel. This kernel is mainly used for dealing with stellar variability in the data such as stellar pulsations and any quasi-periodic activity whose periodicity decay over a certain time period.

We use Celerite Foreman-Mackey et al. 2017 [17] to implement modeling with GPs. Celerite is an algorithm for fast and scalable Gaussian Processes (GP) Regression in one dimension. We use the Celerite 2 Foreman-Mackey et al. 2017 [16] package which is an improved version of Celerite and finally perform joint modeling (GP+BATMAN) (see Fig. 2.8) of WASP-33b data. In the joint modeling and fitting, we also include a jitter term that is added quadratically to the variance of the data to account for underestimated errorbars due to extra white noise.

## 2.4 GP & BATMAN joint modeling and fitting

In the section 2.1.2, we have already implemented the BATMAN model and the results were quite encouraging but using the GP model along with BATMAN could help in obtaining better constraints on the estimated parameters and uncertainties on them. The joint analysis began with a first guess on the hyperparameters of the GP kernel. The first guess was based on a periodogram analysis and visual inspection of the data. Similar to BATMAN, an initial estimate of the joint model parameters were obtained from the least square regression. Then, we use an MCMC to retrieve the most likely parameters of

the joint model along with uncertainties. Once we obtained the median values, we fitted the data using the GP model computed from these parameters. With GP, we finally perform prediction of the whole WASP-33b data including for the big gap between orbit 1 and 2 along with the 1-sigma uncertainty region around the mean model.

### 2.4.1 Data binning and Error treatment

As mentioned in section 2.1.1, TESS in reality is not able to take data points ideally every 2 min for a 2-min cadence dataset due to gaps. In calculating the binned data and their corresponding error, we calculate the weighted mean of fluxes of each bin with bin size in units of time. Considering the real sampling rate of TESS, each bin of equal time interval will have a different number of data points( $y$ ) varying from bin to bin. The higher the number of points in each bin, the more precise should be its representative mean value. The weights( $w$ ) are calculated using variance( $\sigma$ ) on each data point.

$$y_{mean} = \frac{\sum_{i=1}^N w_i y_i}{\sum_{i=1}^N w_i} \quad \text{where : } w_i = \frac{1}{\sigma_i^2}$$

The errorbar of each binned point is calculated as weighted sample variance ( $\sigma_w$ ) where the variance of each bin is weighted based on the number of data points ( $N$ ) in each bin as follows:

$$y_{mean_{err}} = \frac{\sigma_w}{\sqrt{N}} \quad \text{where : } \sigma_w^2 = \frac{\sum_{i=1}^N w_i (y_i - y_{mean})^2}{\sum_{i=1}^N w_i}$$

and each binned data point is plotted at the mid-time of each bin as follows:

$$t_{mid} = \frac{t_{start} + t_{end}}{2}$$

### 2.4.2 GP model

In the introduction of GPs, we mentioned that it is a non-parametric method of modeling the data. So, first we subtract all three parametric models i.e full model composed of transit, eclipse and phase curve to obtain intermediate residuals. We use both Matern 3/2 and SHO kernel and the results (see table 4.1) obtained from both are well consistent with each other. However, in the final analysis, we only choose SHO kernel as it is specifically designed for capturing quasi-periodic signals. The SHO kernel takes three hyperparameters, amplitude ( $\sigma$ ), period ( $\rho$ ) and decay time constant ( $\tau$ ) of the quasi-periodic kernel.

With an initial guess on hyperparameters and BATMAN parameters from the BLS model, we perform least square analysis and fitting. Apart from three hyperparameters,

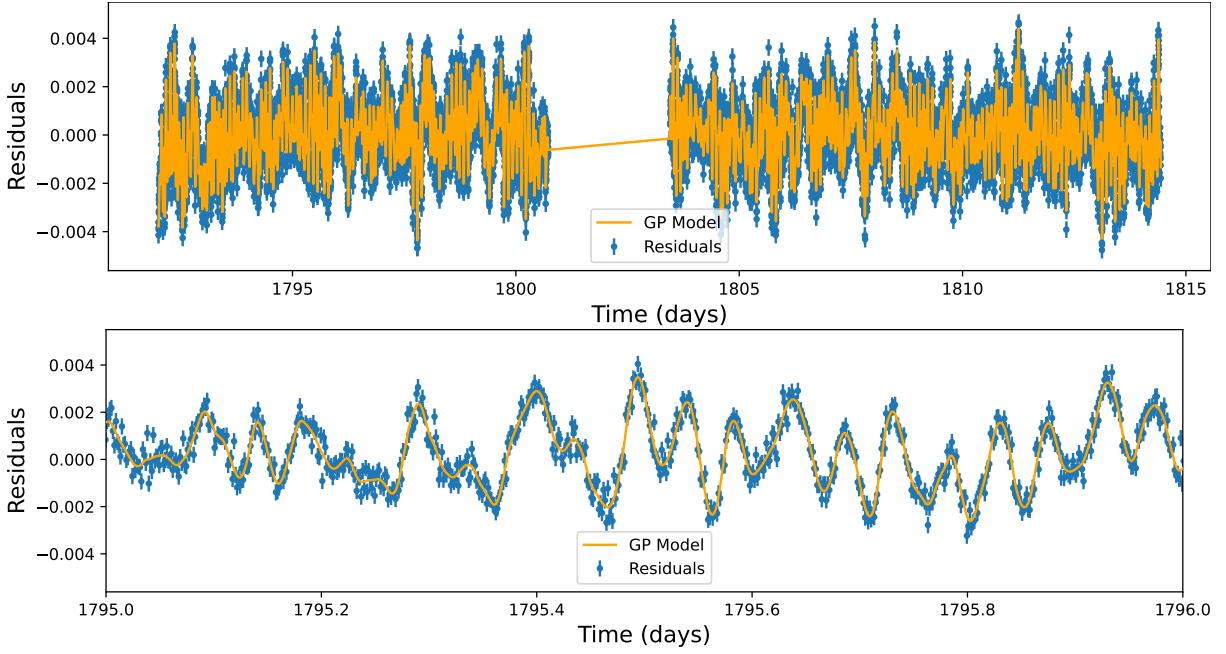


**Figure 2.6:** Best fit GP model plotted over residuals (top) shows how well it models the correlated noise in the data due to stellar variability. Figure (below) is a zoom in view of the above to show GP is not overfitting as it is not passing through each and every data point.

we also included a jitter ( $\sigma_{\text{jitter}}$ ) term. In case we don't include it, the estimated value of  $f_p$  will be biased as the errorbars will be underestimated on  $f_p$  and all other derived parameters.

In the joint modeling and fitting, the first estimates of the combined parameters are obtained from least square regression and these estimates are used as a starting point in MCMC analysis. We apply uniform prior probabilities on all (GP+BATMAN) the parameters. A total of 96 walkers and 3000 steps are used to explore the parameter space. Around step number 1000 and after we can see (see Fig. 4.2), the log-likelihood progresses from a local maxima towards a global maximum. We then detrend the original data using the best-fit GP model.

We also choose 100 random parameter sets from the posteriors around the region of maximum likelihood and use them to obtain 100 BATMAN models. In figure 2.7, we plot these models over the phase folded detrended data to see how well joint fitting constrains the light curve shape, including transit, phase variation and eclipse depth  $f_p$ . The uncertainty (see table 4.1) on  $f_p$  of about 100 ppm compared to 9 ppm from the BATMAN only model is induced by the inclusion of GP which reduces the bias of the results i.e yielding more realistic results and this can be closely compared to the dispersion of the models (orange) and binned data points.

The residuals (see Fig. 2.7) from the joint fitting do not show variability compared to that from BATMAN only model fit (see Fig. 2.5). This shows the effect of most of

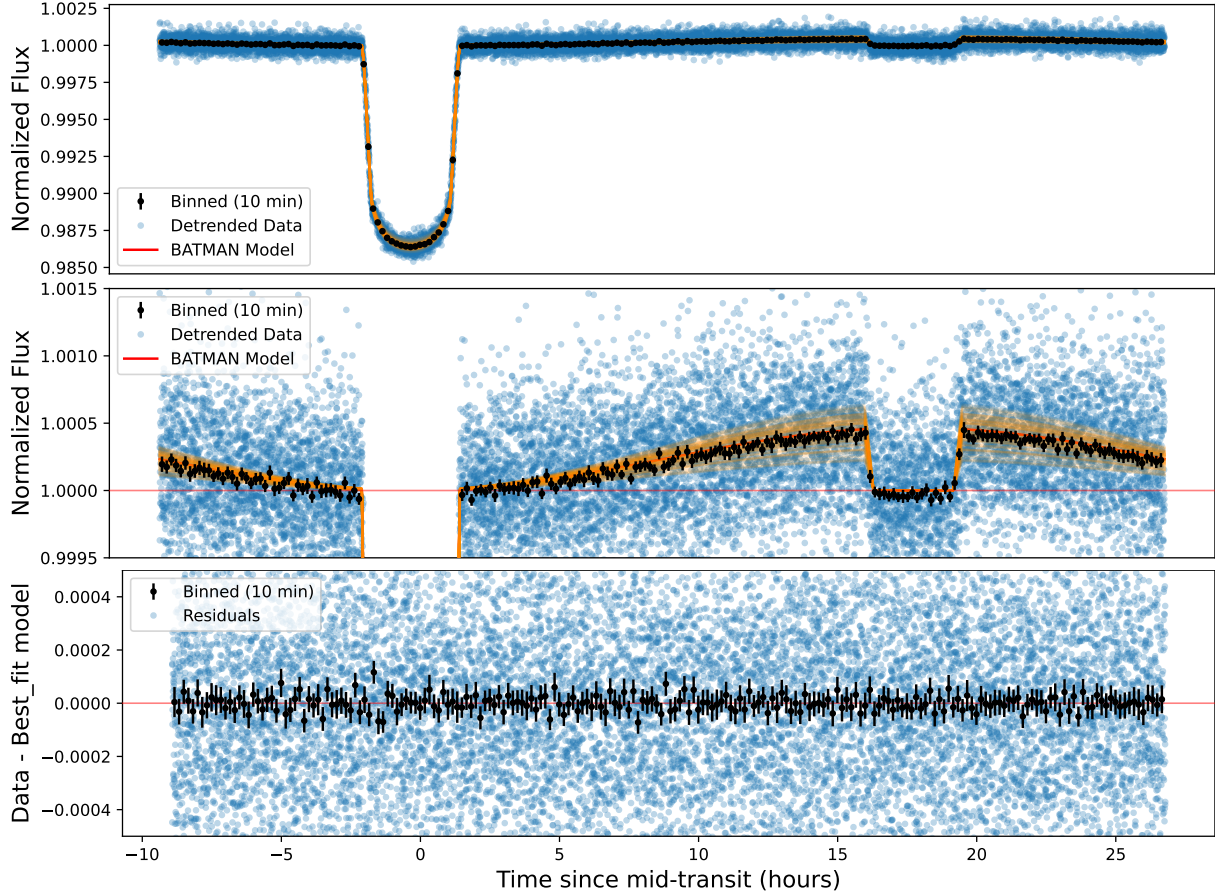


**Figure 2.7:** In the figure(upper panel) is the detrended (WASP-33 b) data in blue, with binned data in black and overplotted are 100 BATMAN models generated from 100 randomly chosen samples of parameters from the posterior around maximum likelihood. Same (middle panel) but a zoom-in view to see eclipse better and to see how well the mean model (red) fits the eclipse and the phase curve. Residuals (bottom panel) shown are computed from the best fit (GP+BATMAN) model. In comparison to BATMAN only fit (see Fig. 2.5) there are no wiggles or variability around zero line(red) which points to good detrending of the data.

the correlated noise induced by the host star is successfully modelled using GP. Essen et al. 2021 modelled these frequencies individually to get an eclipse depth of  $305.8 \pm 35.5$  ppm. Eclipse depth  $f_p$  calculated in this work is well within  $1.5\sigma$  of the value from Essen et al. 2021 but the latter results are 2 times as precise as ours and are certainly better. This difference in the precision of results despite using data from the same sector can be attributed to different pathways of analysing the data as discussed in subsection 2.3.1. From the corner (Daniel Foreman-Mackey 2016 [18]) plot (see Fig. 4.1) we can see some strong correlations between  $t_0$  and period as expected, anti-correlation between scaling parameters  $f$  &  $f_p$ ,  $s$  &  $f$ , and a positive correlation between amplitude ( $\sigma_{gp}$ ) and period ( $P_{gp}$ ) of the kernel. Most importantly, we don't see a very strong correlation of  $f_p$  with any of the parameters, which shows it is quite well constrained. Some of these correlations are due to inherent dependency between parameters. For example, an anti-correlation between epoch time  $t_0$  and period  $P$ .

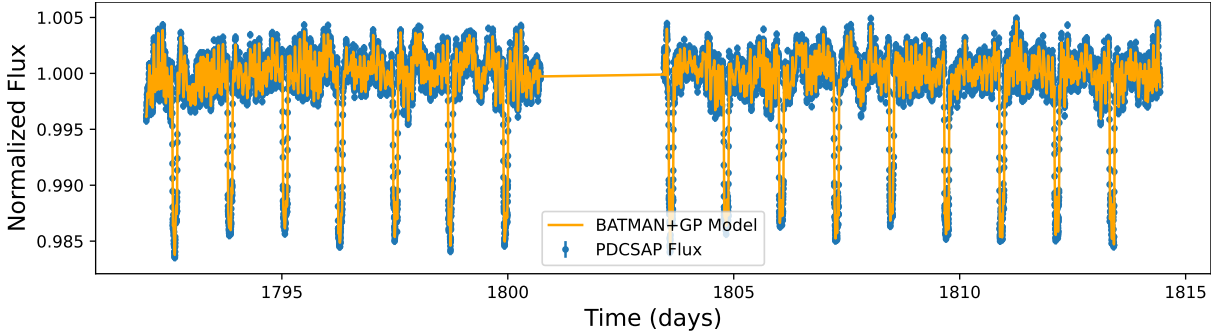


**Figure 2.8:** Best fit full model (GP+BATMAN) plotted over original WASP-33b data 2.1

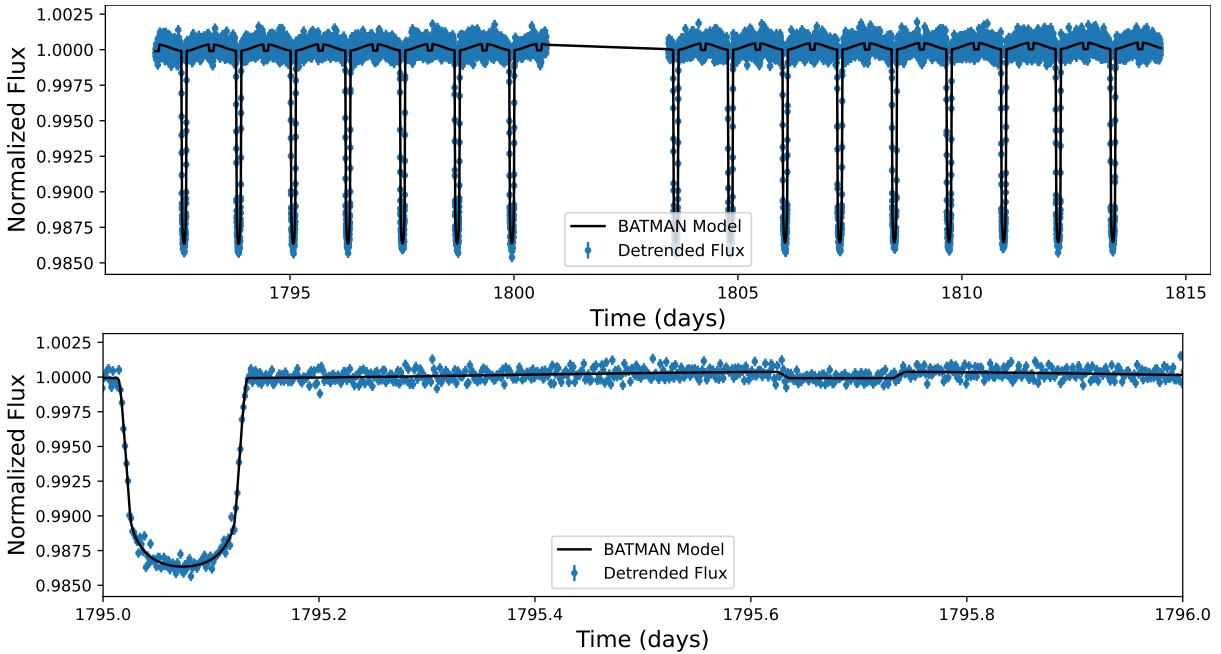


**Figure 2.9:** Figure (top) showing Best fit BATMAN model (top) plotted over corrected data from GP model and below is a zoom-in over a single transit and eclipse.

### 2.4.3 GP Prediction

In the previous section, we saw how well a GP can fit for the correlated noise in the data. We also use GP to predict the data in the gaps. The prediction mostly depends upon the size of the gap and the GP parameter  $\rho$  i.e correlation length of the kernel. For a good prediction, the size of the gap must be comparable to the correlation length of the kernel. We try to predict for the big gap between orbit 1 and 2 of the WASP-33b data (see Fig. 2.1) and the GP prediction comes out to be as expected. (see Fig. 2.10).

Since the size of the gap is more than 3.5 days and the correlation length from the joint fit is about 0.062 days, which is smaller by a factor of 50. Therefore, we get a flat prediction region with large uncertainties. If we look carefully at the ends in zoom-in plot (see Fig. 2.10), we see it's not flat and instead there are some levels of prediction at the edges. This is due to the fact that nearby both ends, there are some data points that the GP uses to compute correlations.

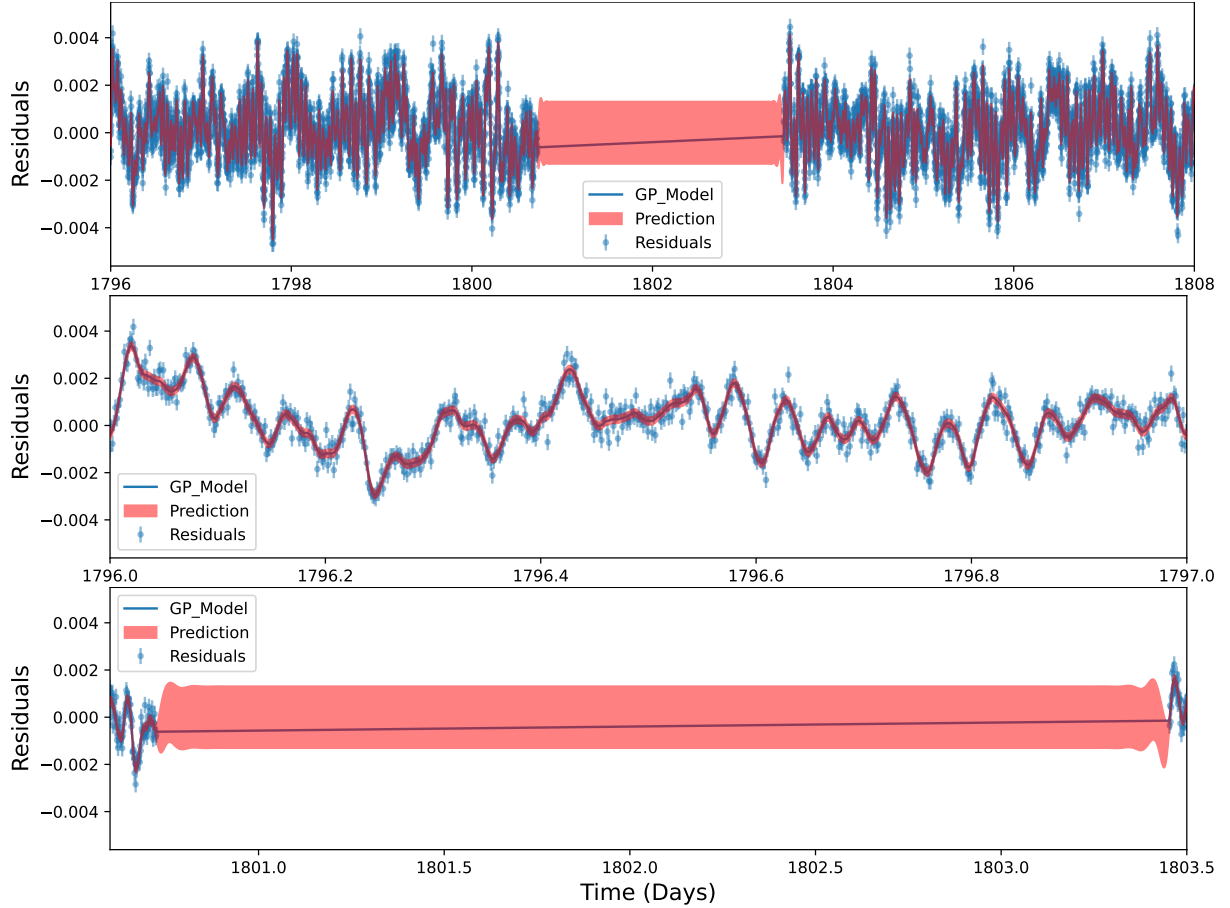


**Figure 2.10:** In the figure(upper panel) GP prediction of data and the gap, plotted over residuals. This plot (Middle) is zoom-in over the region where GP predicts data well along with  $1\sigma$  uncertainty region. Plot (Bottom) is showing prediction for gap, here  $1\sigma$  uncertainty region is broad as GP does not predict well.

A prediction could be crucial in cases where we have some in-transit data missing due to an issue onboard TESS or some technical issue in the data recovery. The prediction where the kernel finds data points is quite good ( see upper panel Fig. 2.10). We can see how well the model passes through data points along with  $1\sigma$  uncertainty region around it (middle panel). We can also see that the width of the uncertainty region increases wherever there is a large scattering in the data points around the mean model.



# Chapter 3

## Secondary Eclipses from Hot Jupiters

TESS and CHEOPS (Characterizing Exoplanet Satellite) are currently leading the way in photometric detection and characterization of exoplanets from space after the Kepler space telescope retired in late 2018. CHEOPS on one hand perform high precision photometry of individual targets, while TESS performs a sky survey and observes a large number of stars. These two telescopes make a perfect team as both share a significant portion of their observation bandpass between about 600-1200 nm. (see Fig. 3.1)

Since the launch of TESS in 2018, more than a year before CHEOPS, a recent report (Ivshina et al. 2022) mentions 382 confirmed TESS planets and among them, 240 are hot Jupiters ( $\text{mass} > 0.3 \text{ M}_{\text{Jup}}$  and  $\text{period} < 10 \text{ days}$ ). TESS has delivered over 5000 planet candidates by April 2022 and this will hopefully turn the three-digit hot Jupiters figure into a four-digit number. CHEOPS being a follow-up mission has limitations to observe these many targets. So, it's important to have a sorted list of important (based on criteria discussed in chapter 3) hot Jupiters for follow-up observations.

Better constraints on the physical parameters of these planets using high precision photometry with CHEOPS would give an improved global picture of their physical properties. A very few interesting CHEOPS targets may become a part of JWST(James Web Space Telescope) observations. Transmission and reflection spectroscopy of those exoplanets will give a deep insight into their atmosphere(composition, escape etc.), temperature profile, pressures profile, winds and clouds.

In chapter 2, we analyzed the data of WASP-33b and found eclipse depth of  $f_p = 466 \pm 105.5 \text{ ppm}$  which is within  $1.5\sigma$  of values from previous work Essen et al. [54] & [53]. The methodology applied for analysing this target is employed for 29 other hot Jupiters. For WASP-33b, data from only one sector is available. We use PDCSAP(Pre-search Data Conditioning SAP flux) flux which is already detrended from systematic noise using TESS SPOC (Science Processing Operations Center) pipeline developed by NASA.

For the rest of the targets, apart from analysing PDCSAP flux, we also use SAP (Simple Aperture Photometry) i.e raw flux wherever we find in our initial analysis that the PDCSAP flux is not detrended properly by the pipeline. Data from multiple sectors is used to get better constraints on the parameters along with their uncertainties, provided it is available. When we also used SAP data, we first detrend it using a GP to remove major trends and then execute the joint analysis of BATMAN and GP model. We discuss in detail on detrending of SAP data when we show a complete analysis of KELT-20 b in subsection 3.2.1. Given the constraints of time, we do not perform our own aperture photometry to extract time-series data from Full Frame Images (FFI) files which could have been better in some of the cases such as binary star systems where both stars are blended.

## 3.1 Target selection

One of the main goals of this thesis work is to find hot Jupiters that show robust eclipse depth for high precision follow-up observation from CHEOPS. So, we apply certain filters to make our target list where planets fulfill both the definition of a hot Jupiter and lie in the observational regime of CHEOPS. The data are taken from ExoFOP<sup>1</sup> after applying filters. The first filter selects planets that lie in the CHEOPS Field of View (FOV). Another filter selects hot Jupiters and thus planets with radius  $> 0.5 R_{\text{Jupiter}}$ , orbital period  $< 10$  days, equilibrium temperature of the planet  $> 1500$  K and that of star  $< 5000$  K. Further, host star brighter than  $< 10$  TESS magnitude and data with Signal to Noise Ratio (SNR) of at least 100 are selected. After applying all these filters, we get a list of 42 targets. Figure 3.1 shows all these targets along with their host star position in the sky. Out of these, we further remove some based on the comments and some after analysis with BATMAN only model, which shows the target is a grazing eclipsing binary. Finally, we get a total of 29 targets for the analysis.

## 3.2 Data Acquisition and Analysis

Time-series data for all 29 targets are filtered from a list of 42 extracted targets from MAST<sup>2</sup> in the form of FITS files. We have already discussed the analysis of WASP-33 b in Chapter 2, so, here we apply the same methodology for the rest of the targets. Since we did not show there how to perform analysis with SAP flux, let's take one of our first planet candidates for which we detect secondary eclipse and see the detrending part along with the rest of the analysis.

---

<sup>1</sup>ExoFOP

<sup>2</sup>MAST: Barbara A. Mikulski Archive for Space Telescopes

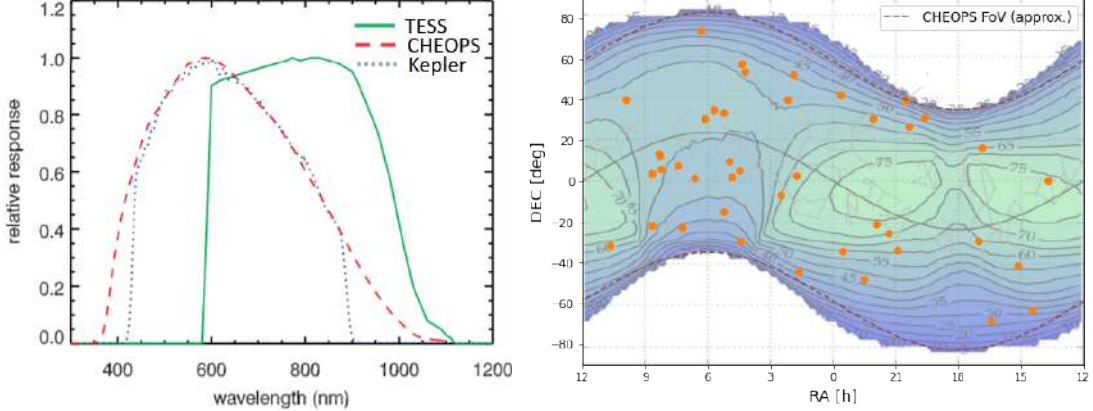


**Figure 3.1:** Figure(left) showing bandpass of different space telescope with wavelength coverage of their observation. Figure adapted from (Gaidos et al.), 2017. Figure(right) showing 42 targets with their sky coordinates plotted after applying major filters. The dash line shown is CHEOPS Field of View (FOV) boundary and it was approximated using a sine function.

### 3.2.1 TIC 69679391 (KELT-20 b/MASCARA-2 b/HD 185603)

KELT-20 b is an ultra-hot Jupiter that orbits a ( $m_V = 7.6$ ) A2-type star with an effective temperature of 8980 K[50] in about 3.47 days. This planet was discovered by Lund et al. 2017 [30]. All transit ephemeris from our joint sector analysis are well within  $1\sigma$  of values from the discovery paper. Secondary eclipse observations for this target have not been reported so far. We first analyze data from all three TESS sectors(14,40,41) individually with SAP flux. When analyzing the PDCSAP data, we obtain large negative values of  $f_p$ , largely inconsistent with zero. After analyzing each sector individually, we remove data points from the original data that correspond to  $5\sigma$  outliers in residuals obtained with the best fit joint (BATMAN+GP) model. We then perform a joint sector analysis of sectors 14 and 40 which gives a statistically significant detection of secondary eclipse depth of  $f_p = 65 \pm 17$  ppm. In the analysis, we use Matérn-3/2 kernel (see equation 2.8 ) and quadratically add a jitter term to the variance of the data to account for underestimated errorbars due to extra white noise. We also perform a joint analysis of sector 40 and 41 data, this time with SHO Kernel which gives an eclipse depth of  $f_p = 62 \pm 14$  ppm and is well within  $0.5\sigma$  of the previous value. We finally present results for this target from sectors 14 and 40 as one of the parameters, epoch time ( $T_0$ ) has almost a flat posterior distribution in sectors 40 and 41 analysis. In another joint analysis of these two sectors with Matérn-3/2 kernel, MCMC does not converge. For the final analysis of sectors 14 and 40, we use 128 walkers with 3000 MCMC steps.

The SAP flux is detrended with a GP model. Sequentially, for each sector data, first, we remove all in-transit data using epoch time  $T_0$  and period  $P$  obtained from individual sector analysis, and  $T_{14}$  total transit time taken from Lund et al. 2017 [30]. Then, we remove major outliers and model out-of transit data using a GP using Matérn-3/2 kernel. In the GP model, we choose the initial value of the correlation length  $\rho$  based on long-term trends that are seen in the data and we keep  $\rho$  significantly larger than the

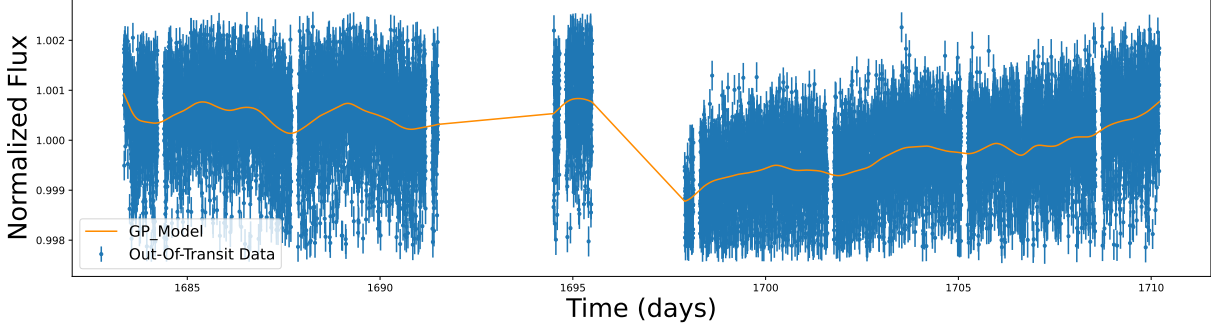


**Figure 3.2:** Figure showing fitted GP model (orange) plotted over out-of transit data of KELT-20 b (sector 14) after removing all parametric in-transit (narrow gaps) data points.

transit duration of the planet so as that the GP does not detrend away the transit, phase curve and eclipse signal. The fitting is performed using least square regression(see eq. 2.2) and after obtaining the adjusted GP model, (see Fig. 3.2) we predict it over the full time-series of SAP data using adjusted hyperparameters. we subtract this model from the SAP data to detrend it and normalize flux values by adding 1 to the detrended flux. We follow a similar procedure for the rest of the sectors to finally proceed with the joint sector analysis using (BATMAN+GP) model.

Besides fitting for the occultation depth, we derive the equilibrium temperature of the planet  $T_{eq}$  using equation 1.17 for a limiting case, assuming heat redistribution factor of  $f = 1$  i.e full atmosphere circulation and bond albedo of  $A_B = 0$ . This gives  $T_{eq} = 2332 \pm 6K$  which is within  $1\sigma$  of  $T_{eq} = 2261 \pm 73K$  as reported by Lund et al. 2017[30]. We further estimate the expected thermal flux contribution (see eq.1.15) in the observed occultation depth by assuming  $T_p = T_{eq}$  of the planet and treating planet and the host star a blackbody. Using 2<sup>nd</sup> part of the same equation 1.15 and integrating their fluxes over the transmission function of TESS (see Fig. 3.1) gives an occultation depth of  $f_{p,th} = 30$  ppm. The same computation for  $f = 2$ , i.e no heat redistribution in the atmosphere, gives  $T_{eq} = 2774 \pm 7K$  which translates to  $f_{p,th} = 102$  ppm.

Further, the expected contribution from the reflected flux  $f_{p,rf}$  is computed by taking the difference of observed eclipse depth  $f_p$  and the expected thermal flux  $f_{p,th}$  as calculated above. Finally, We get an eclipse depth of  $f_{p,rf} = 32$  ppm. Using this value, We place a theoretical upper limit on geometric albedo  $A_{g,th}$  and we find  $A_{g,th} < 0.147$ . The observed eclipse depth  $f_p$  gives brightness temperature  $T_b = 2192 \pm 70K$  at 0.722 micron and it is less than  $T_{eq} = 2332 \pm 6K$ . We choose 0.722 micron since it is the wavelength in the TESS bandpass where the transmission function of TESS is maximum. We use this wavelength for calculating  $T_b$  for the rest of the eight targets. We assume an efficient heat distribution in the atmosphere  $f = 1$  in calculating  $T_b$  using equation 1.18. A possible explanation for a lower value of  $T_b$  could be the underestimation of  $f_p$  due to improper detrending of either of the sectors (14, 40). We also calculate the expected secondary eclipse depth of 37.78 ppm in the CHEOPS bandpass assuming  $f = 2$ .

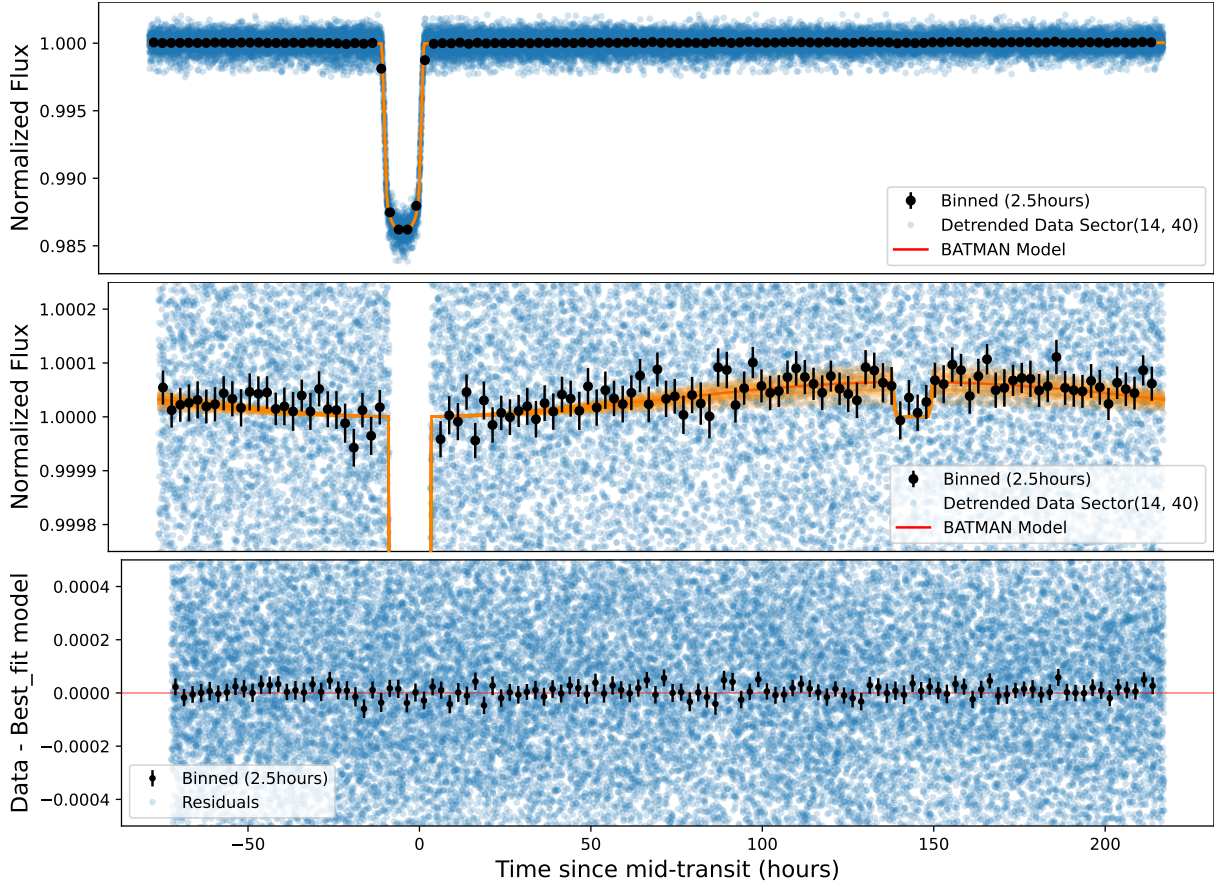


**Figure 3.3:** Figure (top) showing 100 BATMAN models plotted over detrended data of KELT-20 b (sector 14 & 40). (Middle) Zoom-in view of the above and residuals (bottom) obtained with best fit GP+BATMAN model.

**Table 3.1:** KELT-20 b: Derived parameters based on secondary eclipse analysis.

$f_p(ppm)$	$f_{p,th}(ppm)$	$f_{p,rf}(ppm)$	$T_{eq}(K)$	$T_b(K)$	$A_{g,th}$
$62 \pm 14$	102	32	$2332 \pm 6$	$2192 \pm 70$	$< 0.147$

### 3.2.2 TIC 290131778 (TOI-123 A b/HD 202772 A b)

HD 202772 A b or TOI-123 is a hot Jupiter that orbits a ( $m_V = 8.32$ ) F-type star with an effective temperature of 6230 K [55] in about 3.3 days in a binary star system. This planet was discovered from sector 1 data of TESS by Wang et al. 2019 [55]. No secondary eclipse observations have been reported so far. We took data from both sectors 1 and 28 and an initial analysis using a simple BATMAN model indicates the data for both sectors is detrended well by the TESS SPOC pipeline. Therefore, we continue our joint model (BATMAN+GP) analysis with PDCSAP flux, which gives a statistically significant detection of  $f_p = 59 \pm 18$  ppm. We use a Matérn-3/2 kernel for the GP and for fitting, 128 walkers with 3000 MCMC steps.

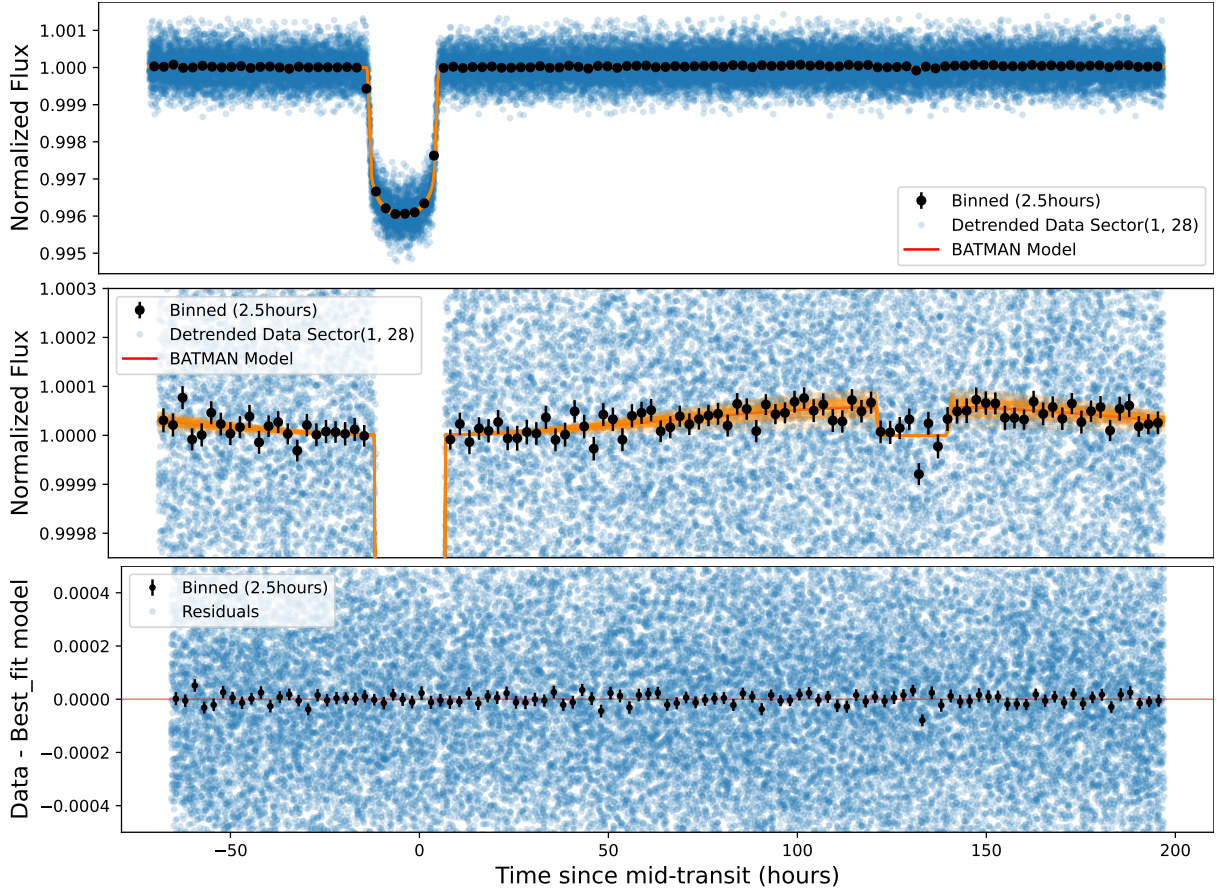


**Figure 3.4:** Figure(top) showing 100 BATMAN models plotted over detrended data of TOI-123 b (sector 1 & 28). (Middle) Zoom-in view of the above and residuals (bottom) obtained with best fit GP+BATMAN model.

Being a binary system, the contribution of flux from the companion star does affect the transit depth and is corrected by a dilution factor as implemented by Wang et al. 2019 [55]. Since we are concerned mainly with eclipse, the presence of a companion may not affect the relative eclipse depth  $f_p$  because the same contribution is present both in the total stellar flux and flux emitted by the planet as it goes behind the star. Moreover, this dilution factor is required when we use SAP flux. For this target, since we use PDCSAP flux which is already corrected for dilution. However, it should be corrected when using SAP flux as stated above, otherwise, it will affect all the other computed parameters based on  $f_p$  as we use only primary stellar parameters to derive the results. Moreover, relative eclipse depth only due to the primary star around which the planet orbits, will be lower than the one from the blended case.

Following a similar strategy to that of the KELT-20 b analysis, we derive the equilibrium temperature of the planet assuming full atmosphere circulation  $f = 1$  and  $A_B = 0$ , and we get  $T_{eq} = 2170 \pm 19K$  which is within  $1\sigma$  of values compared to  $T_{eq} = 2132 \pm 35K$ , as reported by Wang et al. 2019 [55]. He also uses the same assumption of zero albedo and full heat redistribution from day to night hemispheres. We get an expected occultation depth of  $f_{p,th} = 50$  ppm from thermal flux.

Similarly, expected contribution from reflected part is calculated using observed eclipse depth  $f_p$  and expected thermal contribution  $f_{p,th}$  which gives an eclipse depth of  $f_{p,rf} = 9$  ppm. Using this value, we place a theoretical upper limit on geometric albedo  $A_g < 0.212$ . We further derive brightness temperature  $T_b = 2227 \pm 84K$  at 0.722 micron using observed eclipse depth  $f_p$  and as expected  $T_b$  is greater than  $T_{eq} = 2170 \pm 19$ . Here, we assume an efficient heat distribution in the atmosphere  $f = 1$  in calculating  $T_b$  and other parameters. Finally, We also calculate the expected secondary eclipse depth of 22.5 ppm in the CHEOPS bandpass assuming  $f = 2$ .

**Table 3.2:** HD 202772 A b: Derived parameters based on secondary eclipse analysis.

$f_p$ (ppm)	$f_{p,th}$ (ppm)	$f_{p,rf}$ (ppm)	$T_{eq}$ (K)	$T_b$ (K)	$A_{g,th}$
$59 \pm 18$	50	9	$2170 \pm 19$	$2227 \pm 84$	$< 0.212$

### 3.2.3 TIC 367366318 (KELT-7 b)

KELT-7 b is a hot Jupiter that orbits a ( $m_V = 8.54$ ) rapidly rotating F-type star with an effective temperature of 6789 K [4] in about 2.73 days and was discovered by Bieryla et al. 2015 [4]. No secondary eclipse observations have been reported so far using the TESS data. In near-infrared, using WIRCam at CFHT, Martioli et al. 2017 [34] reported an eclipse depth of 400 ppm at  $\lambda \approx 2.2\mu m$ . We use data from two sectors (42 & 43) and perform joint model (BATMAN+GP) analysis of the PDCSAP flux that gives  $> 5\sigma$  detection with  $f_p = 93 \pm 18$  ppm. For this target, we find that an SHO kernel is best to employ due to strong correlated noise in the data. From the periodogram and also from visual inspection, we see this as periodic wiggles in the data and we set the period of the GP kernel to 1 day, similar to the maximum stellar rotation period for KELT-7 of  $1.08 \pm 0.03$  days reported by Zhou et al. 2016 [62]. For the joint model fitting, we use 144 walkers with 3000 MCMC steps.

Further, the equilibrium temperature of the planet assuming complete heat redistribution  $f = 1$  and  $A_B = 0$  is  $T_{eq} = 2044 \pm 7K$  which is well within  $0.2\sigma$  of  $T_{eq} = 2048 \pm 27K$  as reported by Bieryla et al. 2015 [4]. Also, assuming a full heat redistribution case and with  $A_B = 0.1$ , we get  $T_{eq} = 1991 \pm 7K$  which is nearly consistent as shown in Figure 11 of Martioli et al. 2017 [34] where he uses the same assumptions on  $f$  and  $A_B$ . Further, expected thermal contribution in occultation depth is  $f_{p,th} = 55.2$  ppm assuming no heat redistribution i.e  $f = 2$  and that from reflected part computed using  $f_p$  and  $f_{p,th}$  is  $f_{p,rf} = 38$  ppm. Using this eclipse depth, we get an upper limit on  $A_g < 0.3$ .

The observed eclipse depth  $f_p$  gives a brightness temperature  $T_b = 2210 \pm 53K$  at 0.722 microns in the TESS bandpass and is well above  $T_{eq} = 2044 \pm 7K$  which assumes full heat redistribution. It is significantly larger than  $T_{eq}$  for  $f = 1$  and  $A_B = 0$ , which indicates a considerable but not strong temperature difference between the day and night

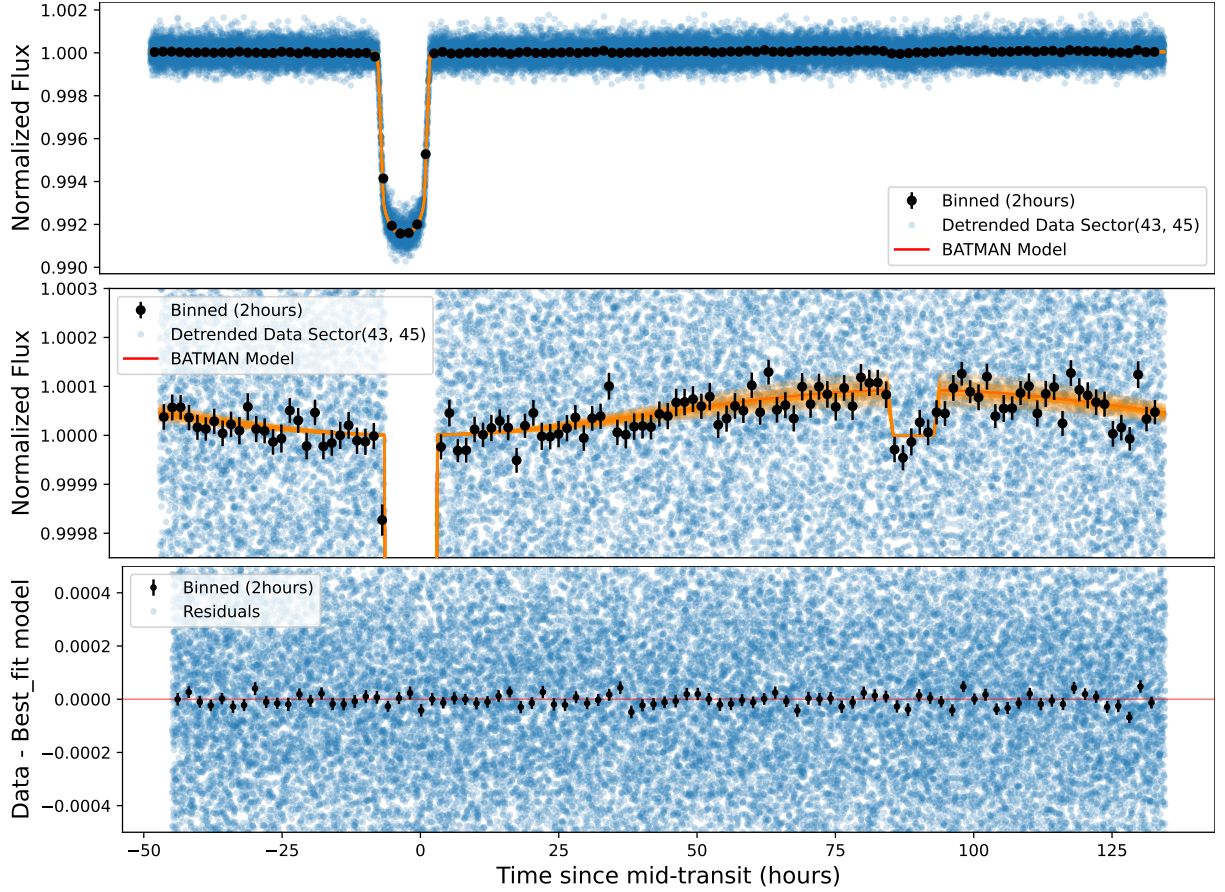


**Figure 3.5:** Figure (top) showing 100 BATMAN models plotted over detrended data of KELT-7 b (sector 43 & 45). (Middle) Zoom-in view of the above and residuals (bottom) obtained with best fit GP+BATMAN model.

side compared to hot Jupiters having  $T_{eq} > 2000K$ . Pluriel et al. 2020 [40] report the transmission spectrum is consistent with a cloud-free atmosphere and also suggest the presence of  $H_2O$  and  $H^-$  along with. The presence of  $H^-$  indicates dissociation and recombination of  $H_2$  which enhances energy redistribution in hot Jupiters between both hemispheres. In the absence of winds, the day side temperature relatively gets lower because some of the stellar radiation is used in the dissociation process and on the night side, re-combination relatively increases the temperature and this whole process lowers the temperature gradient between both hemispheres. Lastly, We also calculate the expected secondary eclipse depth of 22 ppm in the CHEOPS bandpass.

**Table 3.3:** KELT-7 b: Derived parameters based on secondary eclipse analysis.

$f_p(ppm)$	$f_{p,th}(ppm)$	$f_{p,rf}(ppm)$	$T_{eq}(K)$	$T_b(K)$	$A_{g,th}$
$93 \pm 18$	55.2	38	$2044 \pm 7$	$2210 \pm 53$	< 0.3

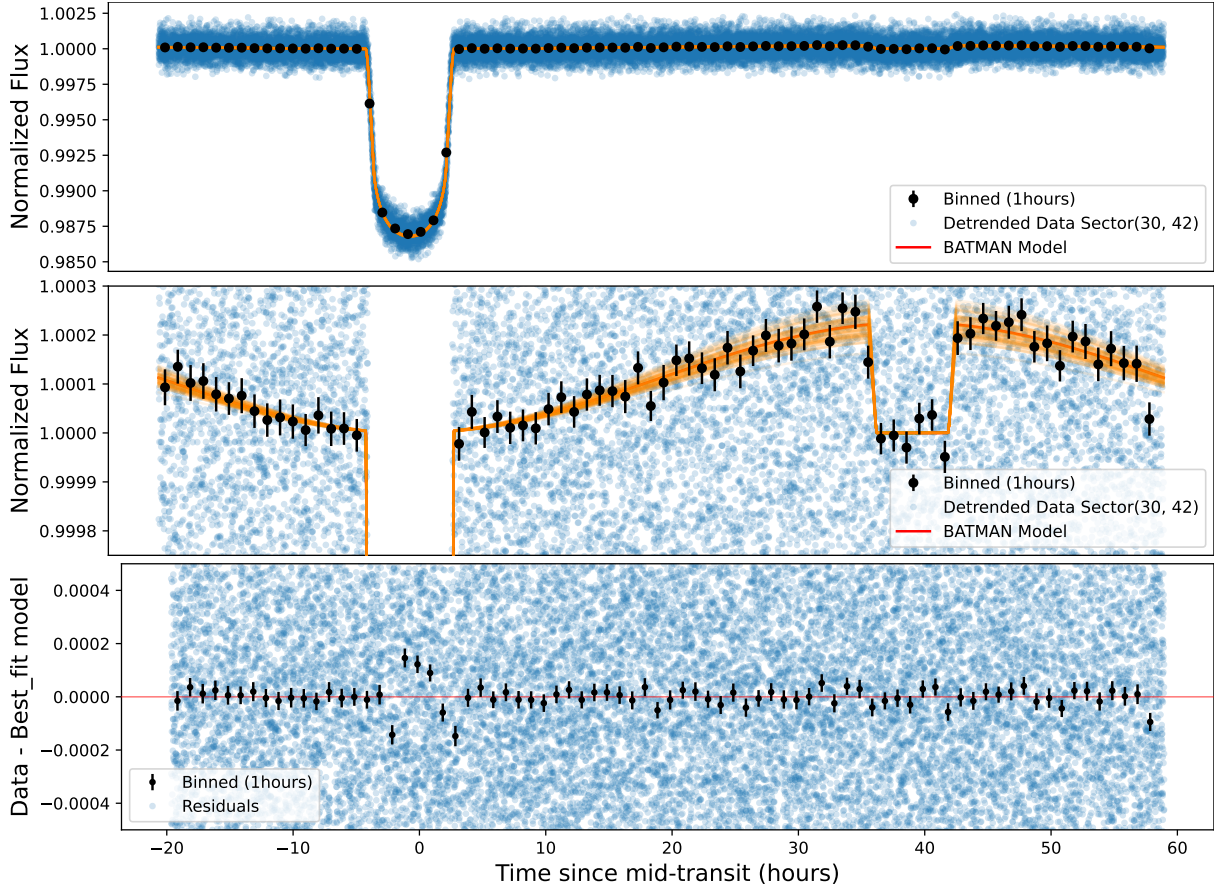


**Figure 3.6:** Figure (top) showing 100 BATMAN models plotted over detrended data of WASP-76 b (sector 30 & 42). (Middle) Zoom-in view of the above and residuals (bottom) obtained with best fit GP+BATMAN model. A larger dispersion (see binned data points in black) in residuals during in-transit is present because we don't model for gravity darkening effect.

### 3.2.4 TIC 293435336 (WASP-76 b)

WASP-76 b is an inflated ultra-hot Jupiter that orbits a ( $m_V = 9.5$ ) F7 star with an effective temperature of 6250 K [56] in about 1.81 days and was discovered by West et al. in 2016 [56]. No secondary eclipse observations have been reported so far from its TESS observation. However in the infrared, with Spritzer data, (May & Komacek, et al. 2021 [36]) showed an eclipse depth of 2539 ppm at  $3.6\mu m$  and 3729 ppm at  $4.5\mu m$ . We analyzed all three sectors 30,42 and 43 with both SAP and PDCSAP data and for the final analysis, we use PDCSAP data from sectors 30 & 42. A joint model (BATMAN+GP) analysis of the PDCSAP flux gives  $> 10\sigma$  detection with  $f_p = 226 \pm 22$  ppm. We do not use sector 43 as data from this sector is not good compared to the other two sectors. Even after detrending SAP data, two parameters namely  $\rho$  and jitter term  $\sigma_{jit}$ , do not show expected posterior distribution. A possible explanation could be lower bounds on the priors, which were set to zero for both parameters. In the final analysis, we use the Matérn-3/2 kernel and for fitting, 128 walkers with 4000 MCMC steps.

The equilibrium temperature of the planet assuming heat redistribution  $f = 1$  and  $A_B = 0$  is  $T_{eq} = 2194 \pm 1K$  which is well within  $1\sigma$  of  $T_{eq} = 2160 \pm 40K$  as reported

in the discovery paper. The expected thermal contribution to the occultation depth is  $f_{p,th} = 162$  ppm assuming no heat redistribution i.e  $f = 2$  and that from reflected part, it is calculated by subtracting thermal contribution  $f_{p,th}$  from the observed eclipsed depth  $f_p$ , which gives  $f_{p,rf} = 64$  ppm. Using this eclipse depth, we get a theoretical upper limit on  $A_g < 0.27$ . Observed eclipse depth  $f_p$  gives brightness temperature  $T_b = 2300 \pm 29$  at 0.722 micron assuming  $f = 1$  and is larger than  $T_{eq} = 2194 \pm 1K$ . Lastly, We also calculate expected secondary eclipse depth of 73 ppm in the CHEOPS bandpass.

**Table 3.4:** WASP-76 b: Derived parameters based on secondary eclipse analysis.

$f_p(\text{ppm})$	$f_{p,th}(\text{ppm})$	$f_{p,rf}(\text{ppm})$	$T_{eq}(K)$	$T_b(K)$	$A_{g,th}$
$226 \pm 22$	160	64	$2194 \pm 1$	$2300 \pm 29$	$< 0.27$

### 3.2.5 TIC 399870368 (TOI-624 b/HAT-P-70 b )

TOI-624 b is another ultra-hot Jupiter that orbits a ( $m_V = 9.5$ ) rapidly rotating A-type star with an effective temperature of 8450 K [61] in about 2.74 days and was discovered by Zhou et al. 2019 [61]. Its orbit is highly misaligned with a projected spin-orbit angle of  $\lambda = 21.2^\circ$ . The discovery paper reports a marginal detection ( $\approx 2.44\sigma$ ) of the secondary eclipse of depth  $159 \pm 65$  ppm from sector 7 of TESS data. Zhou et al. 2019 [61] extracted the photometry from FFI images. Since extracted photometry data is not available from this sector 7, so we use sector 32 data with already extracted photometry by SPOC pipeline. The joint model (BATMAN+GP) analysis of the PDCSAP flux gives a statistically significant  $> 3\sigma$  detection with  $f_p = 216 \pm 70$  ppm. This value is within  $0.6\sigma$  of the value reported by Zhou et al. 2019 [61]. For joint model fitting, we use 88 walkers with 4000 MCMC steps. We do not account for the gravity darkening effect in transit 3.7 as it does not affect the occultation depth or even the shape of the secondary eclipse.

Further, the equilibrium temperature of the planet assuming full heat redistribution  $f = 1$  and  $A_B = 0$  is  $T_{eq} = 2590 \pm 28K$  which is well within  $0.5\sigma$  of  $T_{eq} = 2562 \pm 48K$  as reported by Zhou et al. 2019 [61]. Following a similar approach from previously discussed targets, we get expected thermal contribution in occultation depth of  $f_{p,th} = 152$  ppm assuming no heat redistribution i.e  $f = 2$  and that from the reflected part computed using  $f_p$  and  $f_{p,th}$  is  $f_{p,rf} = 64$  ppm. Using this eclipse depth, we get a theoretical upper limit on  $A_g < 0.54$ .

The observed eclipse depth  $f_p$  gives a brightness temperature of  $T_b = 2663 \pm 128K$  at 0.722 micron and is larger than  $T_{eq} = 2562 \pm 48K$  which assumes full heat redistribution. The temperature difference being small could be indicative of strong winds in the atmosphere with no clouds  $T_{eq} > 2500$ . Bello-Arufe et al. 2021 [2] also suggest a similar scenario. Using high-resolution transmission spectroscopy they detect numerous atomic and molecular species, and their signals are blue-shifted by a few  $km/s$  which suggest,

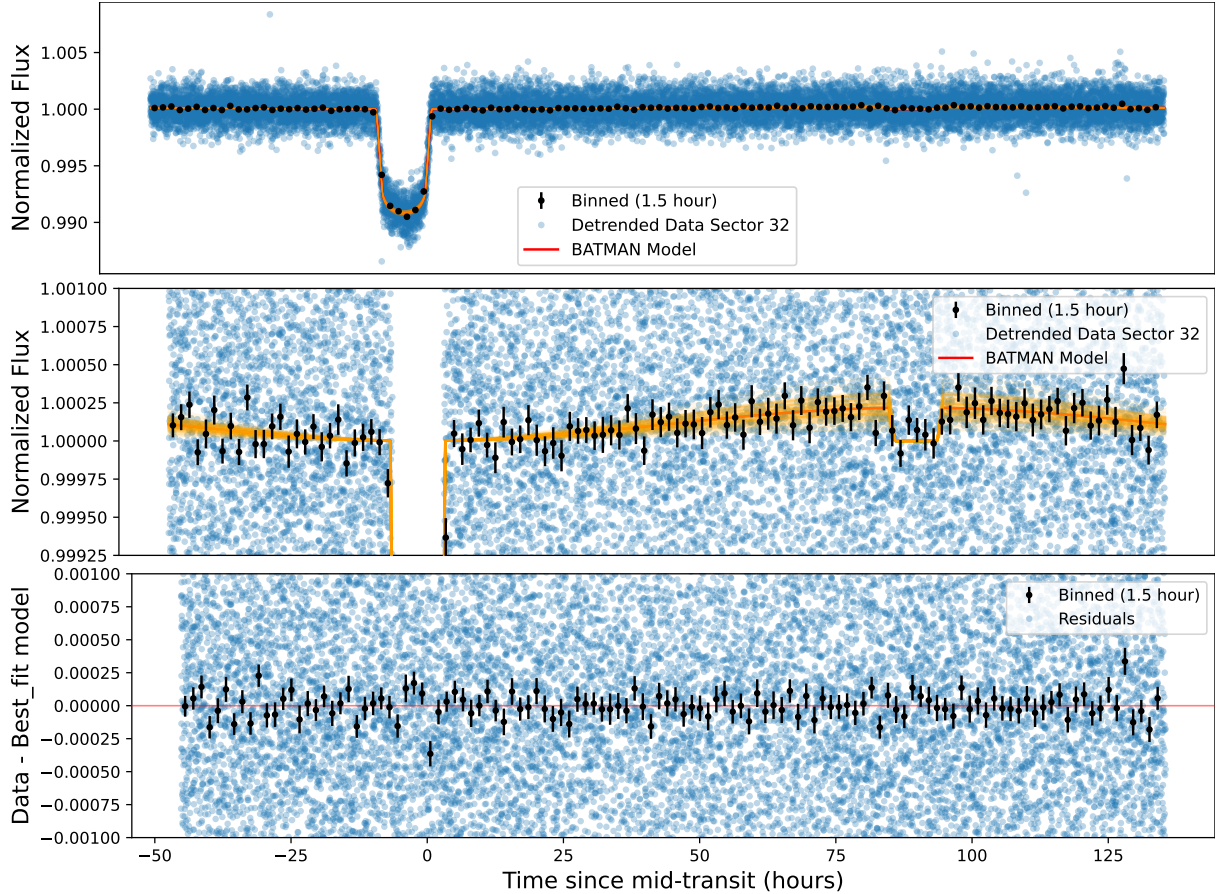


**Figure 3.7:** Figure(top) showing 100 BATMAN models plotted over detrended data of HAT-P 70 b (sector 32). (Middle) Zoom-in view of the above and residuals (bottom) obtained with best fit GP+BATMAN model.

high-velocity winds flowing from the day-side to the night-side. The high temperature inflates these hot Jupiters and inhibits cloud formation. Lastly, We also calculate expected secondary eclipse depth of 64 ppm in the CHEOPS bandpass.

**Table 3.5:** HAT-P-70 b: Derived parameters based on secondary eclipse analysis.

$f_p(\text{ppm})$	$f_{p,\text{th}}(\text{ppm})$	$f_{p,\text{rf}}(\text{ppm})$	$T_{eq}(K)$	$T_b(K)$	$A_{g,\text{th}}$
$216 \pm 70$	152	64	$2562 \pm 48$	$2663 \pm 128$	$< 0.54$

### 3.2.6 TIC 1129033/WASP-77 A b

WASP-77 A b is a hot Jupiter that orbits a ( $m_V = 11.29$ ) G-8 type star in about 1.36 days, in a binary star system with WASP-77 A, having an effective temperature of 5500 K [35]. It was discovered by Maxted et al. 2013 [35]. Wong et al. 2021 [59] report a marginal detection ( $\approx 2\sigma$ ) of the secondary eclipse of depth  $53 \pm 27$  ppm from sector 4 TESS data. However, we get eclipse depth values consistent with zero  $33 \pm 30$  ppm when using the SAP flux.

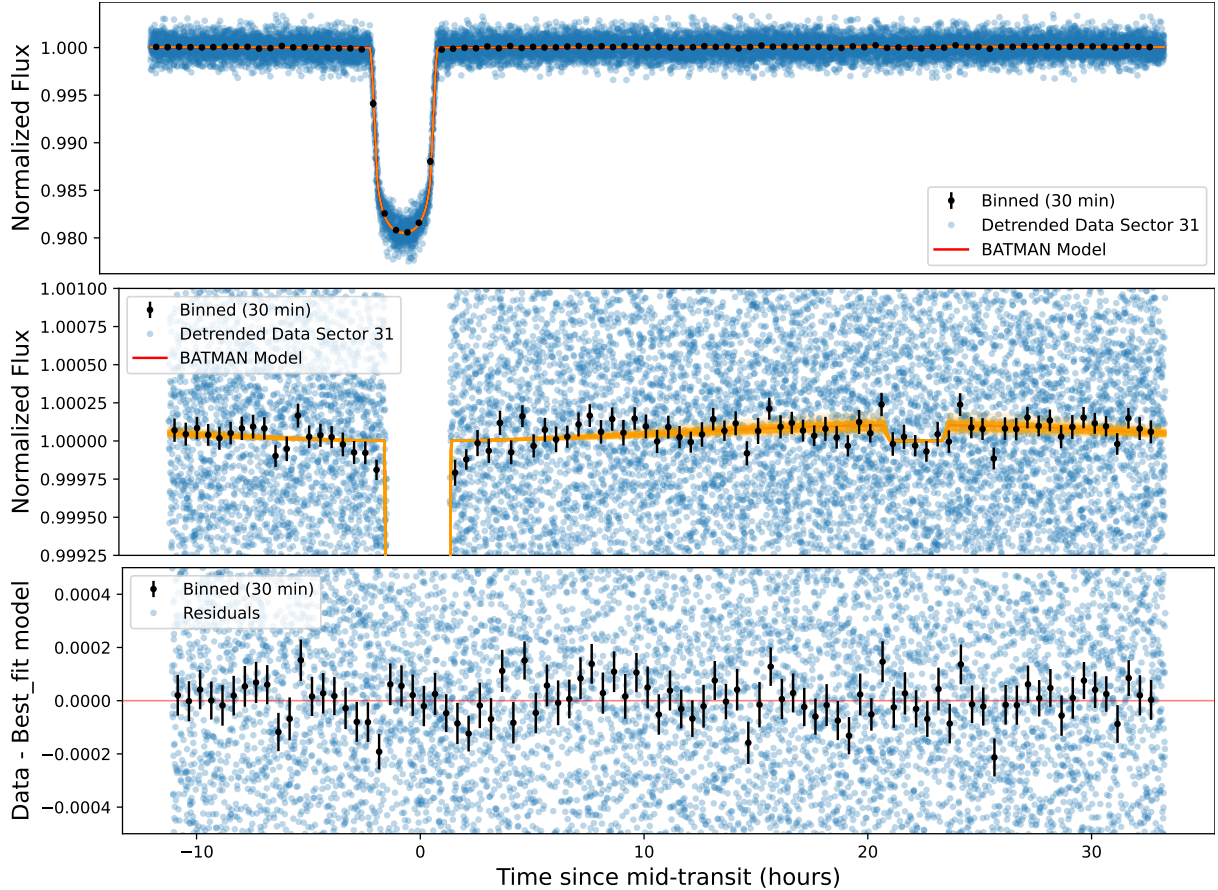


**Figure 3.8:** Figure (top) showing 100 BATMAN models plotted over detrended data of WASP-77 A b (sector 31). Dilution factor was used in the SAP flux analysis to correct from flux contamination by the secondary star. (Middle) Zoom-in view of the above and residuals (bottom) obtained with best fit GP+BATMAN model.

From sector 31, using SAP flux, we get significant detection  $> 3.7\sigma$  with  $f_p = 104 \pm 28$  ppm. We correct for the contamination due to companion star in the system using a dilution correction factor. In a joint analysis of both sectors, the MCMC does not converge (see Fig. 4.4), and similar to the case of WASP-111b 3.2.7, the MCMC walkers find numerous local solutions apart from a dense region at the median value of each posterior as seen from the corner plot 4.4 in the appendix. So, we proceed for further analysis using results from sector 31 only. For the GP, we use a Matérn-3/2 kernel and for fitting, we use 88 walkers with 3000 MCMC steps.

Further, the equilibrium temperature of the planet assuming full heat redistribution  $f = 1$  and  $A_B = 0$  gives  $T_{eq} = 1678 \pm 5K$  compared to  $T_{eq} = 1705K$  as mentioned in Mansfield et al. 2022 [33] where the author cites this parameters as reported by Maxted et al. 2013 [35]. The expected thermal contribution to the occultation depth is  $f_{p,th} = 49$  ppm, assuming no heat redistribution i.e  $f = 2$  and that from reflected part computed using  $f_p$  and  $f_{p,th}$  is  $f_{p,rf} = 55$  ppm. Using this eclipse depth, we get a theoretical upper limit on  $A_g < 0.16$ . Observed eclipse depth  $f_p$  gives brightness temperature  $T_b = 2000 \pm 57K$  at 0.722 micron and is greater than  $T_{eq} = 1678 \pm 5K$  which

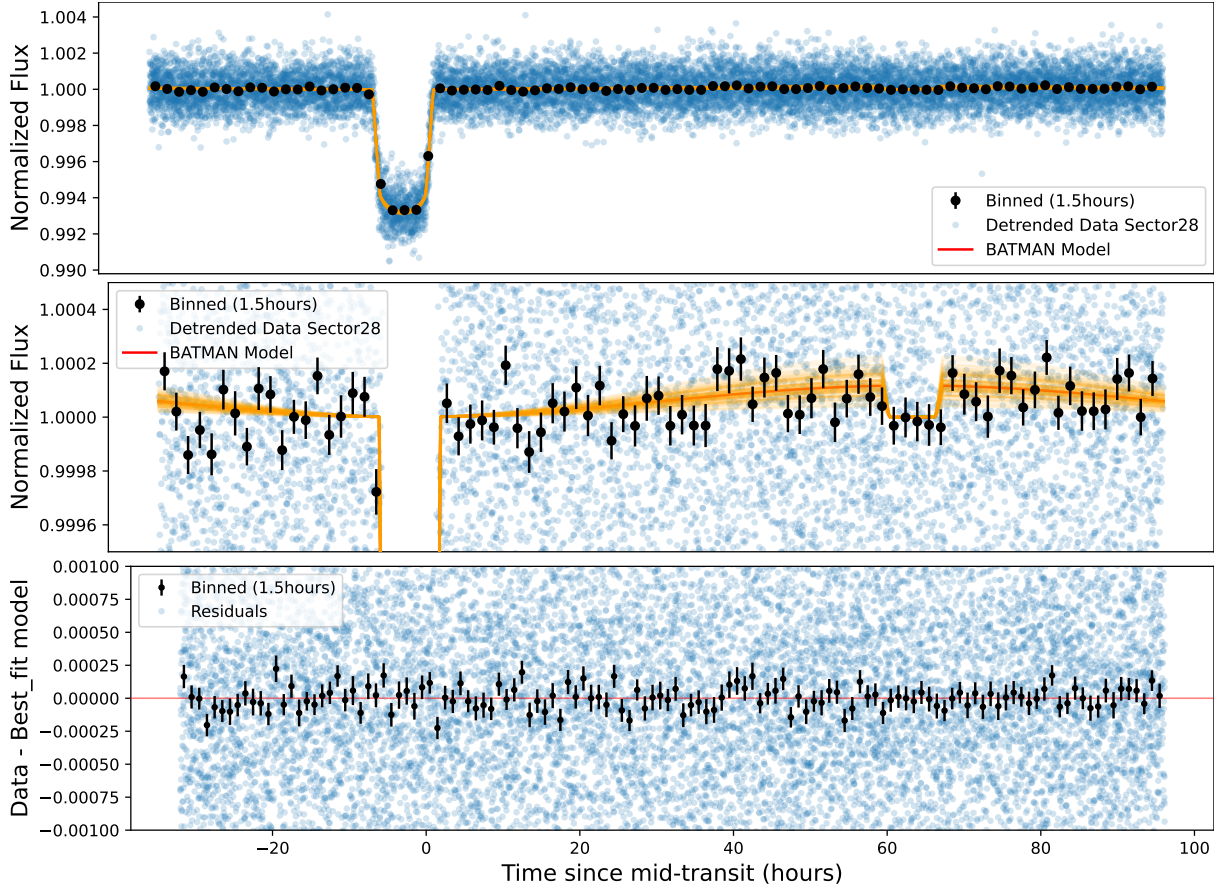


**Figure 3.9:** Figure (top) showing 100 BATMAN models plotted over detrended data of WASP-111 b (sector 28). (Middle) Zoom-in view of the above and residuals (bottom) obtained with best fit GP+BATMAN model.

assumes full heat redistribution. Lastly, We also calculate expected secondary eclipse depth of 20 ppm in the CHEOPS bandpass.

**Table 3.6:** WASP-77 A b: Derived parameters based on secondary eclipse analysis.

$f_p(\text{ppm})$	$f_{p,\text{th}}(\text{ppm})$	$f_{p,\text{rf}}(\text{ppm})$	$T_{eq}(K)$	$T_b(K)$	$A_{g,\text{th}}$
$104 \pm 25$	49	55	$1678 \pm 5$	$2000 \pm 57$	< 0.16

### 3.2.7 TIC 25375553/WASP-111 b

WASP-111 b is a hot Jupiter that orbits a ( $m_V = 10.3$ ) rapidly rotating F-5 type star with an effective temperature of 6400 K [59] in about 2.31 days. It was discovered by Anderson et al. 2014 [1]. From the Rossiter–McLaughlin effect, the orbit was found to be prograde with a sky-projected stellar obliquity of  $\lambda = -5 \pm 16^\circ$ . Wong et al. 2021 [59] report a marginal detection ( $\approx 2.8\sigma$ ) of the secondary eclipse of depth  $102 \pm 38$  ppm from sector 1 of TESS data. Before performing joint analysis of sectors 1 and 28, our sector 1 analysis gives exactly the same results,  $f_p = 102 \pm 38$  ppm.

When analyzing sectors 1 and 28 jointly, we only detrend the sector 28 SAP data and use the PDCSAP flux for sector 1. The final analysis gives a statistically significant  $> 3.3\sigma$  detection with  $f_p = 111 \pm 32$  ppm. This value is within  $0.2\sigma$  of value reported by Wong et al. 2021 [59] and from our analysis of sector 28 data, we get a significant ( $> 3\sigma$ ) detection  $f_p = 118 \pm 39$  ppm. We use this value to derive other results. In our joint sector analysis, we face an issue with convergence in MCMC (see corner plot 4.5) as some walkers converge to local solutions but the correlation plot has a high-density region in each fitted parameter where most of the samples lie around maximum likelihood. We are confident that a converged solution will yield similar results as our analysis indicates. So, we proceed for further analysis using results from sector 28 only. For the GP model, we use a Matérn-3/2 kernel and for fitting, we use 88 walkers with 3000 MCMC steps.

Further, the equilibrium temperature of the planet assuming full heat redistribution  $f = 1$  and  $A_B = 0$  gives  $T_{eq} = 2168 \pm 14K$  which is well within  $0.5\sigma$  of  $T_{eq} = 2140 \pm 62K$  as reported by Anderson et al. 2014 [1]. The expected thermal contribution to the occultation depth is  $f_{p,th} = 84$  ppm, assuming no heat redistribution i.e  $f = 2$  and that from reflected part computed using  $f_p$  and  $f_{p,th}$  is  $f_{p,rf} = 34$  ppm. Using this eclipse depth, we get a theoretical upper limit on  $A_g < 0.27$ . Observed eclipse depth  $f_p$  gives brightness temperature  $T_b = 2277 \pm 78K$  at 0.722 micron and is larger than  $T_{eq} = 2168 \pm 14K$  which assumes full heat redistribution. Lastly, We also calculate expected secondary eclipse depth of 37 ppm in the CHEOPS bandpass.

**Table 3.7:** WASP-111 b: Derived parameters based on secondary eclipse analysis.

$f_p$ (ppm)	$f_{p,th}$ (ppm)	$f_{p,rf}$ (ppm)	$T_{eq}$ (K)	$T_b$ (K)	$A_{g,th}$
$118 \pm 39$	84	34	$2168 \pm 14$	$2277 \pm 78$	$< 0.27$

### 3.2.8 TIC 16740101/KELT-9 b/HD 195689 A b

KELT-9 b is an ultra-hot giant that orbits on a nearly polar orbit around a ( $m_V = 7.56$ ) rapidly rotating A0 type star with an effective temperature of 10170 K [23] in about 1.48 days and was discovered by Gaudi et al. 2017 [23]. Wong et al. 2021 [59] report a significant detection ( $35\sigma$ ) of the secondary eclipse of depth  $630 \pm 18$  ppm from sector 14 & 15 of TESS data. We also use sectors 14 and 15 and first remove the bad data in sector 14. The joint model (BATMAN+GP) analysis of the PDCSAP flux gives a statistically significant  $> 27\sigma$  detection with  $f_p = 608 \pm 22$  ppm. This value is within  $0.8\sigma$  of the value reported by Wong et al. 2021 [59]. For the GP model, we use Matérn-3/2 kernel and for joint sector fitting, we use 128 walkers with 2500 MCMC steps. We do not account for the gravity darkening effect in the transit model as it does not affect the occultation depth.

The equilibrium temperature of the planet assuming heat redistribution  $f = 1$  and  $A_B = 0$  is  $T_{eq} = 4062 \pm 13K$  which is well within  $0.1\sigma$  of  $T_{eq} = 4050 \pm 180K$  as reported by Gaudi et al 2017 [23]. The expected thermal contribution in occultation depth is

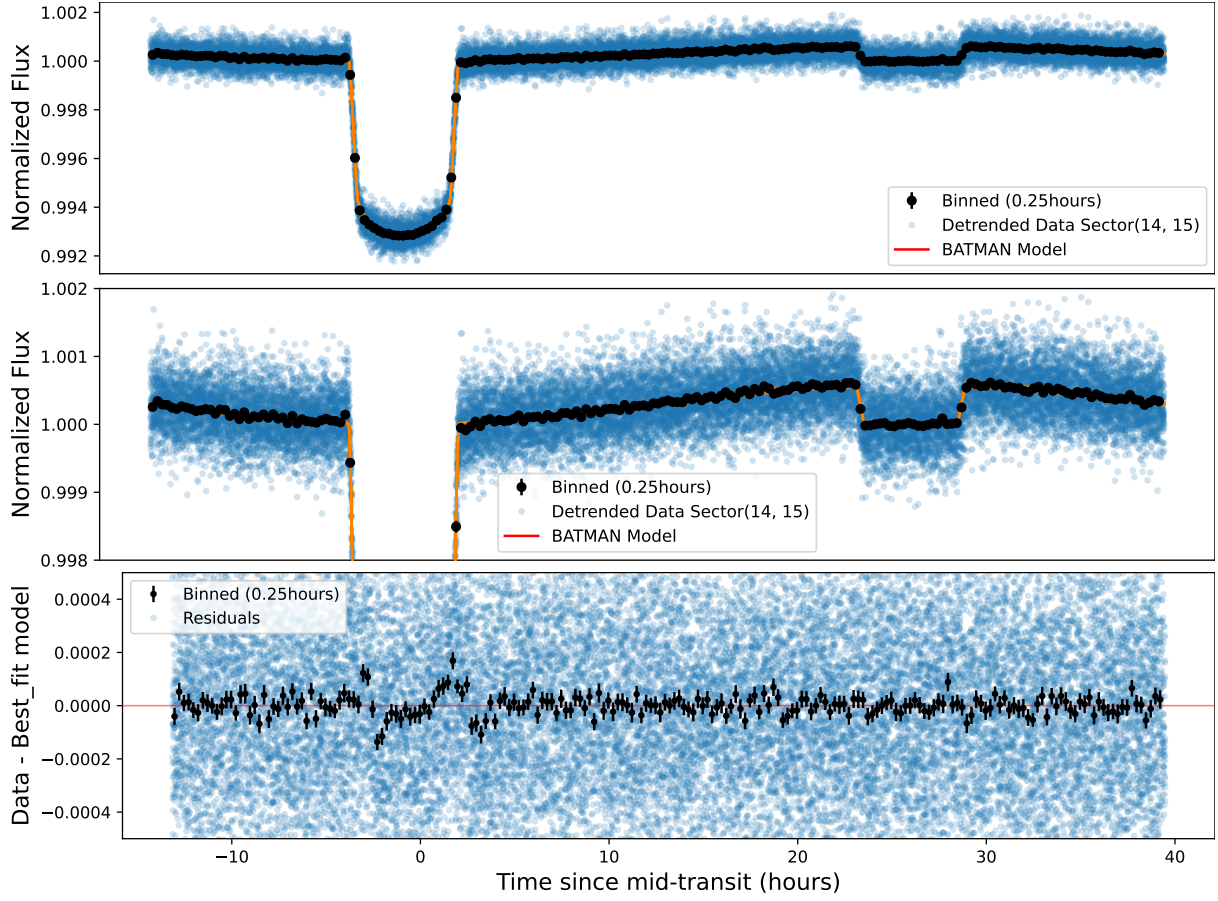


**Figure 3.10:** Figure(top) showing 100 BATMAN models plotted over detrended data of KELT-9 b (sector 14 & 15). (Middle) Zoom-in view of the above and residuals (bottom) obtained with best fit GP+BATMAN model. A higher asymmetric dispersion( see binned data points in black) in residuals during in-transit is present because we don't model for gravity darkening effect.

$f_{p,th} = 673$  ppm assuming no heat redistribution i.e  $f = 2$ . Using  $f_{p,th}$  and  $f_p$  we get a negative value for contribution from expected reflected flux, which means the planet's day side temperature is more than expected which further points to no heat redistribution and further negligible value of  $A_g \approx 0$  also indicated by Wong et al. 2020 [60]. At such temperatures, we can also rule out the formation of clouds as indicated by the author.

Observed eclipse depth  $f_p$  gives brightness temperature  $T_b = 3600 \pm 26K$  at 0.722 micron assuming  $f = 1$  and is less than  $T_{eq} = 4062 \pm 13K$  due to  $A_g \approx 0$ . We also calculate expected secondary eclipse depth of 390 ppm in the CHEOPS bandpass which makes it a fairly good target for follow-up observation.

**Table 3.8:** KELT-9 b: Derived parameters based on secondary eclipse analysis.

$f_p(ppm)$	$f_{p,th}(ppm)$	$f_{p,rf}(ppm)$	$T_{eq}(K)$	$T_b(K)$	$A_{g,th}$
$608 \pm 22$	673	-65	$4062 \pm 13$	$3600 \pm 36$	$\approx 0$

### 3.2.9 TIC 100100827/WASP-18 b/TOI-185 b

WASP-18 b is an ultra-hot giant that orbits on a nearly polar orbit around a ( $m_V = 9.3$ ) rapidly rotating F6 type star with an effective temperature of 6431 K Blazek et al. 2022 [5] in about 0.94 days and was discovered by Southworth J. et al. 2009 [48]. Shporer et al. 2019 [45] report a significant detection ( $\approx 16\sigma$ ) of the secondary eclipse of depth  $341 \pm 18$  ppm from sector 2 and 3 TESS data. We also use sector 2 and 3 data and first remove some bad data in sector 3. The  $f_p$  values found from the individual sector analysis are well within  $1\sigma$  of values from Shporer et al. 2019 [45]. The joint sector analysis of PDCSAP flux from sectors 2 and 3 gives a significant  $> 10\sigma$  detection with  $f_p = 346 \pm 32$  ppm. This value is well within  $0.8\sigma$  of the value reported by Wong et al. 2021 [59]. However, like WASP-111 b, we face a similar issue as some walkers get stuck in local minima (see corner plot 4.6). We also tried initial parameters, especially  $a/R_*$ , which were offset from those of Shporer et al. 2019 [45], attempting to reach convergence, but still the issue persist. However, we are confident that a converged solution will yield similar results as our joint sector analysis indicates. So, we proceed for further analysis using results from sector 2 only where we get  $f_p = 369 \pm 23$  ppm. For the GP model, we use a Matérn-3/2 kernel and for the fitting, we use 88 walkers with 3000 MCMC steps.

The equilibrium temperature of the planet assuming heat redistribution  $f = 1$  and  $A_B = 0$  is  $T_{eq} = 2424 \pm 9K$  which is within  $1.5\sigma$  of  $T_{eq} = 2504 \pm 64K$  as reported by M. Blazek et al. 2022 [5]. The expected thermal contribution in occultation depth is  $f_{p,th} = 76$  ppm assuming full heat redistribution and that from reflected part computed using  $f_p$  and  $f_{p,th}$  is  $f_{p,rf} = 293$  ppm. Using this eclipse depth, we get an upper limit on  $A_g < 0.38$  similar to values from M. Blazek et al. 2022 [5]. However, Shporer et al. 2019 [45] found an inefficient day-night energy redistribution with infrared observations and upon integrating their atmosphere model in the TESS bandpass, they get  $f_{p,th} = 327$  ppm. Using this value and  $f_p$  from our analysis, we place an upper limit on  $A_g < 0.05$ , which is similar to the reported ones  $A_g < 0.048$  in the same publication. With this and considering high equilibrium temperature, we also rule out the formation of clouds on the day side.

Observed eclipse depth  $f_p$  gives a brightness temperature  $T_b = 2532 \pm 22K$  at 0.722 micron assuming  $f = 1$  and is higher than  $T_{eq} = 2424$ . We also calculate expected secondary eclipse depth of 119 ppm assuming  $f = 2$  in the CHEOPS bandpass which makes it a good target for follow-up observation.

**Table 3.9:** WASP-18 b: Derived parameters based on secondary eclipse analysis.

$f_p(ppm)$	$f_{p,th}(ppm)$	$f_{p,rf}(ppm)$	$T_{eq}(K)$	$T_b(K)$	$A_{g,th}$
$369 \pm 23$	76	293	$2424 \pm 9$	$2532 \pm 22$	$< 0.05$

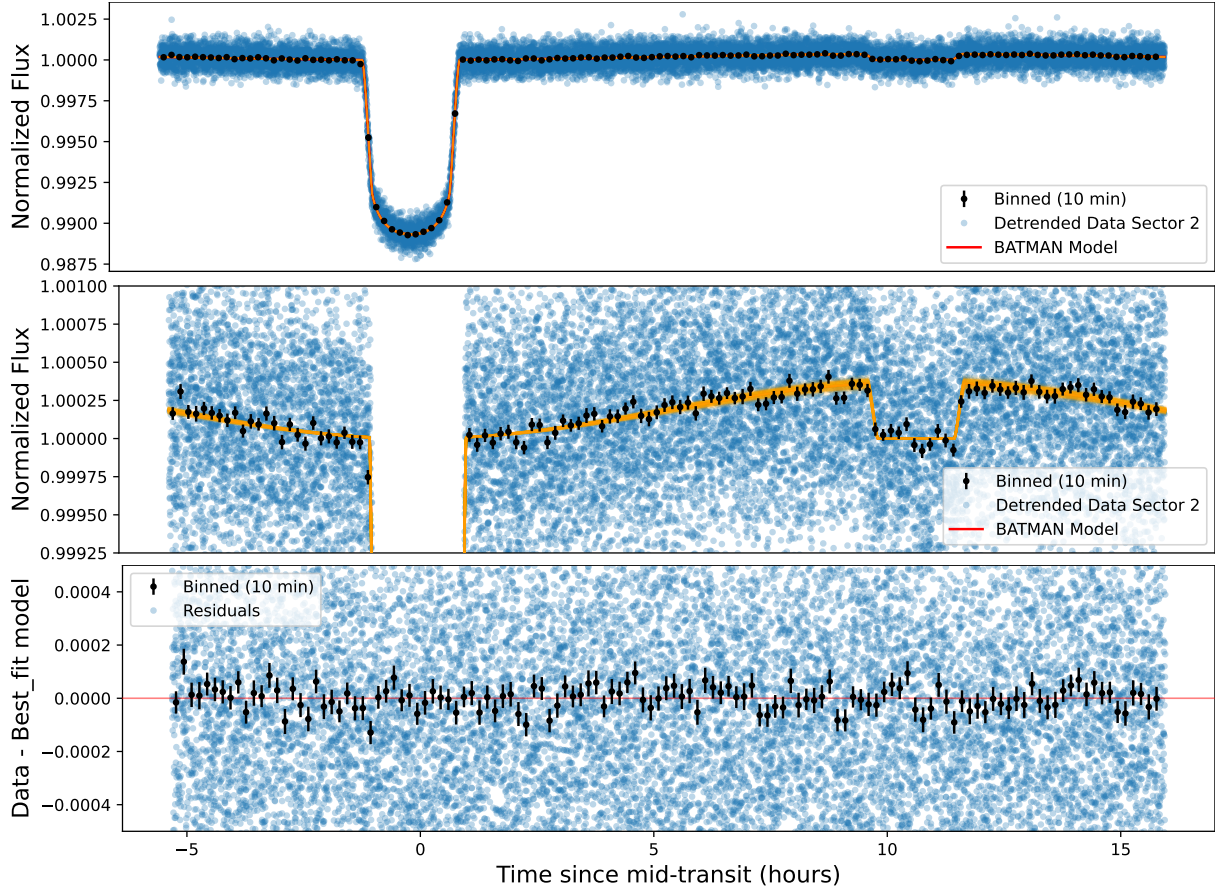


**Figure 3.11:** Figure(top) showing 100 BATMAN models plotted over detrended data of WASP-18 b (sector 2). (Middle) Zoom-in view of the above and residuals (bottom) obtained with best fit GP+BATMAN model.

### 3.2.10 Marginal Detections

In the previous section 3.2, we presented our analysis, derived results and their comparison with previous literature only for those hot Jupiters where we get at least a  $3\sigma$  detection of the secondary eclipse from WASP-95 b, KELT-26 b, WASP-94 A b, HAT-P-30 b, KELT-3 b, TIC 362709886, KELT-17 b and HAT-P-49 b (see table 4.3). Here, we present our results for all these 8 marginal detections, most of which have not been reported so far. A detailed discussion on each of the 8 hot Jupiters is not attempted here given the scope of this thesis and therefore we only present relevant plots and figures. In all 8 figures, similar to previous ones from detections, the top panel shows 100 BATMAN models which are plotted over detrended data of the planet. The middle panel shows a zoom-in view on the top panel and residuals obtained with the best fit (GP+BATMAN) model are shown in the bottom panel.

### 3.2.11 Non Detections

Besides 9 detections and 8 marginal, we get 12 non-detections. For these targets (TIC 170634116, TIC 452808876, TIC 425206121, TIC 379929661, TIC 65412605, TIC 281408474, TIC 176899385, TIC 138168780, TIC 8400842, TIC 67666096, TIC

61098812 , TIC 39858507 ), we perform analysis with both SAP and PDCSAP flux and data is used from all available sectors where extracted photometry data is available. In most of these targets, we obtain a negative eclipse depth  $f_p$  when using PDCSAP flux which as earlier mentioned shows they are not detrended well from SPOC pipeline. From SAP flux analysis, we obtain  $f_p$  values consistent either with zero or well below  $< 1\sigma$ .

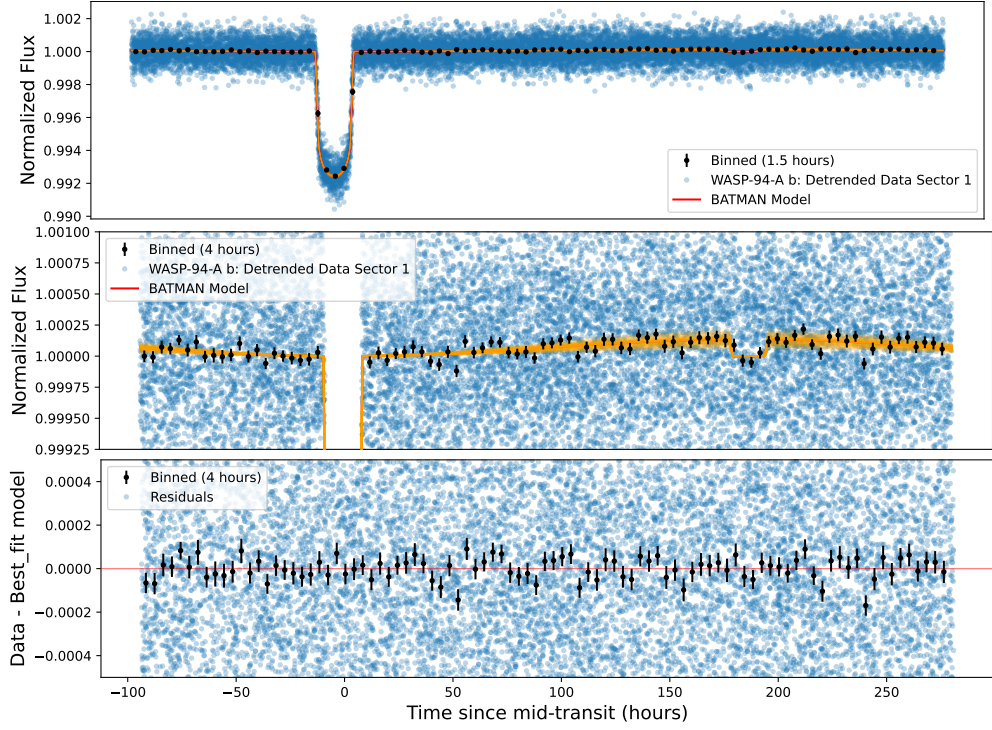


**Figure 3.12:** WASP-94 A b (sector 1,27)

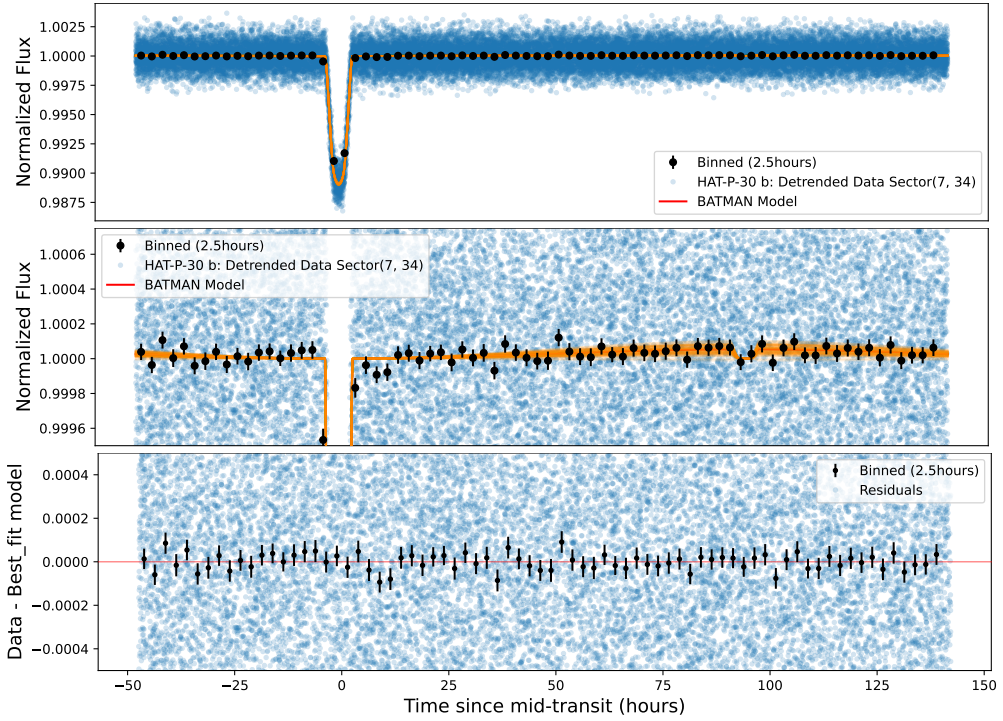


**Figure 3.13:** HAT-P-30 b (sector 7, 34)

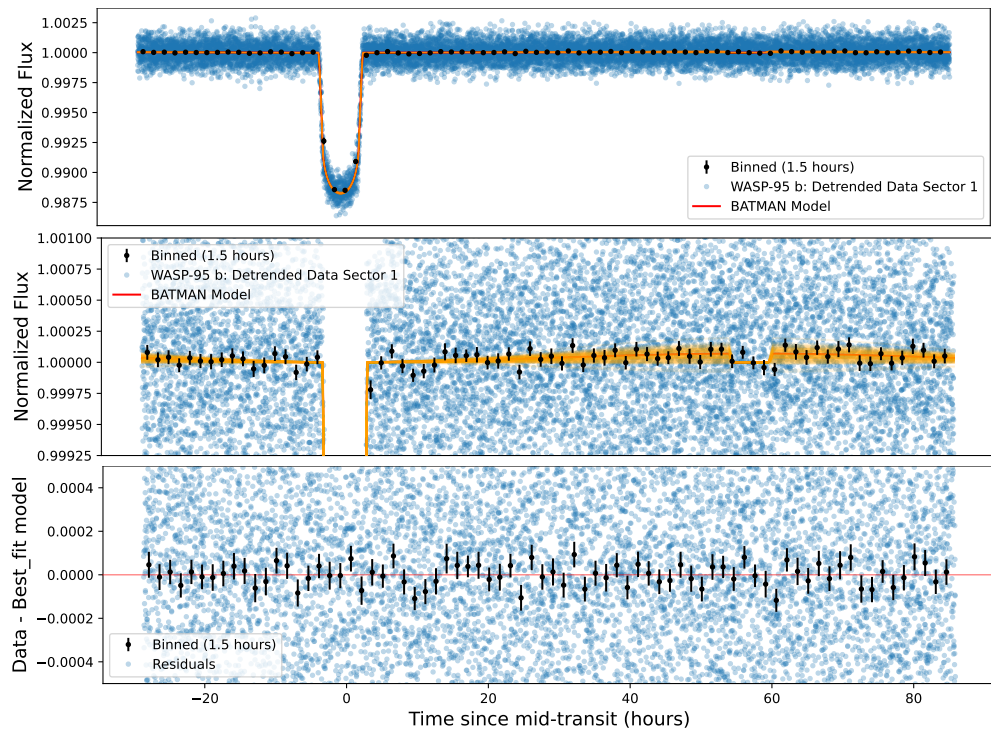


**Figure 3.14:** WASP-95 b (sector 1)

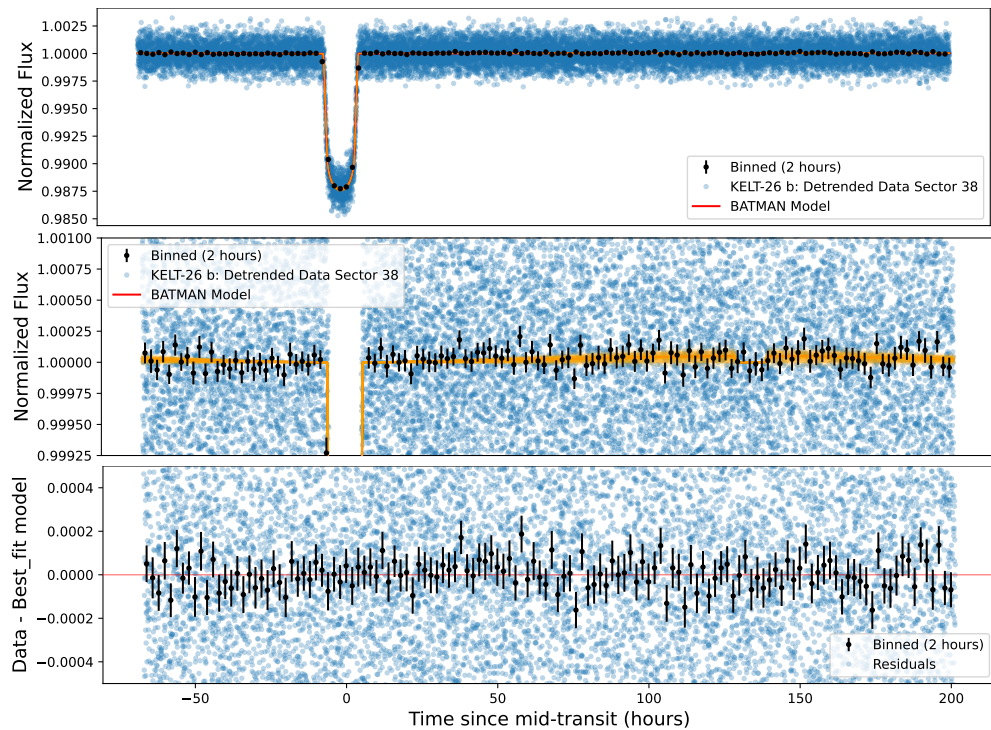


**Figure 3.15:** KELT-26 b (sector 38)

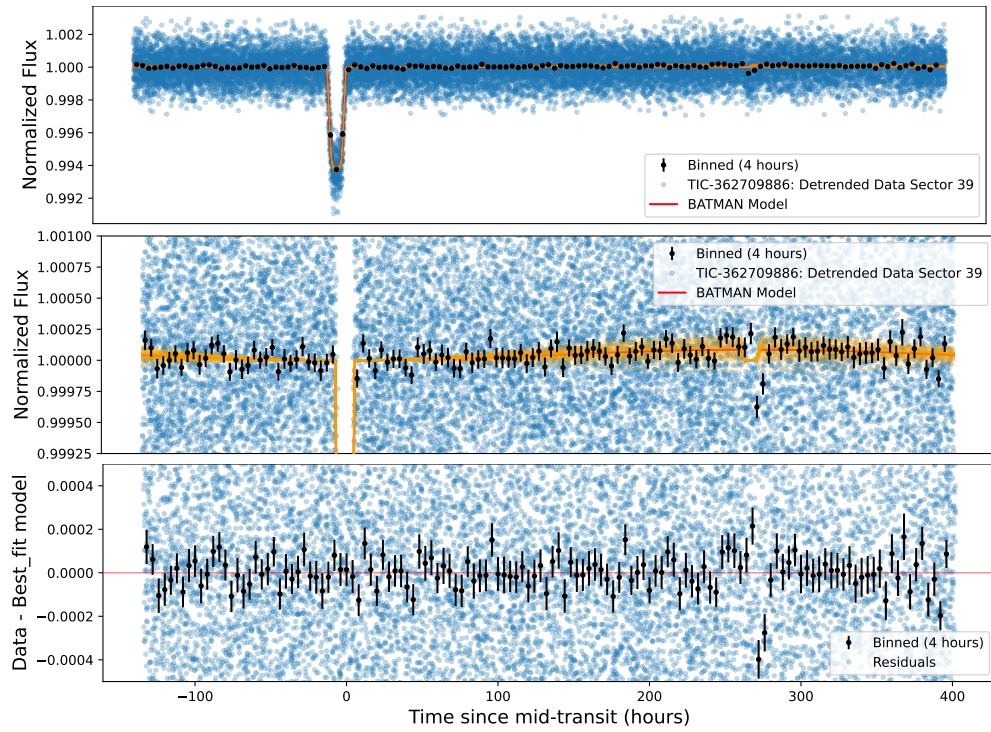


**Figure 3.16:** TIC-362709886 (sector 39)

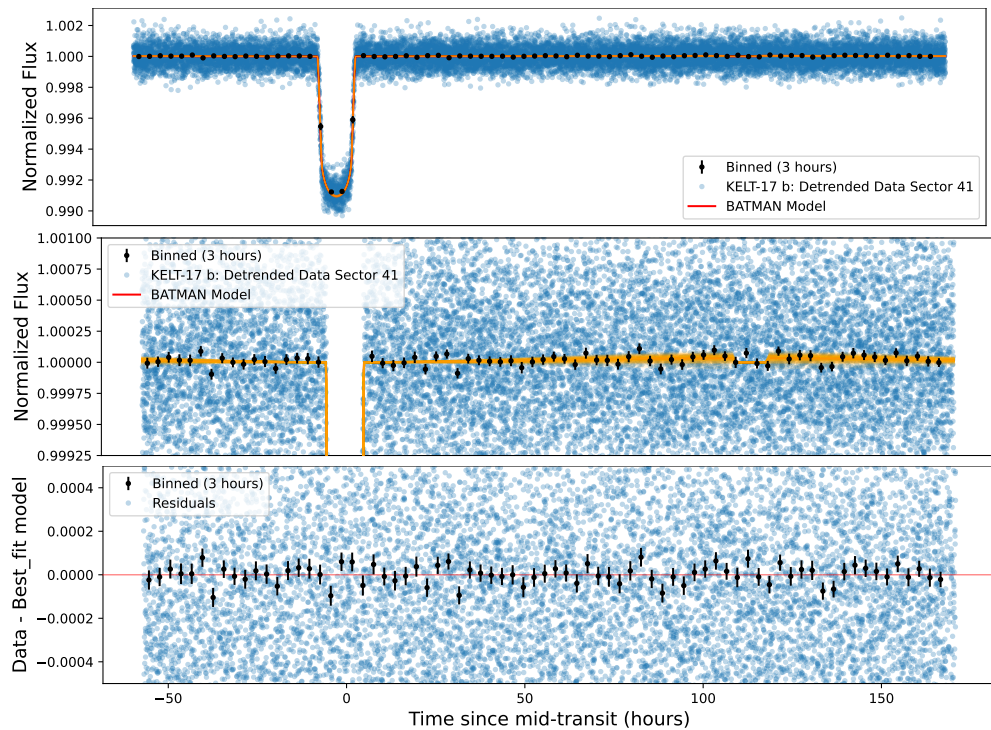


**Figure 3.17:** KELT-17 b (sector 46)

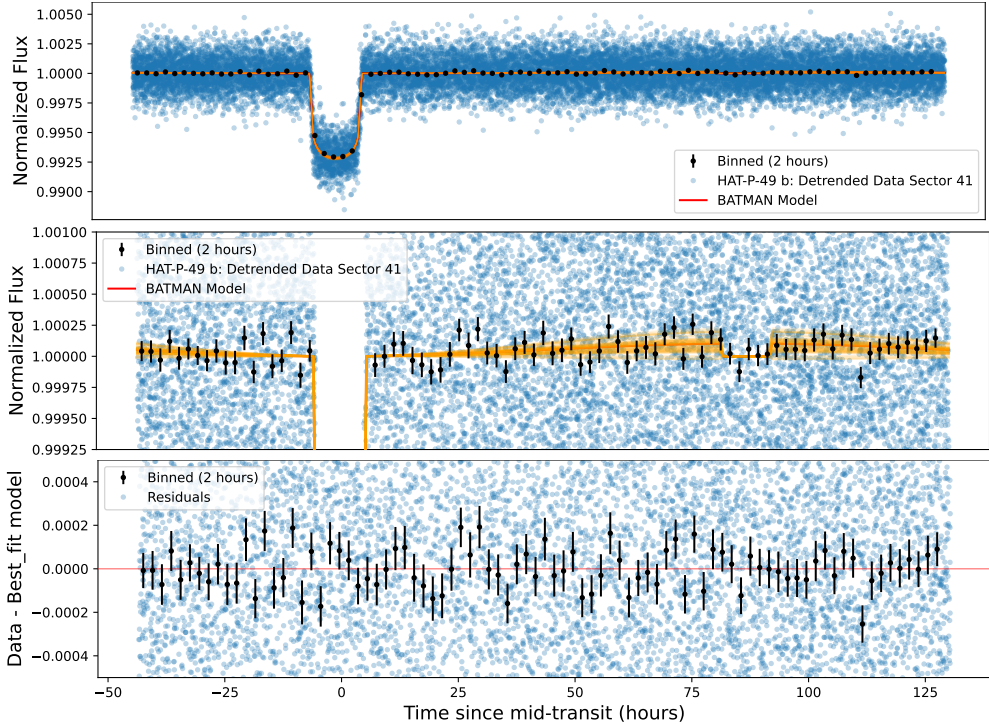


**Figure 3.18:** HAT-P-49 b (sector 41)

### 3.3 Results

We analyze a total of 29 hot Jupiters to detect secondary eclipses. We get detection from 9 of them, out of which 4 (see section 3.2.1, 3.2.2, 3.2.3, 3.2.4) are new, 3 (see section 3.2.7, 3.2.6, 3.2.5) improved to at least  $3\sigma$  confidence, which earlier were reported as marginal and results from the remaining 2 (see section 3.2.9, 3.2.8) which have been already detected are well within  $1\sigma$  of respective occultation depths from our analysis. Apart from these 9 planets, we also get 8 new marginal detections not reported so far.

In this section, we perform some statistics with derived results to further understand observational and physical aspects of hot Jupiters. In the section 3.2, we calculate expected occultation depth in TESS and CHEOPS bandpass, equilibrium temperature ( $T_{eq}$ ) and brightness temperature ( $T_b$ ) for individual planets. Here we try to give a broader perspective on various aspects. With only 9 planets out of more than 400 hot Jupiters detected so far, statistical approach would be biased but it is an attempt to reconcile our results with previous literature.

#### 3.3.1 Observational and Physical Aspects of Hot Jupiters

The planet population plot (see Fig. 3.19) shows all confirmed planets up to today. Planets in orange are the hot Jupiters for which we have a significant detection of the secondary eclipse. The equilibrium temperature  $T_{eq}$  calculated for all these planets assuming both no heat redistribution and bond albedo  $A_B = 0$  is well above 2000 K.

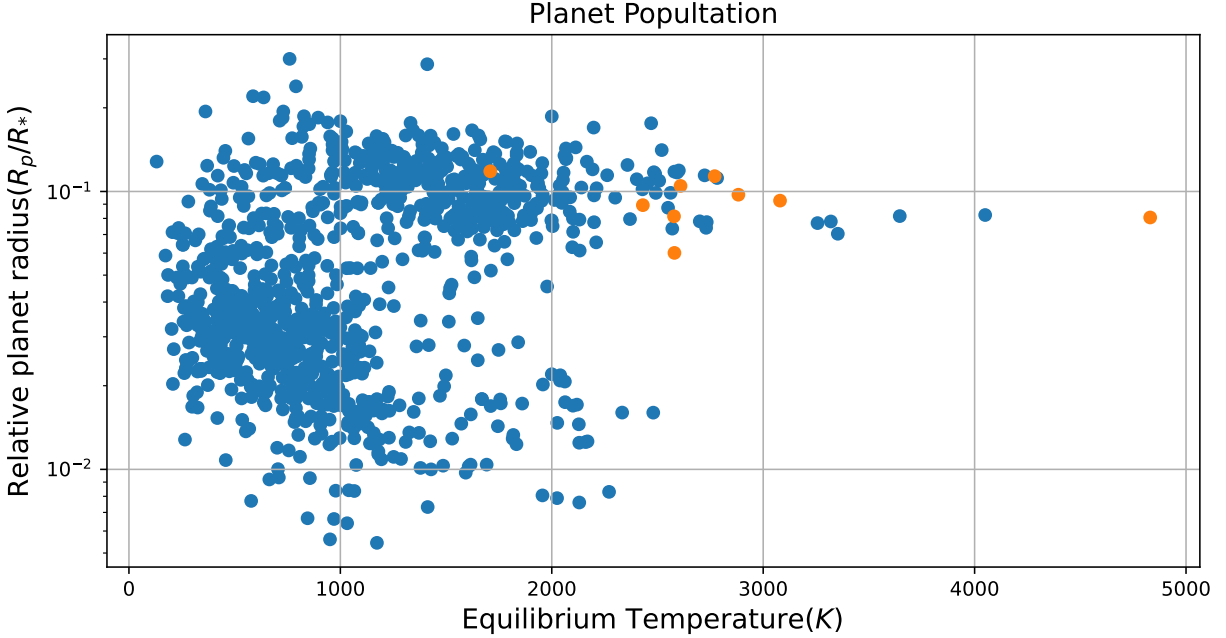


**Figure 3.19:** Figure showing all planets discovered till date (blue) along with hot Jupiters for which we get a detection on secondary eclipse.

Considering full heat redistribution,  $T_{eq}$  is still above 2000 K for each planet except for WASP-77 A b ( see section 3.2.6). First observational constraints from this work would be eclipses for hot Jupiters with  $T_{eq} > 1678$  are detectable from space based telescope like TESS. However, this is just one factor among many, which also includes magnitude of the star ( $m_V$ ) and planet's relative size  $R_p/R_*$ .

The transmission function of TESS (see Fig. 3.1) covers a wavelength range of about (0.6 - 1  $\mu\text{m}$ ) covering some portion both of visible and near infrared wavelengths. If we look at blackbody curves (see Fig. 3.20) of all 9 planets, they also emit significantly in infrared. Since TESS does not cover this range fully, it does not capture the planetary flux at longer wavelength.

Since we aim to find good planets that shows robust eclipse depths which could be observed by CHEOPS, we find, KELT-7 b (see section 3.2.3 ), HAT-P-70 b (see section 3.2.5), WASP-76 b (see section 3.2.4) , WASP-111 b (see section 3.2.7 ), WASP-18 b (see section 3.2.9 ) and KELT-9 b (see section 3.2.8) as potential candidates considering their eclipse depth and blackbody curves. Among all of them, KELT-9 is the best given  $f_p = 608 \pm 22$  ppm and its blackbody curve peak where CHEOPS transmission is maximum and significant planet's emission covers the CHEOPS bandpass. For each planet, we also calculate the expected eclipse depth from CHEOPS in section 3.2, considering those values, only two planet WASP-18 b (see section 3.2.9) and KELT-9 b (see section 3.2.8) are strong candidates given  $f_{p,CHEOPS} > 100$  ppm. HAT-P-70 b (see section 3.2.5) and WASP-76 b (see section 3.2.4) has  $f_{p,CHEOPS} > 60$  ppm.

The blackbody approximation of hot Jupiters in our sample assuming  $T_p = T_{eq}$  with

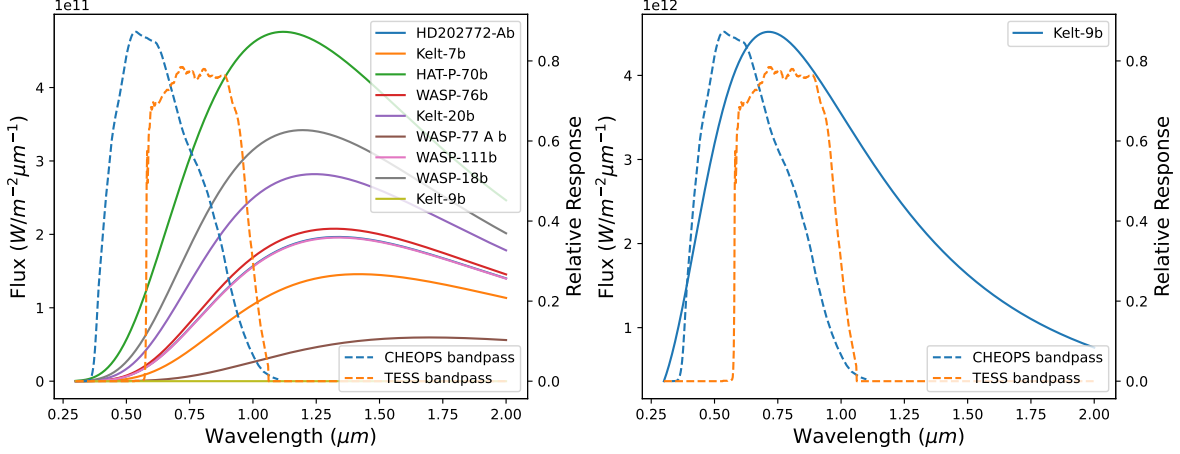


**Figure 3.20:** Planets from our analyzed sample approximated as blackbody assuming  $T_p = T_{eq}$  with inefficient heat-redistribution  $f = 2$  and  $A_B = 0$ . Plotted in dash lines are bandpass of TESS and CHEOPS.

inefficient heat-redistribution  $f = 2$  and  $A_B = 0$ , shows most of them peak around 1 micron in near infrared. As expected, emission from these highly irradiated planets subjected to high UV and X-ray radiation from the host star, are dominated by thermal flux. TESS which barely touches the 1 micron mark is not very sensitive to these fluxes and beyond, and hence expected contribution from thermal flux  $f_{p,th}$  estimated for most of them is less than  $f_p$ .

### 3.3.2 $T_{eq}$ Vs the ratio of $T_{eq}/T_b$

Equilibrium temperature  $T_{eq}$  for the planet is calculated assuming both star and planet emitting flux as blackbody and  $T_b$  is calculated at  $0.722\mu m$  using  $f_p$ . Two plots shown (see Fig 3.21 ) are computed for both full heat redistribution and no heat redistribution case. If we consider the first model for all the hot Jupiters,  $T_b$  seems to dominate for most the planet which implies that  $T_{eq}$  of the planet is not sufficient to explain  $T_b$  and hence another source of energy, either external or internal of the planet would be required to explain such high brightness temperatures and thus it further suggest reflected light from these planets is not negligible.

This reflected light might be due to the presence of clouds and hazes in the atmosphere. We can see,  $T_b$  dominate at lower  $T_{eq}$ , meaning a lower flux contribution is expected from the thermal component in the occultation depth. Another possible explanation for larger  $T_b$  could be the blackbody approximation which is based on  $T_{eq}$  and is not good. If we look at the blackbody curve of all these planets, we find that they peak well outside the mark of visible band. Hence, these approximations.

Further, as we go at higher  $T_{eq}$ , the impact of  $T_b$  decreases and an example of this could be seen in both the plots where the ratio of  $T_{eq}/T_b$  for Kelt-9b is above 1 both for full( $f = 1$ ) and zero heat redistribution( $f = 2$ ) case. We also see a positive correlation

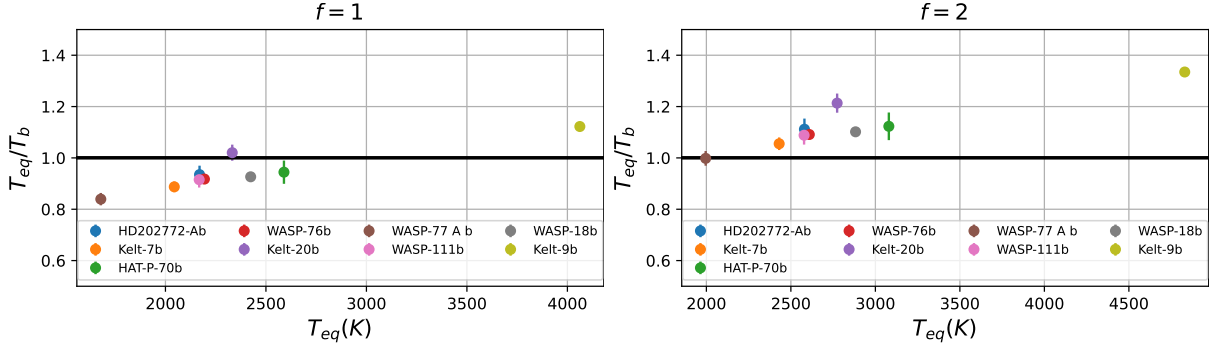


**Figure 3.21:** Figure(left) showing  $T_{eq}$  Vs the ratio of  $T_{eq}/T_b$  considering full heat redistribution. A higher  $T_{eq}$  compared to brightness temperature increase with as  $T_{eq}$  increase. Figure(right) showing the same but considering no heat redistribution.

between  $T_{eq}/T_b$  and  $T_{eq}$  for both models. For  $f = 2$ , we can at least rule out the formation of clouds and this has been suggested by previous works for highly irradiated planets with  $T_{eq} > 1900K$ .

### 3.3.3 Bond Albedo ( $A_B$ ) Vs Equilibrium Temperature ( $T_{eq}$ )

The equilibrium temperature considering different models for a planet having  $f = 1, 1.5, 2$  i.e full heat redistribution, partial and no heat redistribution respectively, can give both an individual and global constraints on albedo of hot Jupiters. We can infer from plots (see Fig. 3.22), all 9 planets from our analysis have bond albedo  $A_B < 0.4$ , except for KELT-9 b and KELT-20 b if we consider  $f = 2$  i.e no heat redistribution, which most of the earlier works suggest for hot and ultra-hot Jupiters.

For KELT-9 b, Wong et al. 2020 calculate  $A_B \approx 0.19$ , comparing our results, we can easily rule out model  $f = 2$  and  $f = 1.5$ . Assuming  $f = 1$ , a lower albedo indicates efficient heat redistribution. As discussed in subsection 3.2.3, dissociation and recombination of  $H_2$  enhances energy redistribution between day and night side on such hot Jupiters under high irradiation.

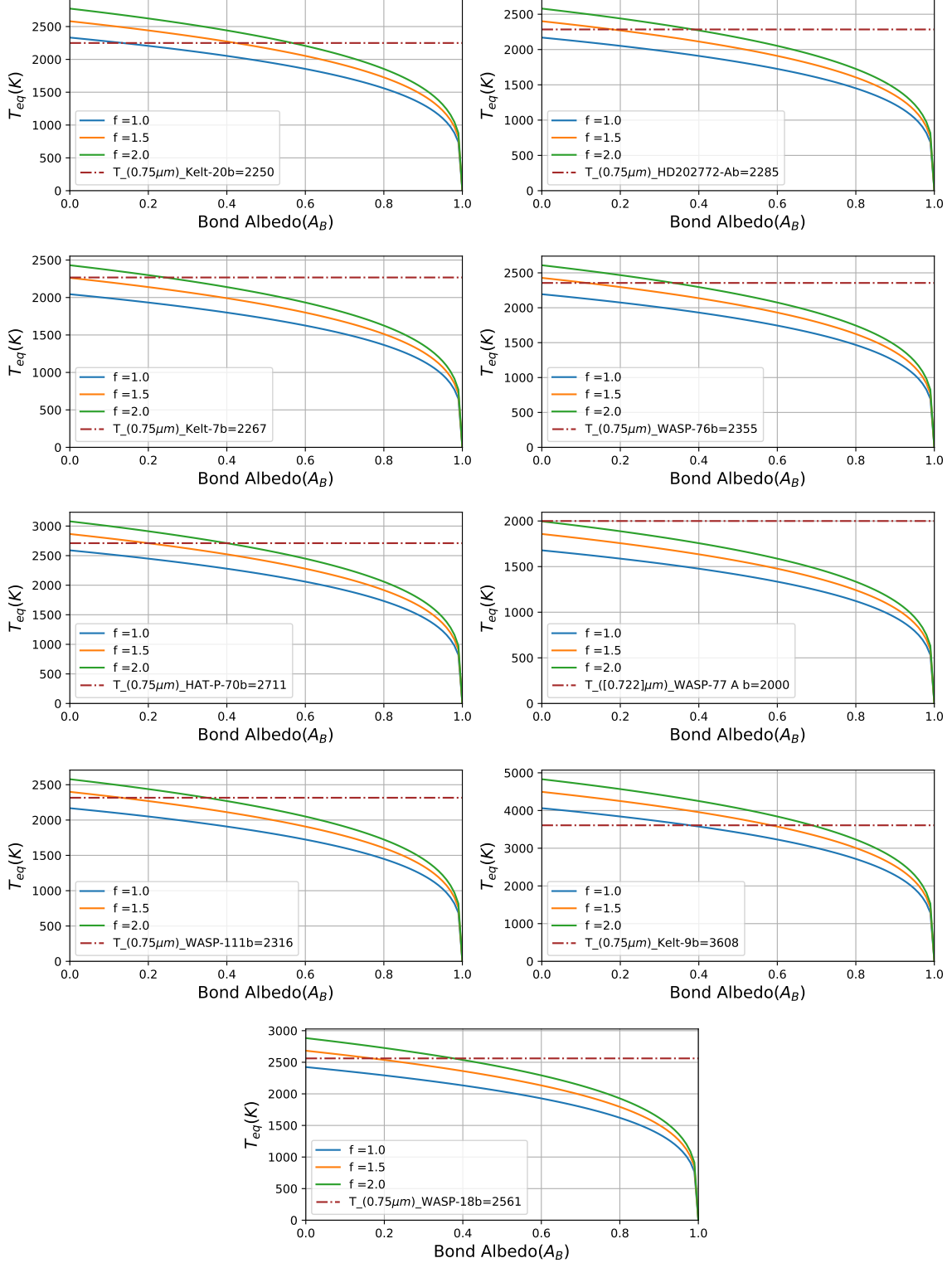


**Figure 3.22:** Figure(left) Plots showing  $T_{eq}$  as a function of bond albedo for different models of the atmosphere assuming heat redistribution of  $f = 1, 1.5, 2$ . Dash-dot line shows day side brightness temperature of the planet at  $0.722\mu m$  calculated using observed eclipse depth  $f_p$ .



# Chapter 4

## Conclusion & Next Work

Hot Jupiters are an important class of planets for which photometry and spectroscopy help retrieve planetary physical and orbital parameters, atmosphere, composition, temperature & pressure profile, clouds & hazes, winds, and further understanding of the impact of host star on the planet, atmospheric escape mechanism and planetary evolution. Transit photometry is one such strong tool, more specifically, the secondary eclipse and phase curve which can constrain the geometric and bond albedo of these hot gas giants. This further help in determining the energy budget of these hot Jupiters and facilitate addressing some of the aforementioned problems.

Astronomers have been detecting eclipses for a long time in the history of exoplanets research. With the accelerated development of sophisticated models and tools, astronomers started focusing on detecting eclipses apart from transit. Despite this, it is still more challenging than detecting a transit. In this work, we employed three different models, beginning from BLS to more inclusive BATMAN and lastly, the state-of-the-art GP model. We saw how BLS compared to BATMAN was not sufficient to include the impact of different orbital parameters in modeling the light curve. Similarly, we saw how BATMAN being a parametric model did not account for correlated noise induced by the stellar pulsation as seen from the residuals of WASP-33 b analysis.

For a significant number of cases among 28 hot Jupiters, analysis of PDCSAP flux with BATMAN gave a high negative value of eclipse depth, implying improper detrending of the data from the TESS SPOC pipeline. To tackle this problem we detrended raw (SAP flux) data using GP. Finally joint model of GP & BATMAN helped in detecting eclipses for 9 hot Jupiters with statistical significance  $> 3\sigma$  and for 8 of them, we get a marginal detection. None of the marginal detections showed  $f_p > 100$  ppm with  $> 2.5\sigma$  significance.

Detection of secondary eclipses using Spitzer from previous studies has helped in constraining especially the geometric albedos for several hot Jupiters. Ground-based detection in the visible to the near-infrared regime has tried to address the hot Jupiter low albedo problem and astronomers were able to derive upper limits on geometric albedo.

TESS covering wavelengths partially in the higher end of visible and lower end of infrared has helped similarly. We also attempted this problem and were able to put an upper limit on geometric albedo. However, a better constraint on this physical parameter along with day side brightness temperature could be obtained with the combined fit of multiple eclipses over a set of wavelengths in visible and infrared.

We calculated both equilibrium and dayside brightness temperature and tried to constrain bond albedo, considering planetary models with different heat redistribution factors. Previous studies concerning transmission spectroscopy were used to select the most favourable circulation model, especially for KELT-9 b to explain its low albedo. Apart from this, equilibrium temperature Vs the ratio of equilibrium to brightness temperature showed a positive correlation for all the estimated values of the temperature ratios in both the full and no heat redistribution model, which tells the relative impact of equilibrium temperature is higher for planets with higher equilibrium temperature and vice-versa for brightness temperature.

Among 9 eclipse detection, 6 of them shows eclipse depth  $f_p \approx or > 100$  ppm. From this work, we find them suitable candidates for follow-up observation from CHEOPS, considering the bandpass of both TESS and CHEOPS. As a next step, it would be good to re-analyze all those targets with multiple sectors(if available) where we could present results only from one sector data. Further, a more sophisticated model for the phase curve where it accounts for atmospheric brightness modulation can help better constrain winds in the atmosphere. A simultaneous fit for the dayside and nightside temperature and retrieving unconstrained values for bond albedo and heat redistribution factor could provide a better explanation for atmospheric circulation. A thorough analysis of emitted light (Thermal + Reflected) of an interesting target for understanding the planet's upper atmosphere could also be attempted.

# Appendix

## A

**Table 4.3:** Results from marginal detections.

Target	Sector	$f_p(ppm)$
WASP-95 b	1	$70^{+48}_{-45}$
KELT-26 b	38	$50^{+33}_{-32}$
WASP-94 A b	1, 27	$82^{+58}_{-58}$
HAT-P-30 b	7, 34	$53^{+25}_{-26}$
KELT-3 b	21	$70^{+48}_{-45}$
TIC 362709886	39	$86^{+69}_{-66}$
KELT-17 b	46	$79^{+45}_{-46}$
HAT-P-49 b	41	$103^{+51}_{-52}$

**Table 4.1:** Results from WASP-33 b analysis with BATMAN only and (GP+BATMAN) model along with comparison with previous works.

Parameter	This Work(BATMAN)	This Work(GP+BATMAN)	Essen et al. 2020	Essen et al. 2014
$P[Days]$	$1.219936 \pm 4 \times 10^{-6}$	$1.219884 \pm 1.5 \times 10^{-5}$	$1.2198705 \pm 3.7 \times 10^{-6}$	$1.2198675 \pm 1.5 \times 10^{-6}$
$R_p/R_*$	$0.108557^{+0.000049}_{-0.000052}$	$0.109097^{+0.000593}_{-0.000533}$	$0.1087 \pm 0.0002$	$0.1046 \pm 0.0006$
$a/R_*$	$3.629209^{+0.001648}_{-0.001806}$	$3.658920^{+0.006630}_{-0.008665}$	$3.601 \pm 0.005$	$3.68 \pm 0.03$
$i$	$89.796430^{+0.147973}_{-0.228832}$	$89.359755^{+0.440277}_{-0.604519}$	$88.53 \pm 0.21$	$87.90 \pm 0.93$
$f_p[ppm]$	$446^{+9}_{-9}$	$466^{+103}_{-106}$	$305.8 \pm 35.5$	-

**Table 4.2:** Results from secondary eclipse detected targets analyzed with joint (GP+BATMAN model).

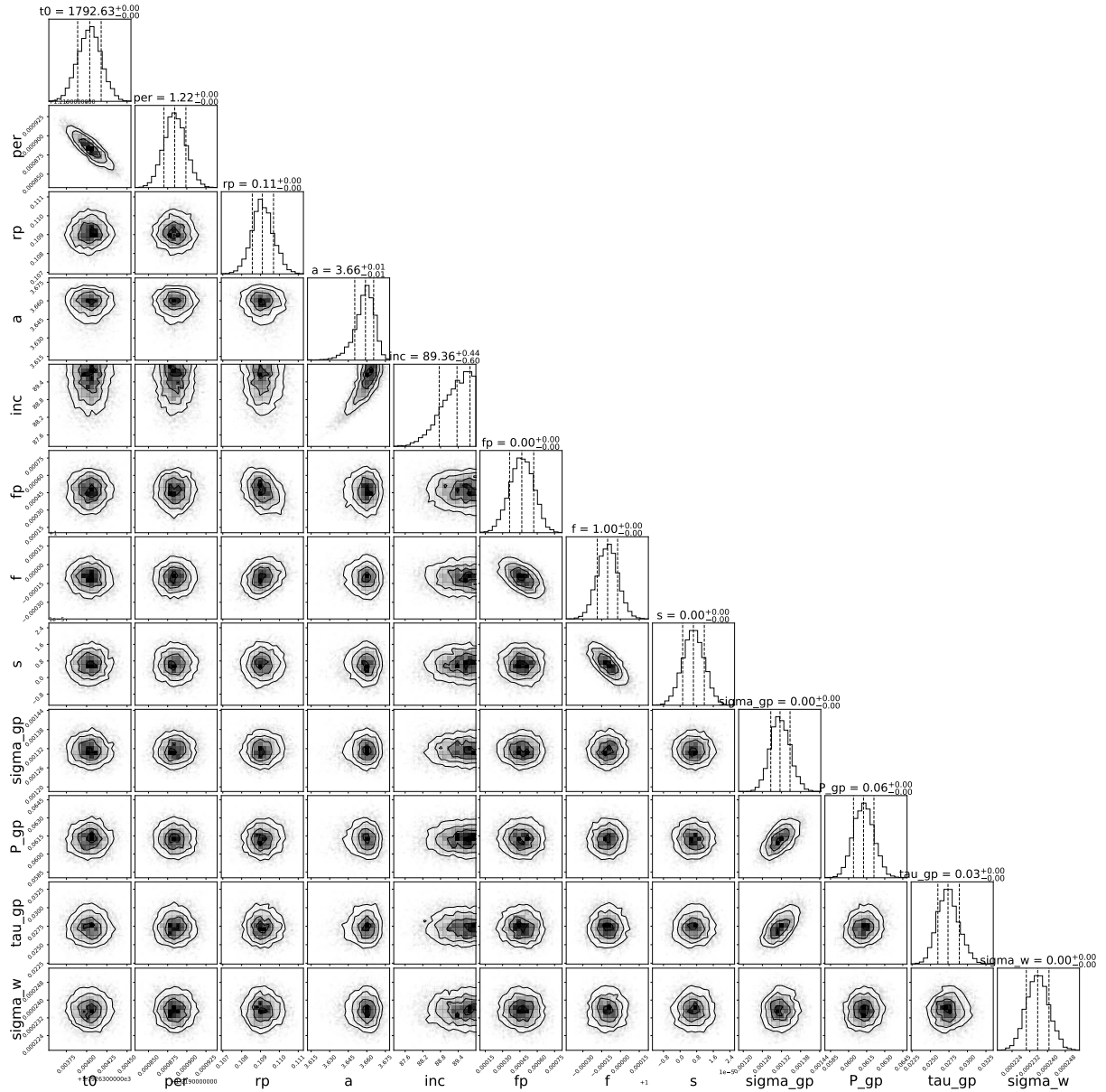
Parameter	KELT-20 b	TOI-123 A b	KELT-7 b	WASP-76 b
<b>Fitted Parameters</b>				
$T_0[BTJD]$	$1684.314609^{+0.000127}_{-0.000131}$	$1328.684053^{+0.000203}_{-0.000207}$	$2475.597165^{+0.000091}_{-0.000095}$	$2448.895270^{+0.000083}_{-0.000087}$
$P[Days]$	$3.474099^{+0.000001}_{-0.000001}$	$3.308876^{+0.000001}_{-0.000001}$	$2.734761^{+0.000004}_{-0.000003}$	$1.809880^{+0.000000}_{-0.000000}$
$R_p/R_*$	$0.113528^{+0.000117}_{-0.000115}$	$0.060105^{+0.000246}_{-0.000249}$	$0.089295^{+0.000140}_{-0.000145}$	$0.104723^{+0.000102}_{-0.000098}$
$a/R_*$	$7.411548^{+0.037386}_{-0.036005}$	$4.118749^{+0.074390}_{-0.069541}$	$5.513959^{+0.037022}_{-0.035712}$	$4.057756 \pm 0.003213$
$i(^o)$	$85.971375^{+0.075818}_{-0.074098}$	$83.133970^{+0.605892}_{-0.548578}$	$83.689870^{+0.116292}_{-0.114577}$	$89.755213 \pm 0.234634$

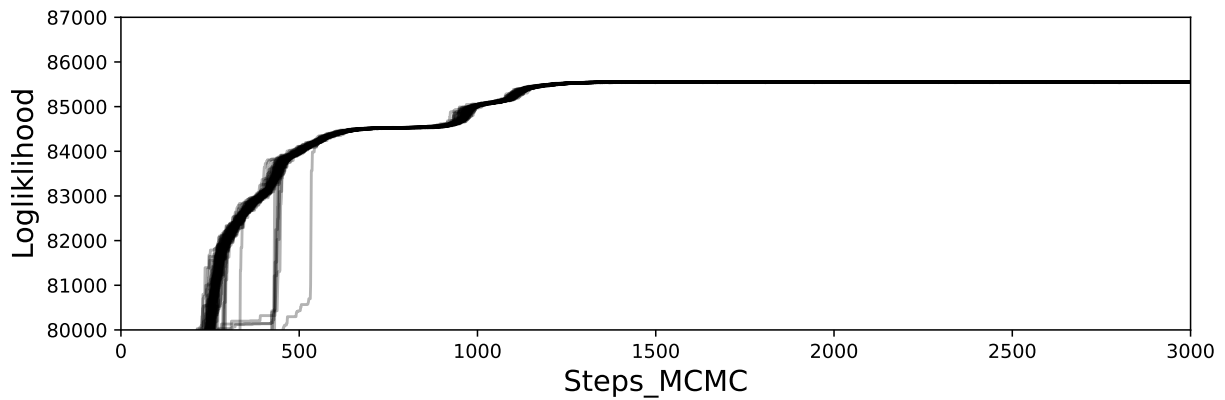
Parameter	HAT-P-70 b	WASP-77 A b	WASP-111 b	KELT-9 b
<b>Fitted Parameters</b>				
$T_0[BTJD]$	$2175.052793^{+0.000380}_{-0.000380}$	$2145.400184^{+0.000085}_{-0.000083}$	$2062.781941^{+0.000341}_{-0.000341}$	$1683.445364^{+0.000097}_{-0.000086}$
$P[Days]$	$2.744220^{+0.000067}_{-0.000068}$	$1.360031^{+0.000008}_{-0.000008}$	$2.310940^{+0.000063}_{-0.000061}$	$1.481119^{+0.000004}_{-0.000004}$
$R_p/R_*$	$0.092725^{+0.000653}_{-0.000655}$	$0.128372^{+0.000248}_{-0.000189}$	$0.081299^{+0.000406}_{-0.000420}$	$0.080617^{+0.000181}_{-0.000174}$
$a/R_*$	$5.323502^{+0.115701}_{-0.113558}$	$5.369481^{+0.022563}_{-0.043583}$	$4.393185^{+0.113588}_{-0.104162}$	$3.134360^{+0.019415}_{-0.018629}$
$i(^o)$	$96.391022^{+0.400306}_{-0.412795}$	$88.948763^{+0.735503}_{-0.702023}$	$80.948234^{+0.505009}_{-0.465307}$	$85.127624^{+0.491913}_{-0.434787}$

Parameter	WASP-18 b
<b>Fitted Parameters</b>	
$T_0[BTJD]$	$1354.457820^{+0.000061}_{-0.000062}$
$P[Days]$	$0.941459^{+0.000004}_{-0.000004}$
$R_p/R_*$	$0.097553^{+0.000170}_{-0.000175}$
$a/R_*$	$3.459302^{+0.025829}_{-0.024795}$
$i(^o)$	$83.779066^{+0.360875}_{-0.333759}$



**Figure 4.1:** Corner plot showing correlations between parameters along with their marginal distribution.



**Figure 4.2:** Plot showing progress of loglikelihood as a function of MCMC step number. It finally converged around a maximum likelihood after a jump from local maxima.

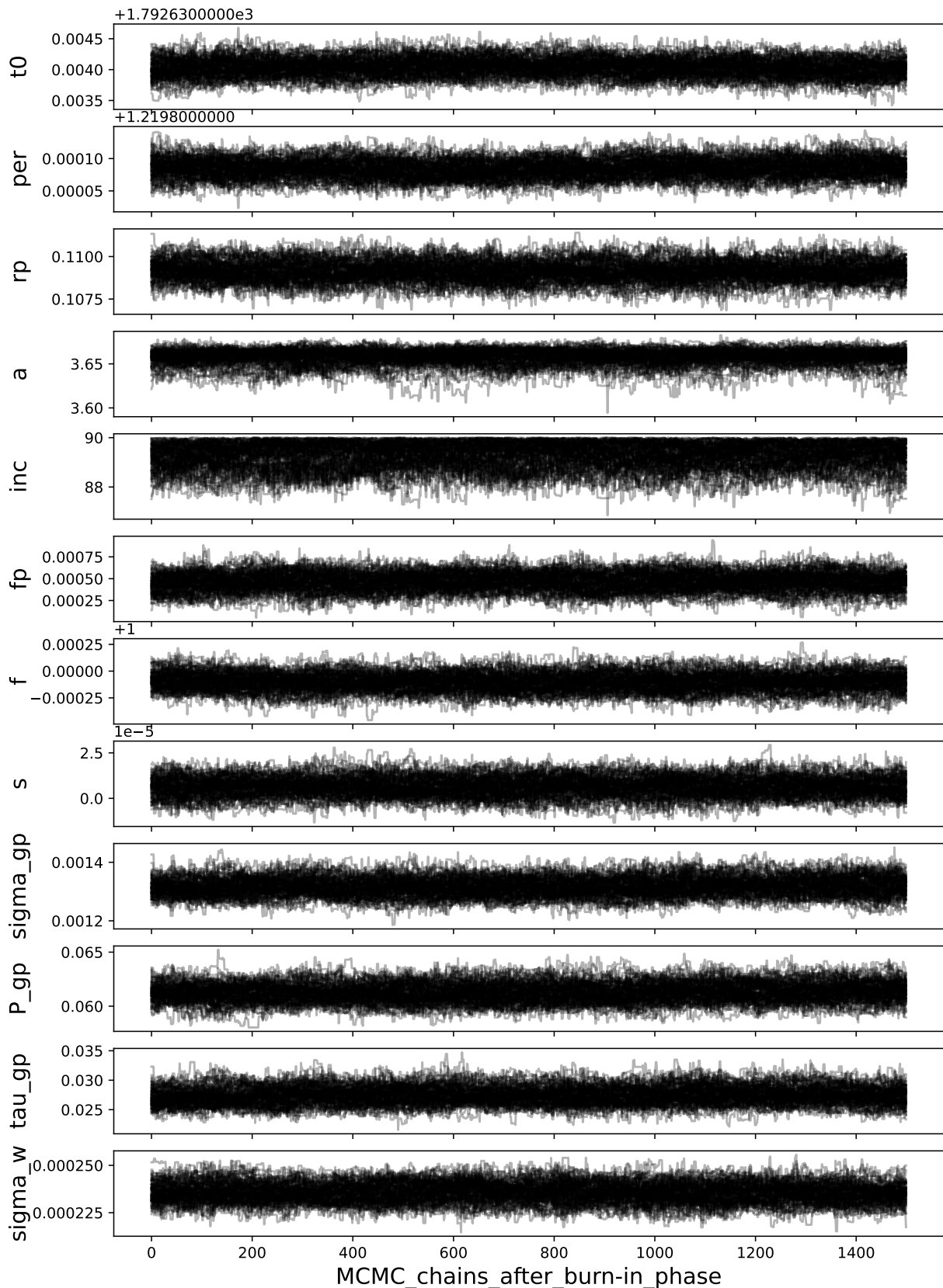


**Figure 4.3:** MCMC Chains after burn-in phase are well settled around a maximum likelihood.



**Figure 4.4:** Corner plot from the joint sector analysis of WASP-77 A b.

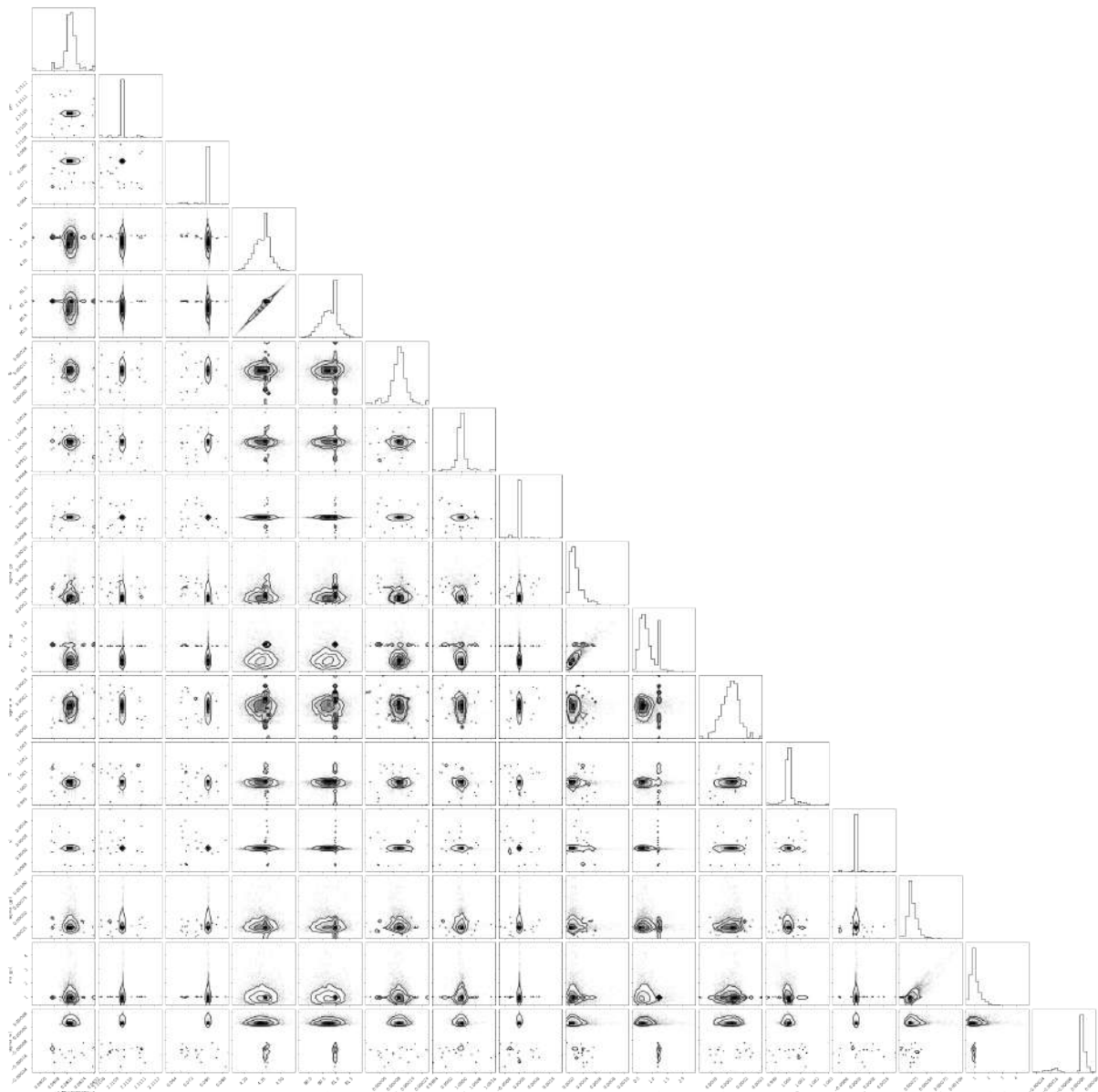


**Figure 4.5:** Corner plot from the joint sector analysis of WASP-111 b.

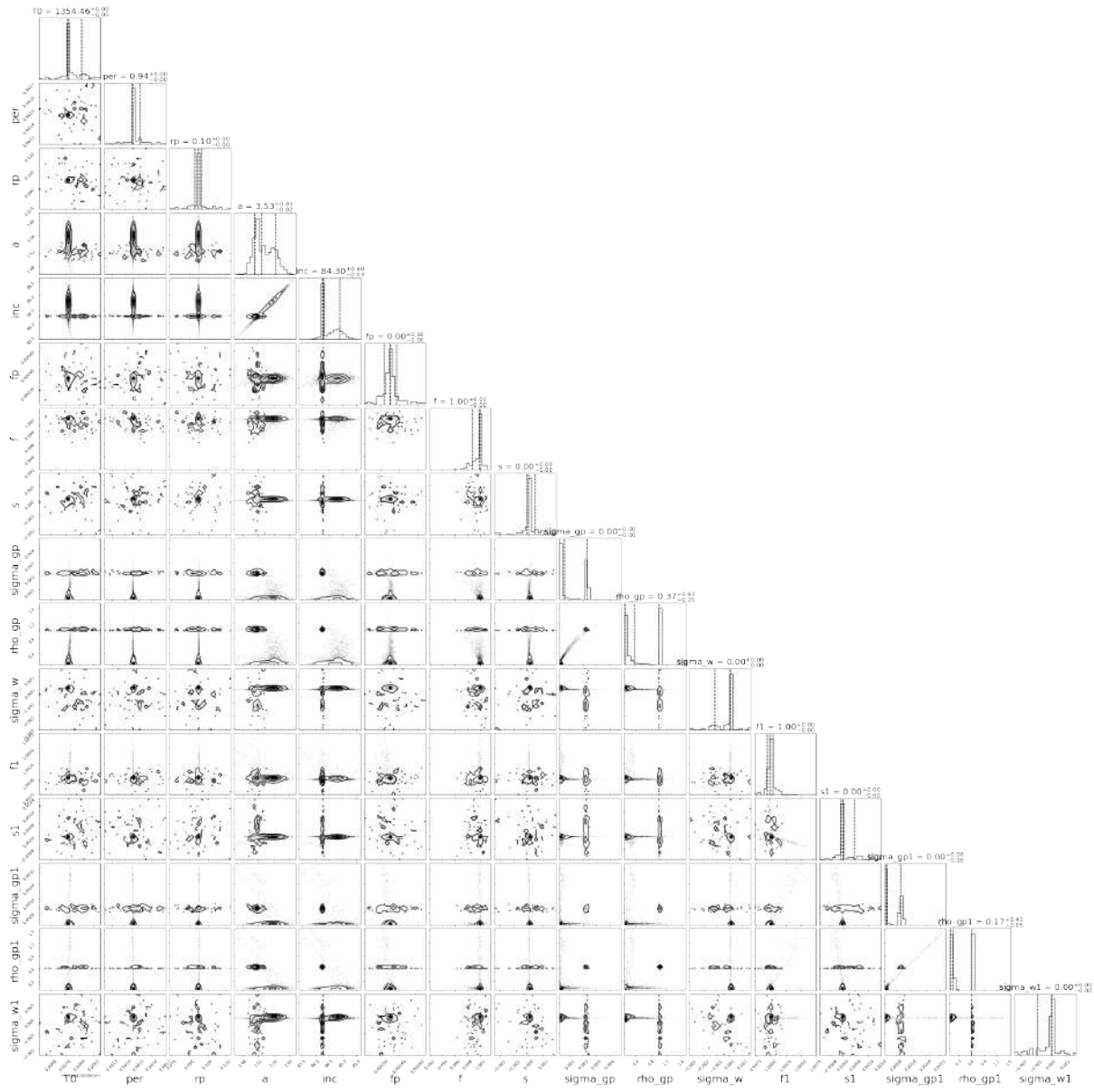


**Figure 4.6:** Corner plot from the joint sector analysis of WASP-18 b.

# Bibliography

- [1] D. R. Anderson et al. “Six newly-discovered hot Jupiters transiting F/G stars: WASP-87b, WASP-108b, WASP-109b, WASP-110b, WASP-111b & WASP-112b”. In: *arXiv e-prints*, arXiv:1410.3449 (Oct. 2014), arXiv:1410.3449. arXiv: [1410.3449 \[astro-ph.EP\]](https://arxiv.org/abs/1410.3449).
- [2] Aaron Bello-Arufe et al. “Mining the Ultrahot Skies of HAT-P-70b: Detection of a Profusion of Neutral and Ionized Species”. In: 163.2, 96 (Feb. 2022), p. 96. DOI: [10.3847/1538-3881/ac402e](https://doi.org/10.3847/1538-3881/ac402e). arXiv: [2112.03292 \[astro-ph.EP\]](https://arxiv.org/abs/2112.03292).
- [3] W. Benz et al. “The CHEOPS mission”. In: *Experimental Astronomy* 51.1 (Feb. 2021), pp. 109–151. DOI: [10.1007/s10686-020-09679-4](https://doi.org/10.1007/s10686-020-09679-4). arXiv: [2009.11633 \[astro-ph.IM\]](https://arxiv.org/abs/2009.11633).
- [4] Allyson Bieryla et al. “KELT-7b: A Hot Jupiter Transiting a Bright V = 8.54 Rapidly Rotating F-star”. In: 150.1, 12 (July 2015), p. 12. DOI: [10.1088/0004-6256/150/1/12](https://doi.org/10.1088/0004-6256/150/1/12). arXiv: [1501.05565 \[astro-ph.EP\]](https://arxiv.org/abs/1501.05565).
- [5] Martin Blažek et al. “Constraints on TESS albedos for five hot Jupiters”. In: 513.3 (July 2022), pp. 3444–3457. DOI: [10.1093/mnras/stac992](https://doi.org/10.1093/mnras/stac992). arXiv: [2204.03327 \[astro-ph.EP\]](https://arxiv.org/abs/2204.03327).
- [6] William J. Borucki et al. “Kepler Planet-Detection Mission: Introduction and First Results”. In: *Science* 327.5968 (Feb. 2010), p. 977. DOI: [10.1126/science.1185402](https://doi.org/10.1126/science.1185402).
- [7] Bruce Campbell, G. A. H. Walker, and S. Yang. “A Search for Substellar Companions to Solar-type Stars”. In: 331 (Aug. 1988), p. 902. DOI: [10.1086/166608](https://doi.org/10.1086/166608).
- [8] A. Cassan et al. “One or more bound planets per Milky Way star from microlensing observations”. In: 481.7380 (Jan. 2012), pp. 167–169. DOI: [10.1038/nature10684](https://doi.org/10.1038/nature10684). arXiv: [1202.0903 \[astro-ph.EP\]](https://arxiv.org/abs/1202.0903).
- [9] David Charbonneau et al. “Detection of Planetary Transits Across a Sun-like Star”. In: 529.1 (Jan. 2000), pp. L45–L48. DOI: [10.1086/312457](https://doi.org/10.1086/312457). arXiv: [astro-ph/9911436 \[astro-ph\]](https://arxiv.org/abs/astro-ph/9911436).
- [10] A. Collier Cameron et al. “Line-profile tomography of exoplanet transits - II. A gas-giant planet transiting a rapidly rotating A5 star”. In: 407.1 (Sept. 2010), pp. 507–514. DOI: [10.1111/j.1365-2966.2010.16922.x](https://doi.org/10.1111/j.1365-2966.2010.16922.x). arXiv: [1004.4551 \[astro-ph.EP\]](https://arxiv.org/abs/1004.4551).

- [11] D. Cont et al. “Detection of Fe and evidence for TiO in the dayside emission spectrum of WASP-33b”. In: 651, A33 (July 2021), A33. doi: [10.1051/0004-6361/202140732](https://doi.org/10.1051/0004-6361/202140732). arXiv: [2105.10230 \[astro-ph.EP\]](https://arxiv.org/abs/2105.10230).
- [12] D. Cont et al. “Silicon in the dayside atmospheres of two ultra-hot Jupiters”. In: 657, L2 (Jan. 2022), p. L2. doi: [10.1051/0004-6361/202142776](https://doi.org/10.1051/0004-6361/202142776). arXiv: [2112.10461 \[astro-ph.EP\]](https://arxiv.org/abs/2112.10461).
- [13] Rosanne Di Stefano et al. “A possible planet candidate in an external galaxy detected through X-ray transit”. In: *Nature Astronomy* 5 (Oct. 2021), pp. 1297–1307. doi: [10.1038/s41550-021-01495-w](https://doi.org/10.1038/s41550-021-01495-w).
- [14] Leonardo A. dos Santos et al. “Search for helium in the upper atmosphere of the hot Jupiter WASP-127 b using Gemini/Phoenix”. In: 640, A29 (Aug. 2020), A29. doi: [10.1051/0004-6361/202038802](https://doi.org/10.1051/0004-6361/202038802). arXiv: [2007.06216 \[astro-ph.EP\]](https://arxiv.org/abs/2007.06216).
- [15] D. Ehrenreich and J.-M. Désert. “Mass-loss rates for transiting exoplanets”. In: 529, A136 (May 2011), A136. doi: [10.1051/0004-6361/201016356](https://doi.org/10.1051/0004-6361/201016356). arXiv: [1103.0011 \[astro-ph.EP\]](https://arxiv.org/abs/1103.0011).
- [16] D. Foreman-Mackey. “Scalable Backpropagation for Gaussian Processes using Celerite”. In: *Research Notes of the American Astronomical Society* 2.1 (Feb. 2018), p. 31. doi: [10.3847/2515-5172/aaaf6c](https://doi.org/10.3847/2515-5172/aaaf6c).
- [17] D. Foreman-Mackey et al. “Fast and scalable Gaussian process modeling with applications to astronomical time series”. In: *ArXiv* (2017). URL: <https://arxiv.org/abs/1703.09710>.
- [18] Daniel Foreman-Mackey. “corner.py: Scatterplot matrices in Python”. In: *The Journal of Open Source Software* 1.2 (June 2016), p. 24. doi: [10.21105/joss.00024](https://doi.org/10.21105/joss.00024). URL: <https://doi.org/10.21105/joss.00024>.
- [19] Daniel Foreman-Mackey et al. “emcee: The MCMC Hammer”. In: 125.925 (Mar. 2013), p. 306. doi: [10.1086/670067](https://doi.org/10.1086/670067). arXiv: [1202.3665 \[astro-ph.IM\]](https://arxiv.org/abs/1202.3665).
- [20] Jonathan Fraine et al. “The Dark World: A Tale of WASP-43b in Reflected Light with HST WFC3/UVIS”. In: 161.6, 269 (June 2021), p. 269. doi: [10.3847/1538-3881/abe8d6](https://doi.org/10.3847/1538-3881/abe8d6). arXiv: [2103.16676 \[astro-ph.EP\]](https://arxiv.org/abs/2103.16676).
- [21] E. Gaidos, D. Kitzmann, and K. Heng. “Exoplanet characterization by multi-observatory transit photometry with TESS and CHEOPS”. In: 468.3 (July 2017), pp. 3418–3427. doi: [10.1093/mnras/stx615](https://doi.org/10.1093/mnras/stx615). arXiv: [1703.02656 \[astro-ph.EP\]](https://arxiv.org/abs/1703.02656).
- [22] D. Gandolfi et al. “TESS’s first planet. A super-Earth transiting the naked-eye star  $\pi$  Mensae”. In: 619, L10 (Nov. 2018), p. L10. doi: [10.1051/0004-6361/201834289](https://doi.org/10.1051/0004-6361/201834289). arXiv: [1809.07573 \[astro-ph.EP\]](https://arxiv.org/abs/1809.07573).
- [23] B. Scott Gaudi et al. “A giant planet undergoing extreme-ultraviolet irradiation by its hot massive-star host”. In: 546.7659 (June 2017), pp. 514–518. doi: [10.1038/nature22392](https://doi.org/10.1038/nature22392). arXiv: [1706.06723 \[astro-ph.EP\]](https://arxiv.org/abs/1706.06723).

- [24] Gregory W. Henry et al. “A Transiting “51 Peg-like” Planet”. In: 529.1 (Jan. 2000), pp. L41–L44. DOI: [10.1086/312458](https://doi.org/10.1086/312458).
- [25] Heather A. Knutson et al. “A map of the day-night contrast of the extrasolar planet HD 189733b”. In: 447.7141 (May 2007), pp. 183–186. DOI: [10.1038/nature05782](https://doi.org/10.1038/nature05782). arXiv: [0705.0993 \[astro-ph\]](https://arxiv.org/abs/0705.0993).
- [26] G. Kovács, S. Zucker, and T. Mazeh. “A box-fitting algorithm in the search for periodic transits”. In: 391 (Aug. 2002), pp. 369–377. DOI: [10.1051/0004-6361:20020802](https://doi.org/10.1051/0004-6361:20020802). arXiv: [astro-ph/0206099 \[astro-ph\]](https://arxiv.org/abs/astro-ph/0206099).
- [27] Laura Kreidberg. “batman: BAsic Transit Model cAlculatioN in Python”. In: 127.957 (Nov. 2015), p. 1161. DOI: [10.1086/683602](https://doi.org/10.1086/683602). arXiv: [1507.08285 \[astro-ph.EP\]](https://arxiv.org/abs/1507.08285).
- [28] Laura Kreidberg et al. “Absence of a thick atmosphere on the terrestrial exoplanet LHS 3844b”. In: 573.7772 (Aug. 2019), pp. 87–90. DOI: [10.1038/s41586-019-1497-4](https://doi.org/10.1038/s41586-019-1497-4). arXiv: [1908.06834 \[astro-ph.EP\]](https://arxiv.org/abs/1908.06834).
- [29] David W. Latham et al. “The unseen companion of HD114762: a probable brown dwarf”. In: 339.6219 (May 1989), pp. 38–40. DOI: [10.1038/339038a0](https://doi.org/10.1038/339038a0).
- [30] Michael B. Lund et al. “KELT-20b: A Giant Planet with a Period of  $P \sim 3.5$  days Transiting the  $V \sim 7.6$  Early A Star HD 185603”. In: 154.5, 194 (Nov. 2017), p. 194. DOI: [10.3847/1538-3881/aa8f95](https://doi.org/10.3847/1538-3881/aa8f95). arXiv: [1707.01518 \[astro-ph.EP\]](https://arxiv.org/abs/1707.01518).
- [31] Nikku Madhusudhan. “C/O Ratio as a Dimension for Characterizing Exoplanetary Atmospheres”. In: 758.1, 36 (Oct. 2012), p. 36. DOI: [10.1088/0004-637X/758/1/36](https://doi.org/10.1088/0004-637X/758/1/36). arXiv: [1209.2412 \[astro-ph.EP\]](https://arxiv.org/abs/1209.2412).
- [32] A. Manduca, R. A. Bell, and B. Gustafsson. “Limb darkening coefficients for late-type giant model atmospheres.” In: 61 (Dec. 1977), pp. 809–813.
- [33] Megan Mansfield et al. “Confirmation of Water Absorption in the Thermal Emission Spectrum of the Hot Jupiter WASP-77Ab with HST/WFC3”. In: 163.6, 261 (June 2022), p. 261. DOI: [10.3847/1538-3881/ac658f](https://doi.org/10.3847/1538-3881/ac658f). arXiv: [2203.01463 \[astro-ph.EP\]](https://arxiv.org/abs/2203.01463).
- [34] Eder Martioli et al. “A survey of eight hot Jupiters in secondary eclipse using WIRCam at CFHT”. In: 474.3 (Mar. 2018), pp. 4264–4277. DOI: [10.1093/mnras/stx3009](https://doi.org/10.1093/mnras/stx3009). arXiv: [1711.07294 \[astro-ph.EP\]](https://arxiv.org/abs/1711.07294).
- [35] P. F. L. Maxted et al. “WASP-77 Ab: A Transiting Hot Jupiter Planet in a Wide Binary System”. In: 125.923 (Jan. 2013), p. 48. DOI: [10.1086/669231](https://doi.org/10.1086/669231). arXiv: [1211.6033 \[astro-ph.EP\]](https://arxiv.org/abs/1211.6033).
- [36] Erin M. May et al. “Spitzer Phase-curve Observations and Circulation Models of the Inflated Ultrahot Jupiter WASP-76b”. In: 162.4, 158 (Oct. 2021), p. 158. DOI: [10.3847/1538-3881/ac0e30](https://doi.org/10.3847/1538-3881/ac0e30). arXiv: [2107.03349 \[astro-ph.EP\]](https://arxiv.org/abs/2107.03349).
- [37] Michel Mayor and Didier Queloz. “A Jupiter-mass companion to a solar-type star”. In: 378.6555 (Nov. 1995), pp. 355–359. DOI: [10.1038/378355a0](https://doi.org/10.1038/378355a0).

- [38] Lokesh Mishra et al. “The New Generation Planetary Population Synthesis (NGPPS) VI. Introducing KOBE: Kepler Observes Bern Exoplanets. Theoretical perspectives on the architecture of planetary systems: Peas in a pod”. In: 656, A74 (Dec. 2021), A74. DOI: [10.1051/0004-6361/202140761](https://doi.org/10.1051/0004-6361/202140761). arXiv: [2105.12745](https://arxiv.org/abs/2105.12745) [astro-ph.EP].
- [39] Hannu Parviainen. “PYTRANSIT: fast and easy exoplanet transit modelling in PYTHON”. In: 450.3 (July 2015), pp. 3233–3238. DOI: [10.1093/mnras/stv894](https://doi.org/10.1093/mnras/stv894). arXiv: [1504.07433](https://arxiv.org/abs/1504.07433) [astro-ph.EP].
- [40] William Pluriel et al. “ARES. III. Unveiling the Two Faces of KELT-7 b with HST WFC3”. In: 160.3, 112 (Sept. 2020), p. 112. DOI: [10.3847/1538-3881/aba000](https://doi.org/10.3847/1538-3881/aba000). arXiv: [2006.14199](https://arxiv.org/abs/2006.14199) [astro-ph.EP].
- [41] William H. Press and George B. Rybicki. “Fast Algorithm for Spectral Analysis of Unevenly Sampled Data”. In: 338 (Mar. 1989), p. 277. DOI: [10.1086/167197](https://doi.org/10.1086/167197).
- [42] George R. Ricker et al. “Transiting Exoplanet Survey Satellite (TESS)”. In: *Journal of Astronomical Telescopes, Instruments, and Systems* 1, 014003 (Jan. 2015), p. 014003. DOI: [10.1111/1.JATIS.1.1.014003](https://doi.org/10.1111/1.JATIS.1.1.014003).
- [43] S. Seager and G. Mallén-Ornelas. “A Unique Solution of Planet and Star Parameters from an Extrasolar Planet Transit Light Curve”. In: 585.2 (Mar. 2003), pp. 1038–1055. DOI: [10.1086/346105](https://doi.org/10.1086/346105). arXiv: [astro-ph/0206228](https://arxiv.org/abs/astro-ph/0206228) [astro-ph].
- [44] S. Seager et al. “On the Dayside Thermal Emission of Hot Jupiters”. In: 632.2 (Oct. 2005), pp. 1122–1131. DOI: [10.1086/444411](https://doi.org/10.1086/444411). arXiv: [astro-ph/0504212](https://arxiv.org/abs/astro-ph/0504212) [astro-ph].
- [45] Avi Shporer et al. “TESS Full Orbital Phase Curve of the WASP-18b System”. In: 157.5, 178 (May 2019), p. 178. DOI: [10.3847/1538-3881/ab0f96](https://doi.org/10.3847/1538-3881/ab0f96). arXiv: [1811.06020](https://arxiv.org/abs/1811.06020) [astro-ph.EP].
- [46] A. M. S. Smith et al. “Thermal emission from WASP-33b, the hottest known planet”. In: 416.3 (Sept. 2011), pp. 2096–2101. DOI: [10.1111/j.1365-2966.2011.19187.x](https://doi.org/10.1111/j.1365-2966.2011.19187.x). arXiv: [1101.2432](https://arxiv.org/abs/1101.2432) [astro-ph.EP].
- [47] B. A. Smith and R. J. Terrile. “A Circumstellar Disk around  $\beta$  Pictoris”. In: *Science* 226.4681 (Dec. 1984), pp. 1421–1424. DOI: [10.1126/science.226.4681.1421](https://doi.org/10.1126/science.226.4681.1421).
- [48] John Southworth et al. “Physical Properties of the 0.94-Day Period Transiting Planetary System WASP-18”. In: 707.1 (Dec. 2009), pp. 167–172. DOI: [10.1088/0004-637X/707/1/167](https://doi.org/10.1088/0004-637X/707/1/167). arXiv: [0910.4875](https://arxiv.org/abs/0910.4875) [astro-ph.EP].
- [49] Gy. M. Szabó and L. L. Kiss. “A Short-period Censor of Sub-Jupiter Mass Exoplanets with Low Density”. In: 727.2, L44 (Feb. 2011), p. L44. DOI: [10.1088/2041-8205/727/2/L44](https://doi.org/10.1088/2041-8205/727/2/L44). arXiv: [1012.4791](https://arxiv.org/abs/1012.4791) [astro-ph.EP].
- [50] G. J. J. Talens et al. “MASCARA-2 b. A hot Jupiter transiting the  $m_V = 7.6$  A-star HD 185603”. In: 612, A57 (Apr. 2018), A57. DOI: [10.1051/0004-6361/201731512](https://doi.org/10.1051/0004-6361/201731512). arXiv: [1707.01500](https://arxiv.org/abs/1707.01500) [astro-ph.EP].

- [51] Pauli Virtanen et al. “SciPy 1.0: Fundamental Algorithms for Scientific Computing in Python”. In: *Nature Methods* 17 (2020), pp. 261–272. DOI: [10.1038/s41592-019-0686-2](https://doi.org/10.1038/s41592-019-0686-2).
- [52] C. von Essen et al. “HST/STIS transmission spectrum of the ultra-hot Jupiter WASP-76 b confirms the presence of sodium in its atmosphere”. In: 637, A76 (May 2020), A76. DOI: [10.1051/0004-6361/201937169](https://doi.org/10.1051/0004-6361/201937169). arXiv: [2003.06424 \[astro-ph.EP\]](https://arxiv.org/abs/2003.06424).
- [53] C. von Essen et al. “Pulsation analysis and its impact on primary transit modeling in WASP-33”. In: 561, A48 (Jan. 2014), A48. DOI: [10.1051/0004-6361/201322453](https://doi.org/10.1051/0004-6361/201322453). arXiv: [1311.3614 \[astro-ph.EP\]](https://arxiv.org/abs/1311.3614).
- [54] C. von Essen et al. “TESS unveils the phase curve of WASP-33b. Characterization of the planetary atmosphere and the pulsations from the star”. In: 639, A34 (July 2020), A34. DOI: [10.1051/0004-6361/202037905](https://doi.org/10.1051/0004-6361/202037905). arXiv: [2004.10767 \[astro-ph.EP\]](https://arxiv.org/abs/2004.10767).
- [55] Songhu Wang et al. “HD 202772A b: A Transiting Hot Jupiter around a Bright, Mildly Evolved Star in a Visual Binary Discovered by TESS”. In: 157.2, 51 (Feb. 2019), p. 51. DOI: [10.3847/1538-3881/aaf1b7](https://doi.org/10.3847/1538-3881/aaf1b7). arXiv: [1810.02341 \[astro-ph.EP\]](https://arxiv.org/abs/1810.02341).
- [56] R. G. West et al. “Three irradiated and bloated hot Jupiters:. WASP-76b, WASP-82b, and WASP-90b”. In: 585, A126 (Jan. 2016), A126. DOI: [10.1051/0004-6361/201527276](https://doi.org/10.1051/0004-6361/201527276). arXiv: [1310.5607 \[astro-ph.EP\]](https://arxiv.org/abs/1310.5607).
- [57] Joshua N. Winn. “Transits and Occultations”. In: *arXiv e-prints*, arXiv:1001.2010 (Jan. 2010), arXiv:1001.2010. arXiv: [1001.2010 \[astro-ph.EP\]](https://arxiv.org/abs/1001.2010).
- [58] A. Wolszczan and D. A. Frail. “A planetary system around the millisecond pulsar PSR1257 + 12”. In: 355.6356 (Jan. 1992), pp. 145–147. DOI: [10.1038/355145a0](https://doi.org/10.1038/355145a0).
- [59] Ian Wong et al. “Systematic Phase Curve Study of Known Transiting Systems from Year One of the TESS Mission”. In: 160.4, 155 (Oct. 2020), p. 155. DOI: [10.3847/1538-3881/ababad](https://doi.org/10.3847/1538-3881/ababad). arXiv: [2003.06407 \[astro-ph.EP\]](https://arxiv.org/abs/2003.06407).
- [60] Ian Wong et al. “Visible-light Phase Curves from the Second Year of the TESS Primary Mission”. In: 162.4, 127 (Oct. 2021), p. 127. DOI: [10.3847/1538-3881/ac0c7d](https://doi.org/10.3847/1538-3881/ac0c7d). arXiv: [2106.02610 \[astro-ph.EP\]](https://arxiv.org/abs/2106.02610).
- [61] G. Zhou et al. “Two New HATNet Hot Jupiters around A Stars and the First Glimpse at the Occurrence Rate of Hot Jupiters from TESS”. In: 158.4, 141 (Oct. 2019), p. 141. DOI: [10.3847/1538-3881/ab36b5](https://doi.org/10.3847/1538-3881/ab36b5). arXiv: [1906.00462 \[astro-ph.EP\]](https://arxiv.org/abs/1906.00462).
- [62] George Zhou et al. “Spin-orbit alignment for KELT-7b and HAT-P-56b via Doppler tomography with TRES”. In: 460.3 (Aug. 2016), pp. 3376–3383. DOI: [10.1093/mnras/stw1107](https://doi.org/10.1093/mnras/stw1107). arXiv: [1605.01991 \[astro-ph.EP\]](https://arxiv.org/abs/1605.01991).